UNIVERSITY OF CALIFORNIA
RIVERSIDE

Spectroscopy and Photoelectric Properties of 1D Single-Walled Carbon Nanotubes and 2D Molybdenum Disulfide and their Applications for Energy Storage, Photodetection and Chemical Sensing

A Dissertation submitted in partial satisfaction
of the requirements for the degree of

Doctor of Philosophy

in

Chemical and Environmental Engineering

by

Guanghui Li

December 2018

Dissertation Committee:
Prof. Juchen Guo, Co-Chairperson
Prof. Mikhail E. Itkis, Co-Chairperson
Prof. Bryan M. Wong

The Dissertation of Guanghui Li is approved:

_____

_____

Committee Co-Chairperson

_____

Committee Co-Chairperson

University of California, Riverside

Acknowledgement

I would take this opportunity to thank my advisors: Prof. Robert Haddon, Prof. Mikhail Itkis, and Prof. Juchen Guo, and my committee member Prof. Wong. I would like to first thank Prof. Haddon for letting me join and work in the wonderful research group. It is a great honor and pleasure to work with him, even though only two years. During these two years, I learnt a lot from him. He always could explain the complicated result with his solid theory knowledge, making it clear and understandable to us. I was deeply impressed by his brilliance, enthusiasm in research, and confidence. He was the most brilliant and talented scientist I have ever met.

I would like to thank Prof. Mikhail Itkis who guided and supported me during my four and half year study at UCR. He taught me how to design experiment, analyze results, and communicate with other people. He is always very nice and patient to explain the problems and questions, and encouraged me and gave me confidence to pass through the difficulties. He can always find the valuable data from the experiment results and analyze it, which provides useful guidance for the next-step experiment. Prof. Mikhail Itkis is not only a great scientist but also a talented engineer. He can always find the best way to prepare devices with smart method and set up the testing system. During my study at UCR, he not only provided help in my research, but gave me much assistance in my life. Without his continues guidance, support, and assistance, I cannot finish this work.

I also want to thank Prof. Juchen Guo who helped me a lot before and after he became my advisor. In my first research project, Dr. Chengyin Fu from Prof. Guo research group provided many good samples for the Raman and UV-Vis spectroscopic

study. Whenever I have problems and difficulties, he can always give me some good suggestions and guidance.

I would like to thank my committee Prof. Bryan Wong for his advice, comments and suggestions in my research. I also want to acknowledge him for his significant contribution to the DFT calculations in my work which provides solid theory knowledge to explain the geometry of sulfur in SWNTs.

I want to acknowledge people who guided and collaborated with me during my study: Dr. Chengyin Fu prepared S@SWNTs samples for Raman and UV-Vis spectroscopic study; Dr. M. Belèn Oviedo did DFT simulations in S@SWNTs; Prof. Jianlin Liu gave me good suggestions and comments in SWNT/ZnO based UV photodetector; Dr. Mohammad Suja for ZnO thin film preparation; Prof. Ashok Mulchandani for comments and suggestions on MoS_2 based gas sensor; Tung Pham for MoS_2 thin film growth and device preparation.

I want to thank my group current and former members: Prof. Elena Bekyarova, Dr. Xiaojuan Tian, Dr. Matthew Moser, Dejan, Wangxiang, and Mingguang for their help and suggestions. I also want to thank the staff from the Center for Nanoscale Science and Nanotechnology-Nancy, Eva, and Nadine, Mark, Dong for their help.

I'd like to express my thanks to my parents, my brother (Guanglei Li) and my cousin (Jinglu Ma) for their unconditional support and love. I want to thank my dearest wife Yingying Hao for her companionship for the last seven years. I am a lucky dog to meet her in my life. I sincerely appreciate the love, sacrifices, and support she gives me.

I wish to acknowledge the financial support from NSF under contracts ECCS-1404671, support from Vice Chancellor for Research and Economic Development, University of California, Riverside.

Portions of the dissertation are adapted with permission from the following references:

Chapter 2:

Guanghui Li, Chengyin Fu, M. Belen Oviedo, Mingguang Chen, Xiaojuan Tian, Elena Bekyarova, Mikhail E. Itkis, Bryan M. Wong, Juchen Guo, and Robert C. Haddon, Giant Raman Response to the Encapsulation of Sulfur in Narrow Diameter Single-Walled Carbon Nanotubes, *J. Am. Chem. Soc*, **2016**, 138 (1), 40-43

Chapter 3:

Guanghui Li, Mohammad Suja, Mingguang Chen, Elena Bekyarova, Robert C. Haddon, Jianlin Liu, Mikhail E. Itkis, Visible-Blind UV Photodetector Based on Single-Walled Carbon Nanotube Thin Film/ZnO Vertical Heterostructures, ACS Appl. Mater. Interfaces, **2017**, 9, 37094-37104

This thesis is dedicated to my parents, Jianghuo Li and Erxiu Ma, and my dear wife Yingying Hao

ABSTRACT OF THE DISSERTATION

Spectroscopy and Photoelectric Properties of 1D Single-Walled Carbon Nanotubes and 2D Molybdenum Disulfide and their Applications for Energy Storage, Photodetection and Chemical Sensing

by

Guanghui Li

Doctor of Philosophy, Graduate Program in Chemical and Environmental Engineering
University of California, Riverside, December 2018
Dr. Juchen Guo, Dr. Mikhail E. Itkis, Co-Chairperson

Single-walled carbon nanotubes (SWNTs) offer extraordinary physical and chemical properties such as high carrier mobility and current-carrying capacity, unique optoelectronic properties, large surface area, and high electrochemical stability, thus showing great potential for applications in thin-film transistors, novel electronic and optoelectronic devices, logic circuits, solar cells, and lithium-sulfur batteries.

In Chapter 1, the fundamental properties of SWNTs are introduced, including their structure, electronic and spectroscopy properties, growth method, thin film preparation, and potential applications. In chapter 2, sulfur encapsulation of SWNTs were prepared and studied by Raman and UV-Vis-NIR spectroscopy techniques. We discovered a giant Raman response to the encapsulation of sulfur in narrow diameter SWNTs with the appearance of new peaks at 319, 395 and 710 cm^{-1} which originate from the sulfur species within the SWNTs. The encapsulated species also shift the near-IR interband electronic transitions to lower energy by more than 10%. These effects seem to originate

from the van der Waals interaction of the confined sulfur species with the walls of the SWNTs.

In chapter 3, we utilized a semitransparent film of p-type semiconducting single-walled carbon nanotubes (SC-SWNTs) with an energy gap of 0.68 ±0.07 eV in combination with a molecular beam epitaxy grown n-ZnO layer to build a vertical p-SC-SWNT/n-ZnO heterojunction-based UV photodetector. The resulting device shows a current rectification ratio of 10^3, a current photoresponsivity up to 400 A/W in the UV spectral range from 370 to 230 nm, low dark current, and UV-to-Visible photoresponsivity ratio of 10^5

In chapter 4, the CVD grown single-layer MoS_2 with Au metal electrodes based gas sensor was utilized. Red light illumination was used to induce a photocurrent which was employed instead of dark current for NO_2 gas sensing. Resulted Au/MoS_2/Au optoelectronic gas sensor showed a significant enhancement of the device sensitivity *S* toward ppb level of NO_2 gas exposure reaching *S*=4.9%/ppb (4900%/ppm) and extremely low limit of detection of NO_2 gas at the level of 0.2 ppb was obtained.

Key Words: SWNTs, Sulfur Encapsulation, Raman Spectroscopy, UV Detection, Heterojunction

Table of Contents

List of Figures

Chapter 1 Introduction to Carbon Nanotubes (CNTs)

Carbon is the basic element in our life which can form many types of organic and inorganic compounds. On the basis of carbon a numerous of amazing structures like zero-dimensional (0D) C_{60},[1-2] one-dimensional (1D) carbon nanotubes (CNT),[3] two-dimensional (2D) graphene,[4] and three-dimensional (3D) graphite or diamond are formed. Among them, graphene, which is composed of a single layer of carbon atoms, is regarded as the mother of all these structures.[5-7] As shown in Figure 1.1, graphene can wrap into 0D C_{60}, roll up into 1D CNT, and stack into 3-D graphite. In the past few decades, 0D, 1D, and 2D carbon based nanomaterials have attracted much attention due to their novel and unique physical and chemical properties and their potential applications in various fields were explored.[8]

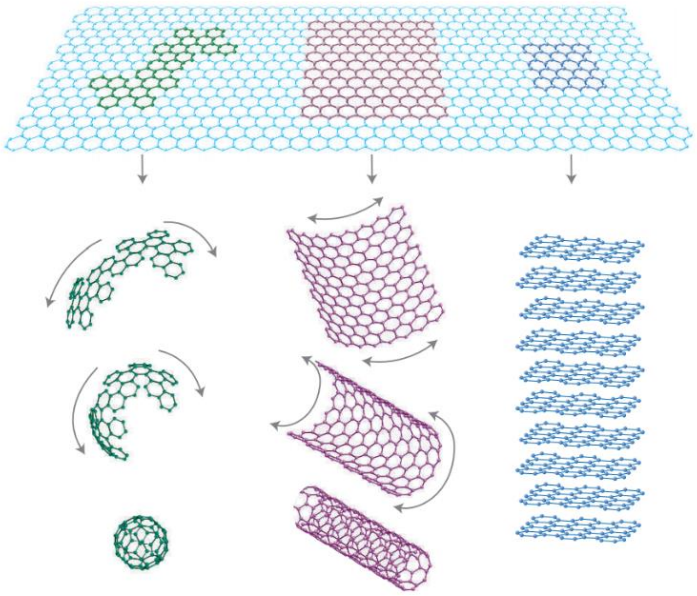

Figure 1.1 From one-atom thick layer of graphene, 0D buckyballs, 1D nanotubes, and 3D graphite can be formed.[8]

Depending on the number of the shells, CNTs can be categorized as multi-walled (MWNTs) and single-walled carbon nanotubes (SWNTs) (Figure 1.2). MWNTs with a diameter ranging from few nanometers to hundred nanometers were first discovered by Iijima in 1991.[3] Two years later, SWNTs were first-time synthesized by arc-discharge method with transition–metal catalyst, and the diameter ranging from 0.7 nm to 1.6 nm. [9-10] Carbon nanotube is 1D nanomaterial which became a hot topic of research due to its unique structure, outstanding electric, photonic, and chemical properties. Up to now, an enormous amount of research has been conducted to explore its potential application in various fields, including field-effect transistors, chemical sensors, photodetectors, solar cells, light modulators, and lithium batteries.[11-16]

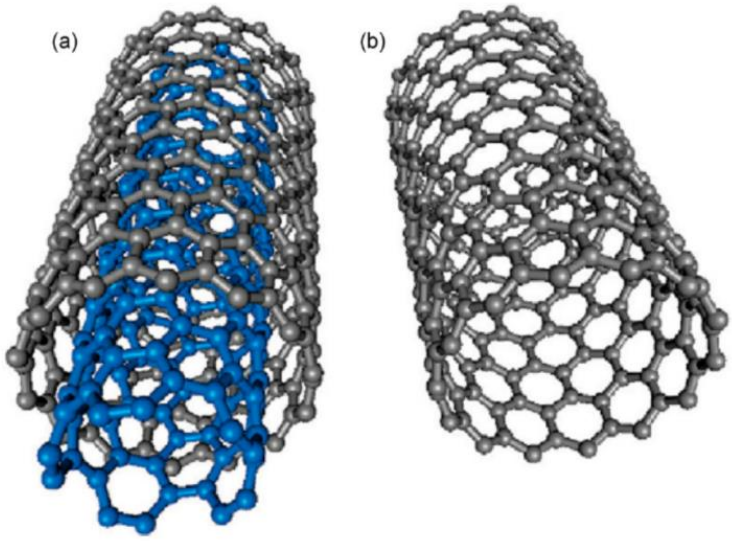

Figure 1.2 Schematic structure of (a) multi-walled carbon nanotubes (MWNTs); (b) single-walled carbon nanotubes (SWNTs).[17]

During my study in UCR, my research has been mainly focused on developing next-generation optoelectronic nano devices based on the SWNTs thin films. In this chapter, I will introduce some general information about the SWNTs.

1.1 Crystal Structure of SWNTs

SWNT is a one-dimensional carbon-based nanomaterial which can be viewed as a sheet of graphene rolled into cylinder along a chiral vector (*m*, *n*) as shown in Figure 1.3.[18] SWNTs structure can be defined by the chiral index (*m*, *n*) which determines its diameter, electronic and photonic properties. As shown in Figure 1.3, a_1 and a_2 are the unit vectors of the hexagonal honeycomb lattice in graphene sheet, where $a_1=a_2=0.246$ nm. The diameter of SWNTs can be calculated by the following equation[19]

$$d = \frac{a}{\pi}\sqrt{n^2 + nm + m^2} \qquad (1.1)$$

where a is a lattice constant: $a = a_1 = a_2 = 0.246\,nm$. The chiral angle is $\theta = tan^{-1}[\frac{\sqrt{3}n}{2m+n}]$ which is in the range of $0 \leq |\theta| \leq 30^o$

When m=n, the carbon nanotube is armchair (Figure 1.3b), it is zigzag when n=0 or m=0 (Figure 1.3 c), or chiral for any other n and m (Figure 1.3 d).[18, 20] Depending on the chiral vector of SWNTs $C=na_1+ma_2$, SWNTs can be either metallic or semiconducting.

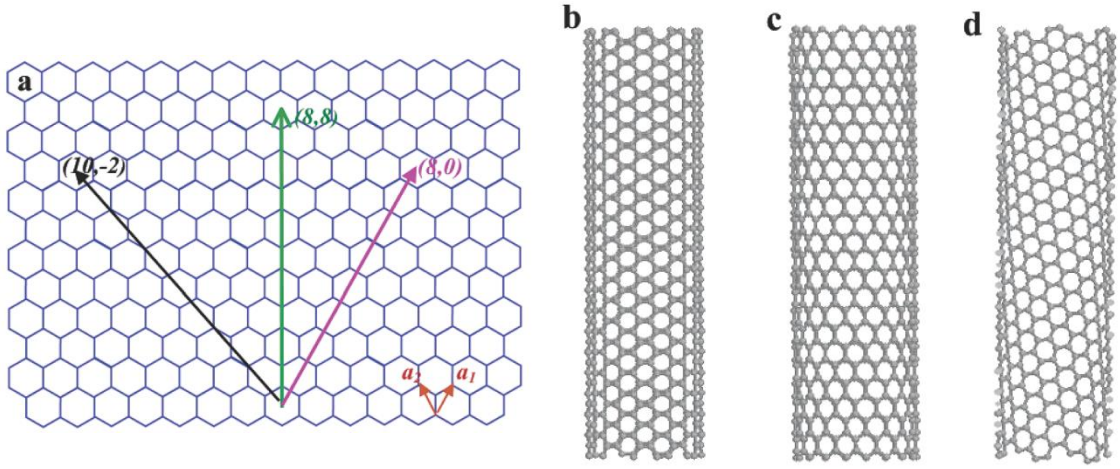

Figure 1.3 (a) Schematic honeycomb structure of a graphene sheet. SWNT can be formed by folding the sheet along lattice vectors. The two basis vectors a_1 and a_2 are shown. Folding of the (8,8), (8,0), and (10,-2) vectors leads to armchair (b), zigzag (c), and chiral (d) SWNTs.[18]

1.2 Electronic Properties of SWNTs

As discussed above, the physical and chemical properties of SWNTs heavily depend on their chirality (m, n). SWNTs can be visualized as graphene rolled along a chiral vector, so we can derive the electronic properties by analyzing the properties of graphene. In the plane sheet of graphene, there are four valence orbitals of carbon atom, including

2s, $2p_x$, sp_y, and $2p_z$ orbitals, in which *s*, p_x, p_y orbitals form sp^2 hybridization in-plane σ (bonding or occupied) and σ^* (antibonding or unoccupied) orbitals, corresponding σ valence bands and σ^* conduction bands.[21] The σ bonds in SWNTs are responsible for the binding energy and elastic properties of graphene sheet but not the band structure as they are far from the Fermi energy.[20] The $2p_z$ orbitals are oriented perpendicularly to graphene sheet and can't be coupled with σ states. Thus, the interaction between the p_z orbitals in carbon atoms forms a π (bonding) and π^* (antibonding) orbitals, corresponding to the π valence band and π^*conduction band. The π bonds are responsible for the electronic states near the Fermi energy in SWNT, so they play an important role in the band structure and electronic properties of SWNTs.[20-21]

The graphene band structure can be calculated within the tight-binding model of graphene.[20-21] Figure 1.4a shows the energy dispersion along the high symmetry direction of triangle $\Gamma M K$ throughout the Brillouin zone. The upper half of the energy dispersion curves describe the π^*-energy bonding band while the lower half is π energy bonding band, which degenerate at the *K* points with crossing at the Fermi energy. These two bands touch each other at six points called Dirac or neutrality points (Figure 1.4b) thus making graphene a zero-gap semimetal.[22]

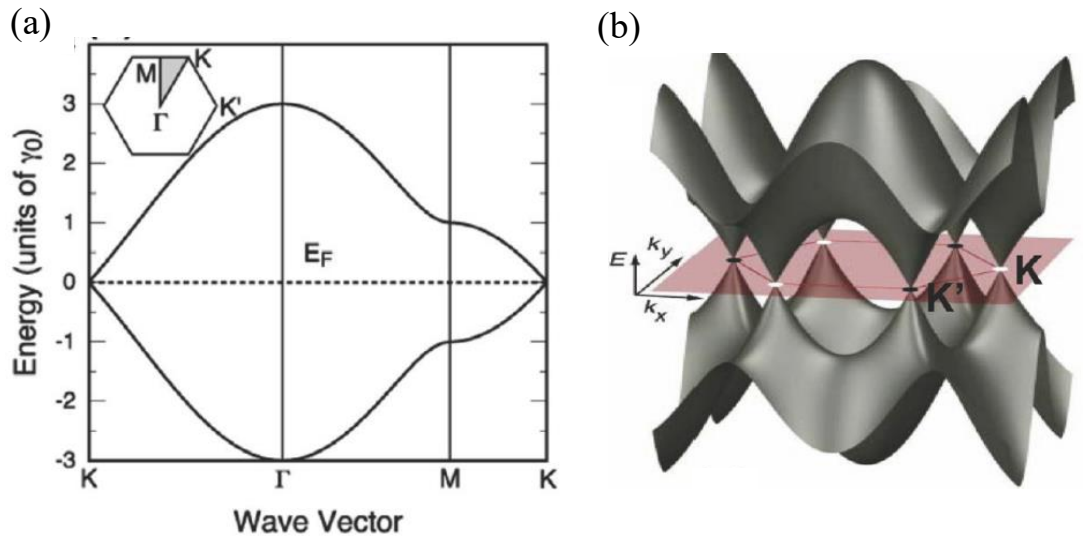

Figure 1.4 (a) Energy dispersion of graphene; (b) 3D band structure of graphene.[22]

The electronic structure of the SWNTs can be derived from that of 2D graphene. As SWNT is one-dimensional, so the wave vectors along the nanotube axis is still continuous like graphene, while the along the diameter can be quantized due to the limited circumference. When the chirality of SWNTs satisfies $n - m = 3l$ relationship, the π band will cross the Fermi level at *K* point with corresponding zero bandgap and metallic behaviors of the SWNTs, like in case of graphene (Figure 1.4a).[20] All the armchair SWNTs are metallic as *m*-*n*=0. In theory, metallic SWNTs have an electrical conductivity as high as 4×10^5 S/cm and the electric current density can reach 4×10^9 A/cm^2 which is 1,000 times higher than for copper.[16]

On the other hand, in the situation of $n - m = 3l \pm 1$, SWNTs show semiconducting characters with a small bandgap calculated as below:

$$\Delta E_g = \frac{2\pi\alpha\gamma_0}{\sqrt{3}|C_h|} \qquad (1.2)$$

where $|C_h| = \pi d_t$, and $\gamma_0 = 2.9\ eV$.

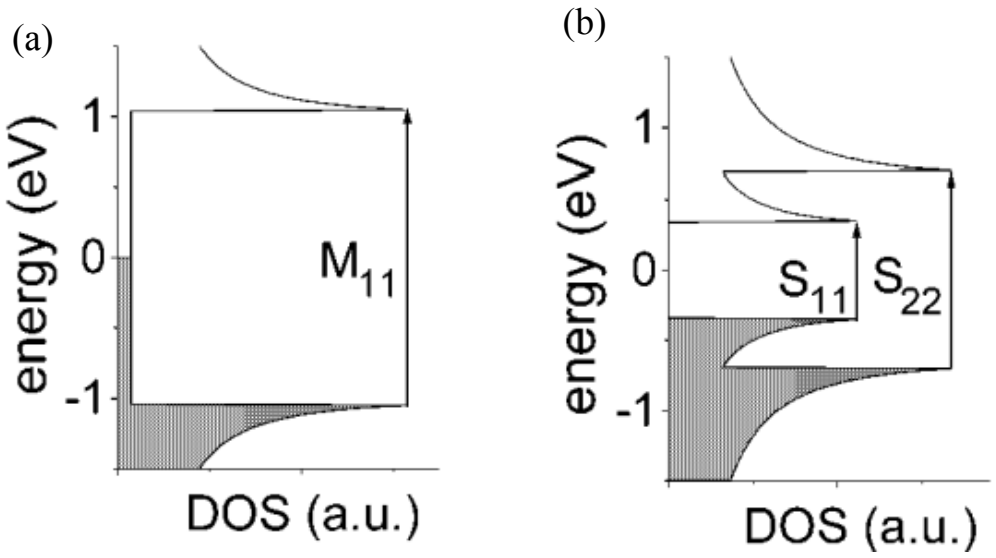

Figure 1.5 Schematic diagram of the density of states (DOS) of SWNTs. (a) Metallic SWNTs; (b) Semiconducting SWNT.[23]

1.3 Spectroscopic Studies of the SWNTs

As shown in equation 1.2, the bandgap of SWNTs is reversely proportional to the tube diameter. Up to now, several techniques have been used to experimentally study crystal and electronic structure of the SWNTs like scanning tunneling spectroscopy (STM), UV-Vis-NIR spectroscopy, and Raman spectroscopy.[24-26]

1.3.1 Scanning Tunneling Microscopy of SWNTs

Ultra-high-vacuum (UHV) scanning tunneling microscopy (STM) is a useful tool to probe the surface of the SWNTs with atomic resolution, and scanning tunneling spectroscopy (STS) was used for band structure measurement.[18, 24, 27] Lieber research group studied the electronic properties of single SWNTs with different diameters with atomic resolution by STM (Figure 1.6).[24] They resolved the hexagonal-ring structure of carbon nanotube walls and measured their corresponding electronic properties. The

results confirmed that the electronic properties of the SWNTs depend on their diameters and helicities. In the semiconducting SWNTs, the bandgap reversely depends on the diameter, which was consistent with the theory calculation.

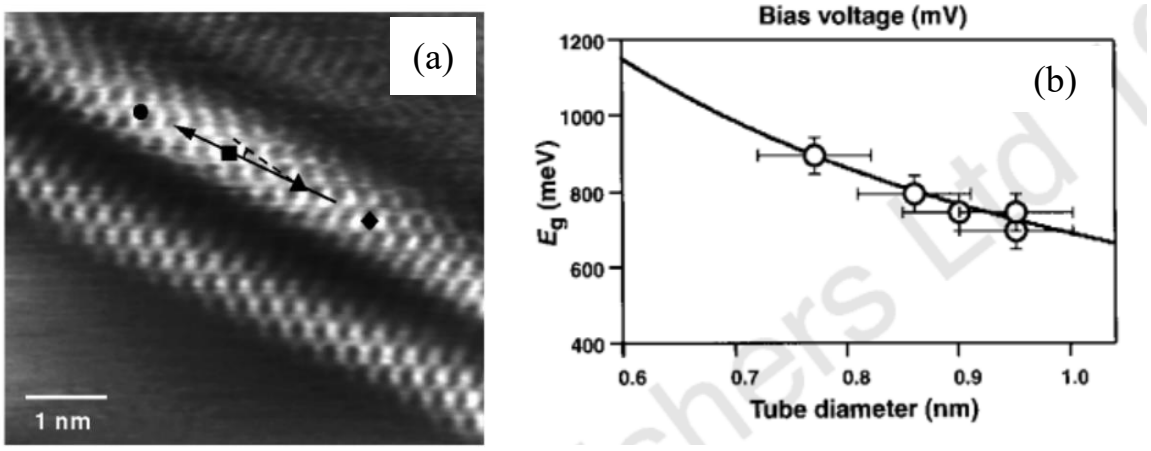

Figure 1.6 (a) Structure and spectroscopy of semiconducting SWNTs. (b) Bandgap (*Eg*) versus tube diameter.[24]

1.3.2 UV-Vis-Near-IR Spectroscopy of the SWNTs

The electronic structure of SWNTs is determined by the chirality (*m, n*) and show either semiconducting or metallic character with series of spikes in *DOS* (Figure 1.5). The optical absorption of SWNTs is closely related to their corresponding structures, so it gives a tool to study SWNTs electronic states by measuring their optical absorption spectra. Haddon group measured the sub-bands of SWNTs of different diameters produced by arc discharge, laser ablation, and HiPCO methods by Vis-NIR spectroscopy (Figure 1.7).[28] As shown in Figure 1.7, the UV-Vis-NIR spectra of semiconducting SWNTs show a few absorption peaks such as S_{11} and S_{22} corresponding to the first and second interband transitions, respectively. M_{11} peak corresponds the first interband transition in metallic SWNTs.[28] It was confirmed that positions of the maximums of the

first (S_{11}) and second absorption (S_{22}) bands are sensitive to the diameter of SWNTs, increasing with the decrease of the SWNTs diameter.[24, 28-29]

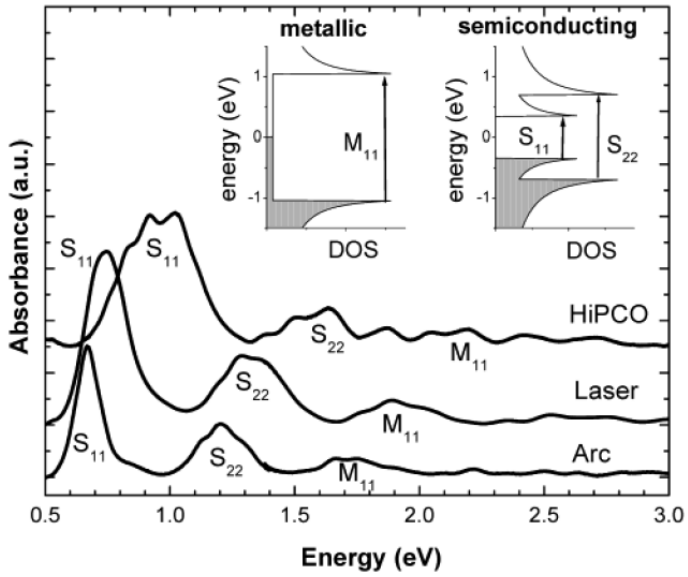

Figure 1.7 Absorption spectra (Varian Cary 500 spectrometer) of films of purified HiPCO, purified laser ablation, and electric arc discharge produced SWNTs after baseline correction.[28]

The individual SC-SWNTs shows outstanding electronic properties with the mobility of charge carriers of 10^5 $cm^2/s/V$ and the on/off ratio of 10^5.[16] For the SC-SWNTs thin film, the conductivity can reach 250-400 S/cm.[30]

1.3.3 Raman Spectroscopy Properties of the SWNTs

Raman spectroscopy is a fast, nondestructive, and high-resolution tool for the characterization of carbon nanotubes.[31-35] It provides phonon spectra of the SWNTs closely related to their crystal, electronic structure, and the defects in SWNTs. Raman scattering is an inelastic scattering photons by phonons, where a photon excites the electrons which are scattered by phonons, resulting in the energy shift of photon: $\hbar\omega_L -$

$\hbar\omega_{Sc} = \hbar\Omega$. By plotting the intensity of the scattered light as a function of the difference between the incident and scattered photon energy, the Raman spectra of the sample can be obtained. As shown in Figure 1.8, there are four main regions in the SWNT Raman spectra which are *G* band, radial breathing mode (*RBM*), *D* bands and *IFM* bands.[36]

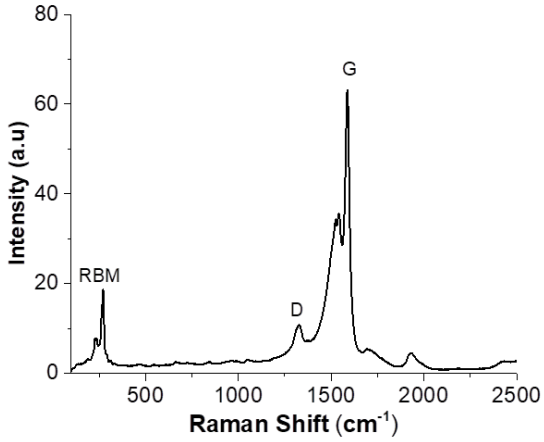

Figure 1.8 Raman spectra of HiPCO SWNTs.[36]

The phonon structure of SWNTs can be derived from graphene structure. In single layer graphene, each unit cell contains two carbon atoms, *A* and *B*, which form a triangular network with their neighbor atoms (Figure 1.9).[37]

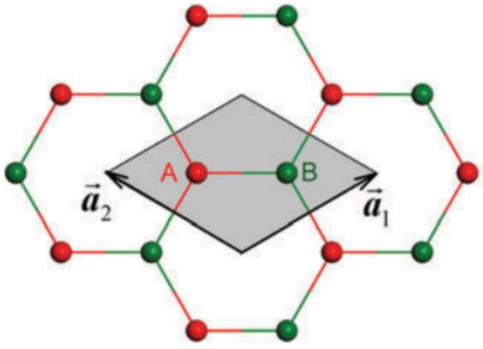

Figure 1.9 Top view of unit cell of 1 layer graphene.[37]

Therefore, there are six vibration modes at the center of Brillouin zone of one-layer graphene (Γ point), including two double-degenerate modes (Figure 1.10). The lattice vibrations in one-layer graphene at Γ point can be described as: $\Gamma_{1LG} = A_{2u} + B_{2g} + E_{1u} + E_{2g}$ shown in Figure 1.10. E_{2g} is a doubly degenerate in-plane mode which is Raman-active, while B_{2g} mode is out-of-plane optical mode which is neither Raman nor infrared active. A_{2u} and E_{1u} (doubly degenerate) are the translations of the plane and E_{1u} is infrared –active.[37]

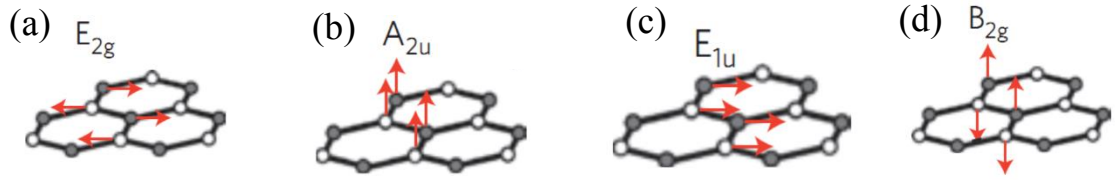

Figure 1.10 The atoms displacements of phonon modes at the Γ points of 1 layer graphene: (a) E_{2g} mode, (b) A_{2u} mode, (c) E_{1u} mode, and (d) B_{2g} mode.[37]

From the theoretical calculation, there are six phonon branches at the Γ point in one layer graphene which are three acoustic phonon modes and three optical phonon modes. The acoustic phonon modes are composed by out-of-plane transverse acoustic (*oTA*), in-plane transverse acoustic (*iTA*), longitudinal acoustic (*LA*). The optical modes are out-of-plane transverse optic (*oTO*), in-plane transverse optic (*iTO*), and longitudinal optic (*LO*), shown in Figure 1.11.[32] The three acoustic phonon modes are composed of A_{2u} and E_{1u} modes, and the optical phonon modes are E_{2g} and B_{2g} modes.

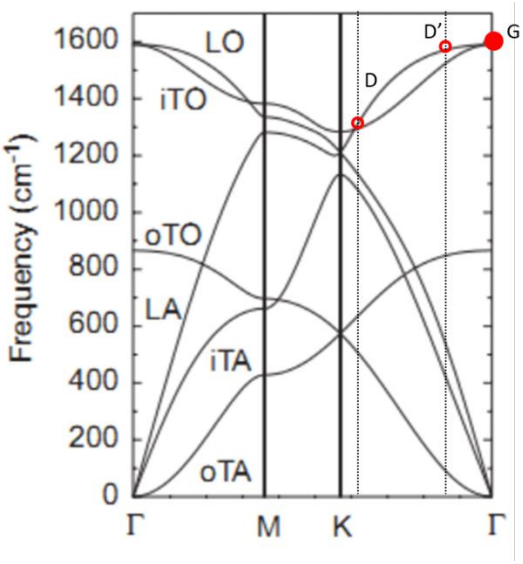

Figure 1.11 Phonon dispersion of graphene.[32]

The phonon dispersion of SWNTs can be calculated by zone folding the phonon dispersion curves of a two-dimensional graphene layer as follow:

$$\omega_{1D}^{m\mu}(k) = \omega_{2D}^{m}\left(k\frac{K_2}{|K_2|} + \mu K_1\right), \quad \begin{pmatrix} \text{m=1,...,6} \\ \text{μ=0,....,N−1} \end{pmatrix} \; and \; -\frac{\pi}{T} < k \leq \frac{\pi}{T} \qquad 1.3$$

where m is the number of acoustic and optical modes, k is a one-dimensional wave vector, K_1 and K_2 are the reciprocal vectors in the circumferential direction and along the nanotube axis, respectively, T is the magnitude of the one-dimensional translation vector **T:**

$$T = |\mathbf{T}| = 3^{1/2}L/d_R \qquad 1.4$$

Based on the zone folding procedure, the phonon dispersion curves of the SWNTs can be calculated. Figure 1.12 shows the phonon dispersion curves of the (10,10) SWNT.[32]

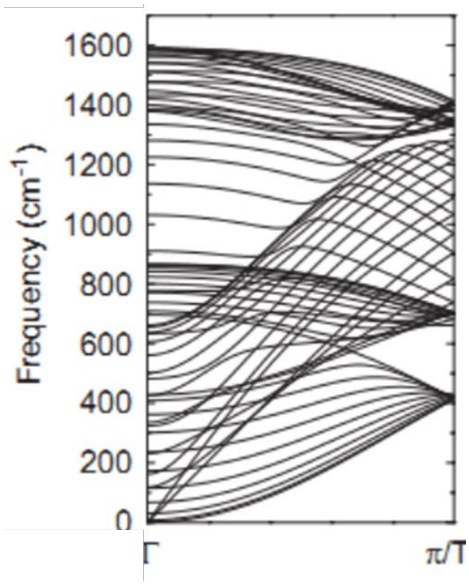

Figure 1.12 The phonon dispersion of armchair carbon nanotube (10,10).[32]

***G*-band**

G-band in graphene or SWNTs is from the stretching of the *C*-*C* bonds which is a common feature in all sp^2 carbon system (~1582 cm^{-1}).[32] The *G*-band is related to the Raman-active E_{2g} mode, which is at the crossing point of *iTO* and *LO* at the Brillouin zone (*BZ*) center (Figure 1.13).[38] In SWNTs, the most intense *G*-band is from the carbon vibration along the tube axis (ω^+ *G*-band), which negligibly depends on the SWNT diameter. The *C*-*C* bonds also vibrate along the circumferential direction, and the frequency depends on the tube diameter (ω^- *G*-band).

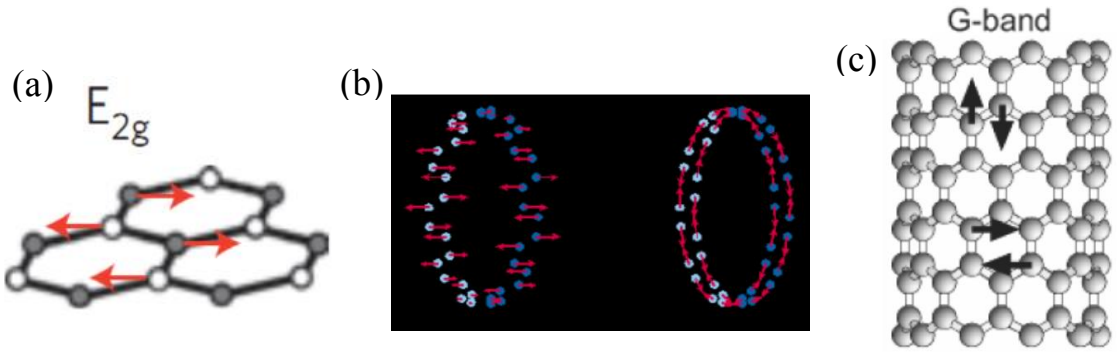

Figure 1.13 E_{2g} mode in 1 layer graphene[37], (b)[26]and (c) schematic of *G* band modes.[39]

As ω_G^- strongly depend on the diameter (d_t) of SWNTs while ω_G^+ is independent on d_t, the d_t can be calculated from the equation below:

$$\omega_G^- = \omega G - {}^{\varphi}/_{d_t^2} \qquad 1.5$$

where φ=47.7 $cm^{-1}nm^2$ for semiconducting SWNTs and φ=79.5 $cm^{-1}nm^2$

In graphene or SWNTs, the *G* peak produced in Raman scattering is a one-phonon process. Briefly, the electron is excited from the valence band to conduction band, and then scattered by a E_{2g} phonon.[37] The scattered electron will combine with a hole and relax the photon (Figure 1.14).

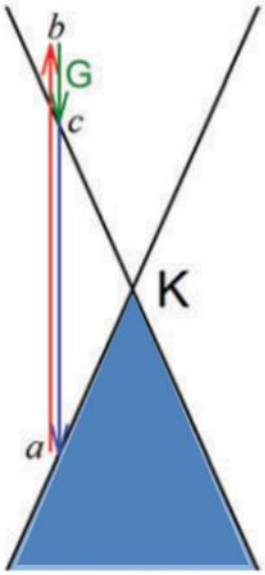

Figure 1.14 Single resonance process of *G* mode in 1 layer graphene.[37]

As *G*-band is from the carbon vibration in E_{2g} mode and it is very sensitive to strain effects in sp^2 carbon materials. Therefore, when the length and the angles of graphene change due to the external strain or the interaction with substrate, the *G*-band of graphene will shift.[34]

***RBM* Mode**

In SWNTs, the *RBM* modes are usually strong at low frequencies ranging from 100 cm^{-1} to 400 cm^{-1}. The *RBM* is a first-order Raman Scattering process which is a bond-stretching out-of-plane mode. All the carbon atoms in SWNTs vibrate in the radial direction like breathing (Figure 1.15). [39]

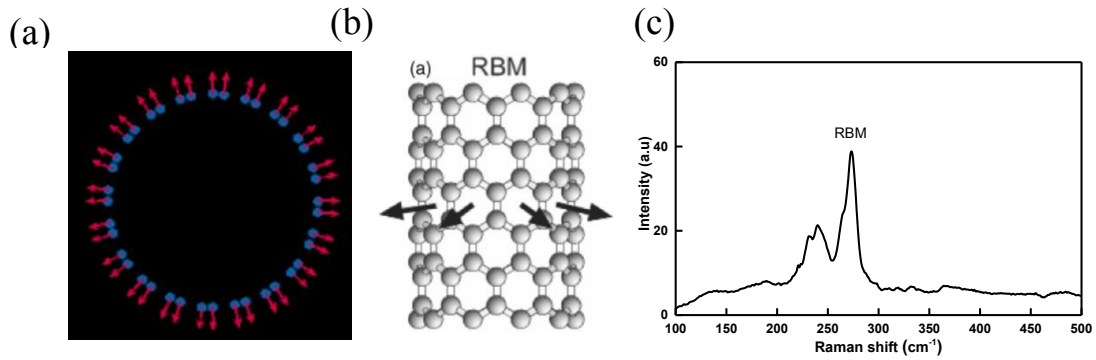

Figure 1.15 (a) and (b) *RBM* modes of SWNTs[31, 43] (c) The Raman spectra of HiPCO SWNT within the *RBM* range.

The frequencies of *RMB* are closely related to the diameters of SWNTs. Therefore, SWNTs diameters can be directly and conveniently determined via Raman spectroscopy method by measuring the *RMB* features. The relationship between the *RBM* frequency and diameter of SWNT can be expressed as follow:

$$\omega_{RBM} = \frac{A}{d_t} + B\ (cm^{-1}) \qquad 1.6$$

where A= 248 cm^{-1}nm for isolated SWNTs on SiO_2 substrate, and B is the parameter caused by environmental factors.[32] Therefore, the diameter of the SWNTs can be calculated by measuring the *RBM* frequency of SWNTs (100-400 cm^{-1}). When $d_t \rightarrow \infty$, ω_{RBM} goes to zero, so there is no *RMB* feature in graphene. Raman spectroscopy can probe the diameters of both metallic and semiconducting SWNTs.[40]

The electronic structure of SWNTs can be determined by measuring the intensity of *RBM* peaks under various excitations. Jorio et al. studied the shape of joint density of electronic states (*JDOS*) of isolated SWNTs by Raman spectroscopy technique with a tunable laser.[41] As the resonant Raman intensity is proportional to *JDOS*, the *JDOS* of

SWNTs can be obtained by studying its *RBM* features. The Raman spectra intensity $I(E_l)$ is closely related to the laser excitation energy (E_l) which can be described below:

$$I(E_l) = \int \left| M \frac{g\,(E)}{(E_l - E - i\Gamma_r)(E_l \pm E_{ph} - E - i\Gamma_r)} \right|^2 dE \qquad 1.7$$

$$g(E) = Re\left[\sum_i \frac{a_{C-C}E}{d_t \gamma_0 \sqrt{(E - E_{ii} - i\Gamma_J)(E + E_{ii} + i\Gamma_J)}} \right] \qquad 1.8$$

$$M = M_i M_{ep} M_s \qquad 1.9$$

E_{ph} can be obtained from the *RBM* peaks. The band gap of SWNTs (E_{ii}) can be derived from equation 1.7 based on the data from *RBM* features. As the diameter can be obtained from equation 1.6 and E_{ii} can be got from equation 1.7, the possibilities of SWNTs chirality can be estimated. Therefore, the diameter, electronic structure, and chirality of SWNTs can be obtained by measuring the *RBM* frequency and intensity.

***D*-Modes**

Graphene and SWNTs are composed of carbon rings which contain 6 atoms in each ring. All these six carbon atoms symmetrically breath which is shown in Figure 1.16. In the perfect graphene or SWNTs without defects, there is no Raman resonance features. When the ring is destructed by functional groups or sp^3 bonds, the *D* peak will be active and can be probed by Raman spectroscopy. In both graphene and SWNTs, the *D* peak is at 1360 cm^{-1} for visible excitation.[32, 42-43 38]

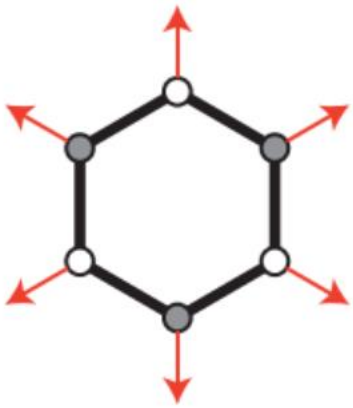

Figure 1.16 *D* modes of graphene. [38]

The *D* band originates from inter-valley one-phonon double resonance (*DR*). Raman scattering process between two nonequivalent Dirac cones (*K* and *K'*) as shown in Figure 1.17.[43] Briefly, it involves four processes: 1) the laser excites the sample and produce an electron/hole pair; 2) the electron is scattered by a phonon with an exchanged momentum *q*~*K*; 3) defect scattering; 4) electron/hole recombination. Therefore, the *D* peak is the result of second-order Raman scattering process.[32, 42]

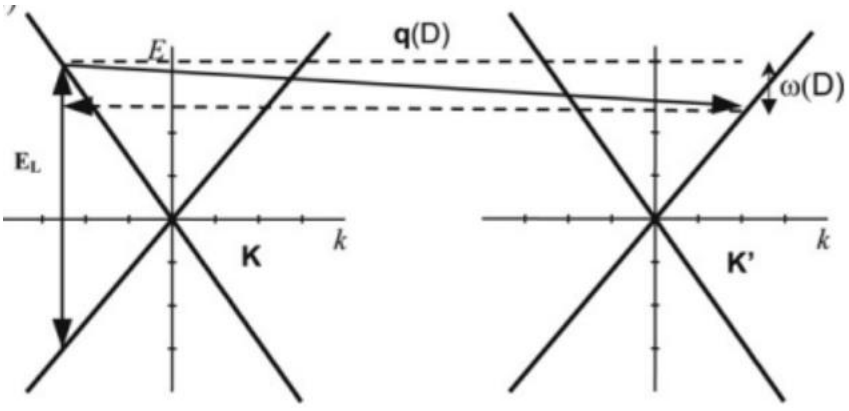

Figure 1.17 The double resonance processes.[43]

***IFM* modes**

The *G* band and *RBM* band are due to the first-order Raman scattering process, while the *D* band is due to one-phonon double resonance. When combine these modes, it will produce some weak Raman features in the intermediate-frequency region from 600 to 1100 cm^{-1} in the SWNT Raman spectroscopy, which is named as intermediate-frequency modes (*IFM*).[44] In literature, a Raman active feature at around 860 cm^{-1} was observed in electric-arc SWNTs which is related to the out-of-plane transverse optical (*oTO*) phonon branch in graphene (Figure 1.18).[44]

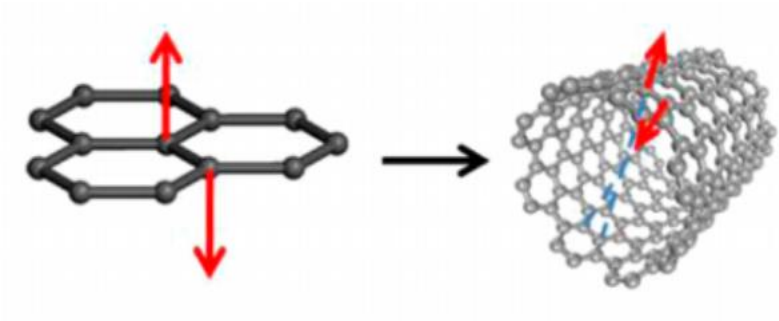

Figure 1.18 Schematic diagram of *oTO* phonon vibration in graphene and SWNT.[44]

The *IFM* features in SWNTs are associated with the combination of zone folded oTO and in-plane transverse acoustic *iTA* in graphene, which produce IFM^+ and IFM^- above and below *oTO*, respectively.[45] The frequency of *IFM* can be calculated by the sum and difference of phonon frequencies described as below[46]:

$$\omega_{IFM}^{+} = \omega_{oTO} + \omega_{iTA} \qquad 1.10$$

$$\omega_{IFM}^{-} = \omega_{oTO} - \omega_{iTA} \qquad 1.11$$

In the Raman scattering process for the SWNTs, the phonons usually interact with electronic states in E_{ii} in the valence band and conduction band. However, when the

energies of E_{ii} and E_{ii}'' are very close, it is possible that the electron excited in E_{ii} state is scattered by a phonon to E_{ii}'' state. The *IFM* features are from the Raman resonance absorption and emission between E_{33} and E_{44} states in semiconducting SWNTs while in the $M_{11}^{M^-}$ and M_{11}^{+} for metallic SWNTs. The electrons can only interact with phonons with E_3 symmetry in semiconducting SWNTs to meet the angular momentum conservation. Based on the Raman selection rules, the E_3 symmetry modes can't be probed in the first order Raman scattering process but can be observed in a second-order scattering process involving two E_3 phonons. One is from the folding of optical branch and another one is from the folding of an acoustic branch in 2D graphene.

In order to activate Raman scattering process, the linear momentum along the tube axis and angular momentum conservation are needed to meet the requirement. For the linear momentum conservation, it requires:

$$\left|q_{phonon}\right| = \left|k_f - k_i\right| \qquad 1.12$$

where q_{phonon} is the phonon wave vector along the tube axis, k_f and k_u are the electronic wave vectors of final and initial electronic states. In SWNTs, f=4, and i=3.

So when $q_{phonon} \to 0$, $k_4 \approx k_3$ and θ≈0. When $q_{phonon} \equiv 0$, $k_4 = k_3$ and θ=0. Therefore, the *IFM* features can only be observed near or in zigzag SWNTs $(n,0)$.[45-47]

The frequencies of *IFM* features are associated with the diameters of SWNTs, showing decreasing trend with the decrease of SWNTs diameter. In SWNTs, the intensity of ω_{IFM}^{+} peaks is higher than the ω_{IFM}^{-} as ω_{IFM}^{+} is related to acoustic mode stoke process while the ω_{IFM}^{-} is associated with the less probable acoustic mode anti-stokes process.

1.4 Growth of SWNTs

Since the first carbon nanotube was discovered in 1991,[3] various techniques have been developed to grow SWNTs for different applications. The most common techniques are arc-discharge method[9], laser ablation (*LA*),[48] and chemical vapor deposition (CVD),[49] Even though most of these techniques have been improved in the past 2 decades, all the as-prepared SWNTs contain impurities like amorphous carbon, catalyst and graphitic nanoparticles. Therefore, purifying processes are needed to get high-purity SWNTs. Also, it is still a challenge to precisely control SWNT diameter, chirality, and length during the synthetic process.

1.4.1 Electric Arc-Discharge Method

Electric arc-discharge method has been initially used to produce fullerene.[50] Usually, a discharge direct current (80-200 A) is running between two high-purity graphite rods, working as cathode and anode, and separated by 1~2 mm under inert gas like He or Ar atmosphere. Carbon nanomaterials like fullerene and graphitic nanoparticles are deposited on the electrode (Figure 1.19). [19]

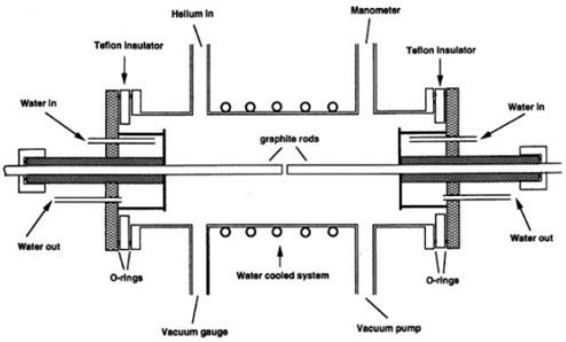

Figure 1.19 Schematic of the arc-discharge apparatus employed for carbon nanomaterials production (Fullerene, SWNTs, MWNTs).[19]

Sumio Iijima first synthesized SWNTs by arch discharge method in 1993.[9] Iron metallic catalyst was filled into the graphite cathode, and the chamber was filled with the mixture of methane and argon. After the reaction with the direct current of 200 A at 20 V, MWNTs were found on the graphite cathode, while SWNTs were grown in gas. The diameters of SWNTs were in the range of 0.7 nm and 1.6 nm.

C. Journet prepared SWNTs in large-scale by the electric arc-discharge method, in which anode was made out of graphite rod with a drilled hole filled with a mixture of metallic catalyst and graphite powder, while another graphite rod worked as cathode. A direct current (100 A) was applied between the cathode and anode to vaporize the graphite anode. The anode electrode was continuously translated to keep a constant distance between the two graphite electrodes.[51] Large amounts of carbon nanotubes were found on the cathode. SEM image of the SWNT material is shown in Figure 1.20. The synthetic process also produces spherical nanoparticles ranging from 3 nm to 20 nm in diameter.[19, 51]

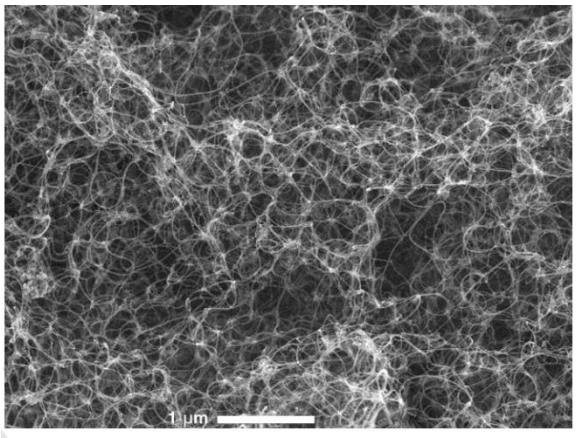

Figure 1.20 Scanning electron microscopy (SEM) image of SWNTs produced by arc-discharge method. [51]

Nowadays, SWNTs can be produced by arc-discharge method with many types of metal catalysts with high yields and a narrow range of diameters of SWNTs. The SWNTs produced by arc-discharge method show high crystallinity and quality.[52-54] However, even best synthesis also produces some impurities like amorphous carbon, graphite, encapsulated metal particles.

1.4.2 Laser Ablation Method

Laser ablation method needs a high-power laser to vaporize the high-purity graphite target in a furnace at high temperature (Figure 1.21). In order to produce SWNTs, metal catalysts are needed to be added to the graphite target. Even though laser ablation method can produce multi- or single-walled carbon nanotube with high quality, it still has some drawbacks like high cost and low yield.[19, 55]

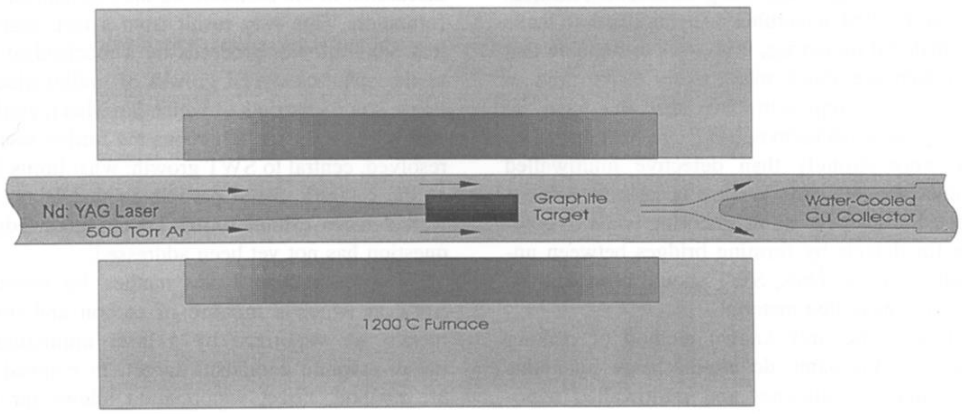

Figure 1.21 Experimental setup for the production of SWNTs and MWNTs using the laser technique.[19]

1.4.3 Chemical Vapor Deposition Method

CVD is one of the most common techniques used to produce nanomaterials like ZnO nanowire, graphene, and MoS_2.[56-58] For the CNT synthesis, catalysts like Fe_2O_3

nanoparticles were deposited on a substrate and heated at high temperature in hydrocarbon gas (e.g., methane, benzene, acetylene, etc.) atmosphere. Hydrocarbon gas will be decomposed at high temperature on the surface of metal catalyst, resulting in producing H_2 and C_n species. The C_n species were absorbed into metal catalyst on the substrate to form a carbon-iron solid state solution. When carbon atoms reach supersaturation in metal catalyst, it will precipitate out of the metal and form SWNTs. The diameters of SWNTs are closely determined by the size of catalyst particles.[18-19, 49] Like in arc-discharge and laser ablation methods, CVD can grow single- and multi-walled carbon nanotubes. It can produce SWNTs at lower temperature (550-1000ºC) which make it easier and cheaper than other methods.[18] Furthermore, CVD method can be used to grow aligned SWNTs arrays under suitable condition.[59] However, the CVD method also has some disadvantages like more defects in SWNTs. At present, by changing parameters like catalyst and carbon source, carrier gas, particle size, temperature, large quantities of SWNTs can be produced with high purity, crystallinity, and efficiency.

1.5 Processing of SWNTs

1.5.1 Purification of SWNTs

The perfect structure of SWNTs makes it an outstanding material which can be used in various fields. However, there is significant amount of impurities in as-prepared SWNTs (AP-SWNTs) including metal catalyst and amorphous carbon, graphitic nanoparticles and fullerenes, which limits the applications of SWNTs in various fields. To totally fulfill the technological potential of the SWNTs, the first and most important

step is to develop method and process to purify the material. Haddon research group has put much effort to purify SWNTs and develop standard method to characterize its purity. The hierarchical flow chart presented in Figure 1.22 shows multiple purification stages starting with removing impurities and ending with sorting pure SWNTs by their length, chirality and diameter.[60]

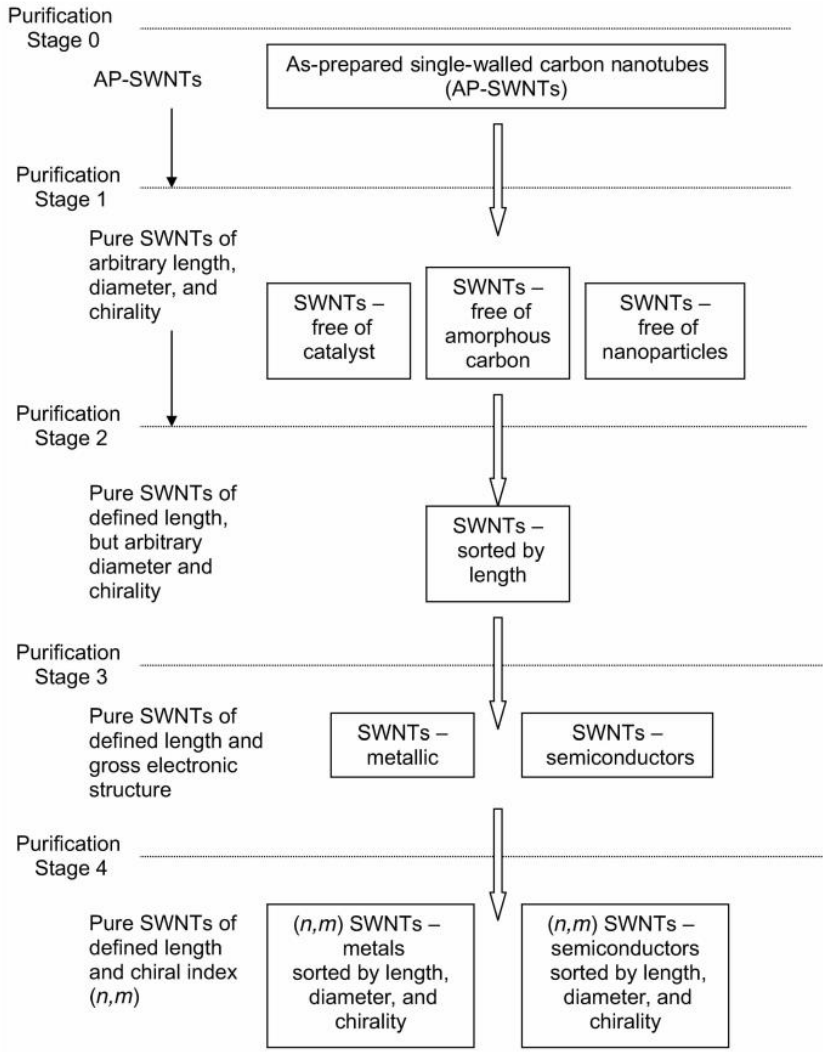

Figure 1.22 Hierarchical flow chart for purification of single-walled carbon nanotube (SWNTs).[60]

Up to now, much work has been done to remove the impurities in stage 1 and a promising progress has been achieved. Usually the purification strategies involve physical, chemical methods, or combination them together. As SWNTs physical properties are different with the impurities, like size, density, solubility in solvent, magnetic properties, etc.., the impurities can be removed by filtration, centrifugation, high-temperature annealing treatment, and dispersing in different solvents. Physical methods are usually combined with chemical methods.

Chemical methods mainly involve selective oxidation of carbonaceous impurities and the removal of the catalyst by acid. The carbonaceous impurities produced during SWNTs growth can be removed by oxidation in different gas atmospheres, such as O_2, mixture of Cl_2, H_2O and HCl, and a mixture of Ar, O_2 and H_2O. Significant development of purification techniques was conducted in the past by Haddon research group. For example, Rahul Sen et al.[61] Annealed arc-discharge produced SWNTs thin film at different temperatures and for different times in air to oxidize the impurities. In this experiment, the purity of SWNTs was evaluated by near-infrared (NIR) spectroscopy, and the result shows that SWNTs thin film has highest relative purity when SWNTs thin film was annealed at 245 ^oC for 12h under flowing oxygen atmosphere.[61] Hui Hu et al.[62] Purified arc-discharged produced SWNTs by nitric acid and characterized it by NIR spectroscopy. It was found that the concentration of nitric acid and reflux time have great influence on the purity and yield of the SWNTs. Nitric acid can efficiently remove metallic catalyst but also can damage the SWNTs and produce carbonaceous impurities at the same time. When SWNTs is treated by 3 M nitric acid for 12h or 7 M for 6 h, the

purification was found to be the most efficient.[62] As there are some carbonaceous impurities and carbon nanoparticles left in SWNTs after acid treatment, it is necessary to take further steps to remove these impurities. To achieve large-scale removal of impurities in SWNTs, Aiping Yu et al. combined low-speed and high-speed centrifugation methods together to remove amorphous carbon and carbon nanoparticles in nitric-acid treated SWNTs dispersion (Figure 1.23).[63] At low-speed centrifugation (2000 g), amorphous carbon is suspended preferentially in dispersion and can be removed by decanting, while after the high-speed centrifugation carbon nanoparticles precipitate, leaving SWNTs suspended in aqueous solution.

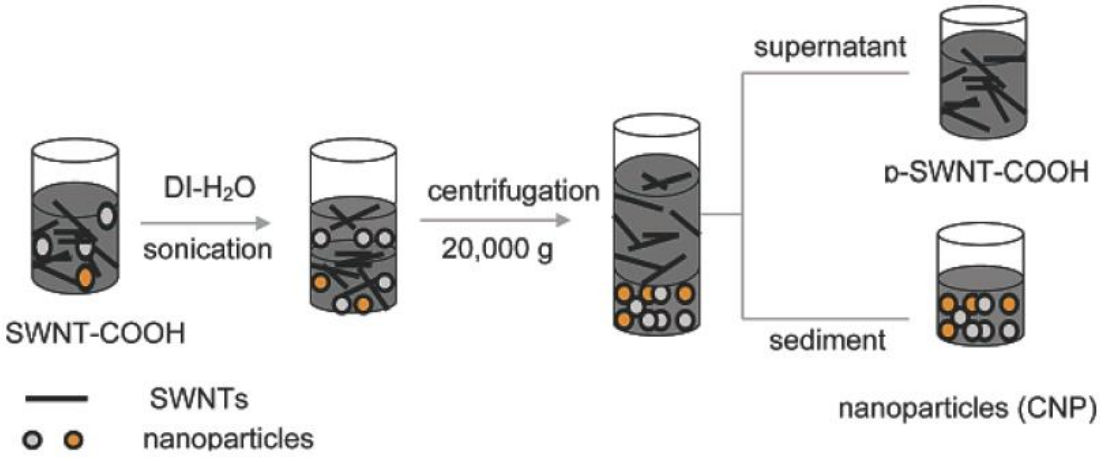

Figure 1.23 Schematic diagram of the resuspension - centrifugation - decantation cycle for removal of carbon nanoparticles.[63]

1.5.2 Measuring Purity of SWNTs

For improving synthesis and purification of the SWNTs it is important to measure the SWNTs purity at each step of the process as a function of synthetic and purification parameters. The weight of transition-metal catalyst can be measured by

thermogravimetric analysis (TGA). However, the real difficulty is to assess the carbonaceous purity. In the early work, the purity of SWNT is mainly assessed by transmission electron microscopy (TEM)[64] and scanning electron microscopy (SEM),[65-66] and these microscopy techniques were regarded as the standard measure of purity. However, SEM is just a local probe which can measure pictograms of sample, and it is impossible to measure gram-scale of samples, let alone the kilogram quantities. Moreover, the material quality varies widely within the samples, even in the same batch. Therefore, SEM is not a suitable technique to measure the purity of SWNT in large scale.[60-62, 67]

In order to achieve a standard measurement of SWNTs purity, Haddon research group developed near-infrared (NIR) spectroscopy method to estimate the purities of SWNTs produced by electric-arc method.[53] This technique is also suitable for the analysis of SWNTs produced by other method like CVD, HiPCO, and laser ablation.[53, 60-61, 63, 67-68] This technique was later accepted by NIST as one of the most efficient purity evaluation technique.[69]

Figure 1.24 shows a schematic of absorption spectrum of a typical SWNT material produced by electric-arc method in the spectral range between far-IR to UV (10-4500 cm^{-1}).[53, 61, 67] In the high energy spectral range, π-plasmon of the SWNTs and carbonaceous impurities mainly contribute to the absorption, while the NIR-visible spectral range exhibits absorption features originating from the interband transitions of semiconducting SWNT (S_{11} and S_{22}) and metallic SWNTs (M_{11}). S_{11} absorption band is extremely susceptible to chemical dopants and the M_{11} is weaker than S_{22}, so S_{22} is chosen to estimate the purity of the SWNTs (Figure 1.24).

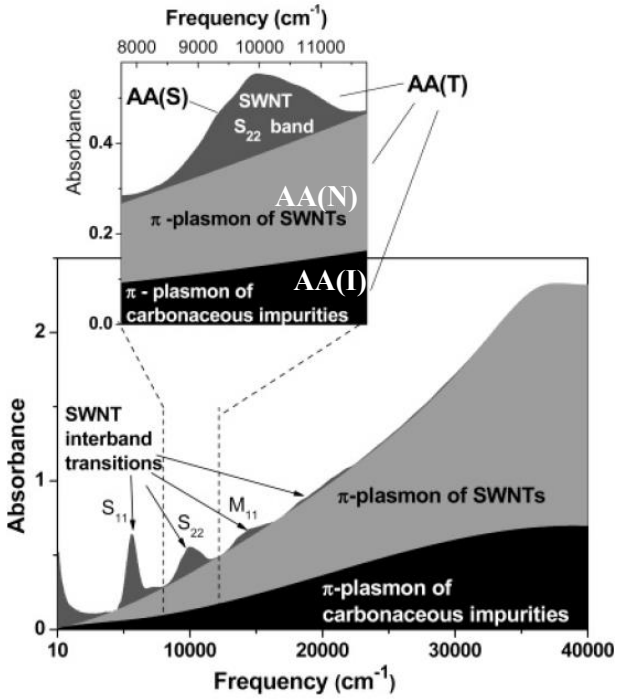

Figure 1.24 Schematic illustration of the electronic spectrum of SWNTs prepared by electric arc method.[53]

As shown in Figure 1.24, the areal absorption within S_{22} band was denoted as *AA(S)*, π-plasmon absorption from the SWNTs was denoted as *AA(N)* and from impurities is *AA(I),* and the total absorption was denoted as *AA(T),* where *AA(T) = AA(S)+AA(N)+AA(I).*

The relative purity of SWNT against the experimentally selected reference sample was defined as follows:

$$RP\ (Sample) = \frac{AA\ (S)_{Sample}/AA(T)_{Sample}}{AA(S)_{Reference}/AA(T)_{Reference}} \qquad 1.13$$

where $AA(S)_{Sample}$ and $AA(T)_{Sample}$ are the total areas of the NIR-UV curves in Figure 1.24. $AA(S)_{Reference}$ and $AA(T)_{Reference}$ are the areas under the S_{22} absorption in reference sample, respectively. In the experimentally selected reference sample, the ratio of $AA(S)_{Reference}$

$/AA(T)_{Reference}$ was measured as 0.141, and was assigned to the 100% relative purity of SWNTs. This purity evaluation technique was utilized for improving arc-discharge synthesis of SWNTs and improving efficiency of their purification.[25, 53, 61-63, 70-71] Later, this technique was utilized by commercial company Nanointegris, Inc. in separation of metallic and semiconducting SWNTs described in the next section.

1.5.3 Separation of Semiconducting and Metallic SWNTs

SWNTs have excellent electrical and optical properties leading to the wide range of potential applications, especially in electronic industry. However, the SWNTs in large scale synthetic production are naturally grown as bundles of a mixture of metallic and semiconducting tubes in a ratio of 1:2, thus hindering widespread applications of SWNTs. Up to now, much effort has been put to separate semiconducting from metallic SWNTs. For example, Krupke et al. prepared thin film of metallic SWNT by electrophoresis on the interdigitated chips. However, this technique can only be applied on the small.[72] Takeshi Tanaka et al. reported a rapid and scalable method to separate metallic and semiconducting SWNTs by selective adsorption of SWNTs on agarose gel. Briefly, the well-dispersed SWNTs/ sodium dodecyl sulfate solution was mixed with liquid agarose gel followed by the frozen, thawed, and squeezed processes. The resulting solution contains 70% pure metallic SWNTs, leaving the gel containing 95% pure semiconducting SWNTs (Figure 1.25).[73]

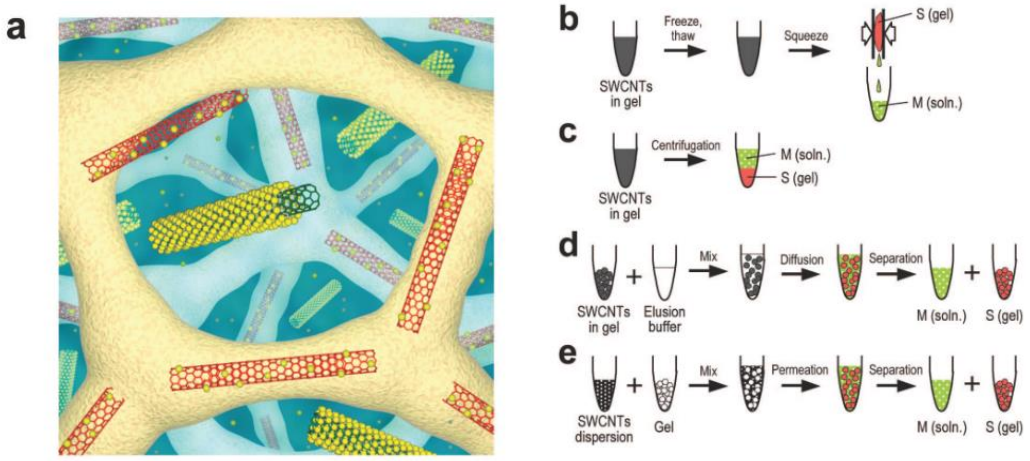

Figure 1.25 (a) Model of metallic and semiconducting SWNTs separation using agarose gel. Red: semiconducting SWNTs; beige, agarose gel matrix; green: metallic SWNTs; yellow: SDS. (b - e) Schematic diagrams showing steps of metallic and semiconducting SWNTs separation using agarose gel: (b) freeze and squeeze, (c) centrifugation, (d) diffusion, and (e) permeation. M, metallic SWCNT; S, semiconducting SWCNT.[73]

Hersam group developed a density-gradient ultracentrifugation technique for separating SWNTs by diameter, bandgap, and electronic type (metallic versus semiconducting SWNTs), which was later applied to large-scale and effective industrial production.[74-75] They first utilized DNA as a surfactant and dispersed SWNTs in iodixanol solutions followed by the ultracentrifugation at 174 000 g.[74] For this method, it has some drawbacks like the limited stability of DNA-wrapped SWNTs in solution, the removal of DNA, and the cost of DNA, which hindered their widespread applications. To overcome these drawbacks and achieve large-scale sorting of the SWNTs at low cost, they improved the density-gradient ultracentrifugation by replacing DNA surfactant with bile salts.[74] SWNTs were dispersed in bile salt solutions like sodium cholate (SC) via

ultrasonication method to obtain well-dispersed solutions of individual SWNTs. Unlike the anionic-alkyl surfactants such as sodium dodecyl sulphate (SDS) and sodium dodecylbenzene sulphonate (SDBS), the bile salt like SC is more molecularly rigid and is capable to form encapsulation layers on SWNTs. Moreover, metallic SWNTs show stronger interaction with adsorbates via π interaction than semiconducting SWNTs because of their larger electronic polarizability. Therefore, SWNTs with different chirality will be sorted under ultracentrifugation according to their various buoyant densities in solution (Figure 1.26). Density-gradient ultracentrifugation technique was the 1st method to achieve large-scale separation of MT- and SC-SWNTs at the purity exceeding 99%, and it utilizes NIR purity evaluation technique to measure the degree of separation. It was later commercialized through Nanointegris, Inc.

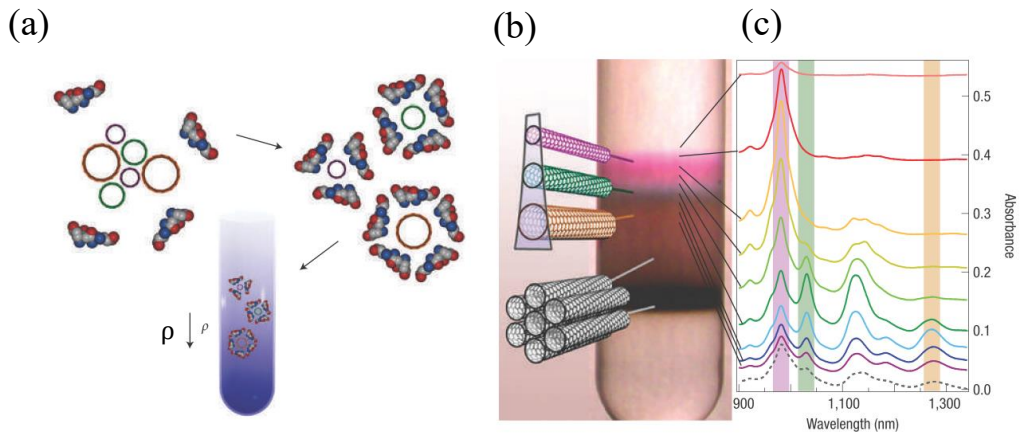

Figure 1.26 (a) Schematic of surfactant encapsulation and sorting of SWNTs, where ρ is density; (b) Photographs and optical absorbance (c) spectra after separation using density gradient ultracentrifugation.[75]

Currently, conjugated polymer wrapping method became the dominant sorting technique as it shows more advantages than other techniques, such as higher SWNT concentration, less excess dispersants and no ionic component. It is also easier to prepare SWNT thin films following such sorting.[76] Malefant group used 9,9-dialkylfuorene homopolymers (PFs) as surfactant to disperse large-diameter SWNTs in toluene by horn sonication.[77] During the sonication process, SWNTs will be exfoliated from large bundles and wrapped by polymer to form stable dispersion. The non-dispersed SWNTs or SWNTs with large bundles are removed during the centrifugation, leaving the enriched SC-SWNTs in solution. The unbound polymers in SWNT solution can be washed away by toluene via filtration method. In this study, they explored the factors that affect the enrichment like molecular weight, polymer side chain length, and the polymer/SWNT weight ratio. After centrifugation, the resulting solution contains more than 99% semiconducting (SC-) SWNTs with a yield of 5-10%. A multiple extraction process can be applied to increase the yield and maintain the purity of SC-SWNTs.

1.6 SWNTs Thin Film Preparation

1.6.1 Vacuum-Filtration Method

SWNTs show unique structure and outstanding electronic and optical properties. However, it is difficult to manupulate devices with individual SWNT on the industrial scale due to the technology limitation and low efficiency. An alternative approach is SWNT thin film based devices. Carbon nanotube thin films hold great potential for next-generation electronic devices due to their unique properties. For example, metallic SWNT thin film show high conductivity and transparency which can be applied in

flexible displays, battery electrodes, solar cells and supercapacitors.[78-79] Semiconducting SWNTs thin films can work as active materials for sensors, transistors, photodetector, and light emission devices (LED).[80] Many techniques have been developed to prepare high-quality SWNTs thin film. Rinzler group fabricated thin and transparent thin film by vacuum filtration method.[81] SWNTs were firstly dispersed in surfactant-based solution and then filtered through a membrane leading to the formation of the uniform SWNTs thin film. The SWNTs thin film can be transferred from the membrane onto any substrate by dissolving away the membrane in solvent (Figure 1.27).

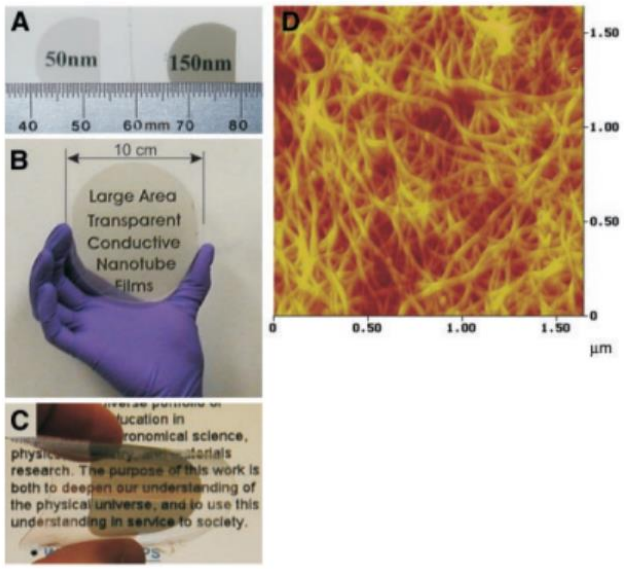

Figure 1.27 Transparent SWNT films on various substrates. (A) on quartz substrates; (B) on a sapphire substrate ; (C) on a Mylar sheet. (D) AFM image of a 150-nm SWNTs film.[81]

1.6.2 Casting Method

Chuan Wang et al. functionalized SiO_2 wafer surface by aminopropyltriethoxy silane (APTES), which resulted in formation of the amine-terminated monolayer. After that the

wafer was immersed into SWNTs solution containing 95% semiconducting SWNTs. After removing the wafer, the nanotube density on APTES functionalized wafer was much higher (24-32 tubes/μm^2) than the wafer without APTES (<0.5 tube/μm^2) (Figure 1.28). This method achieved wafer-scale SWNTs thin film preparation with high density uniform network, and high yield.[82]

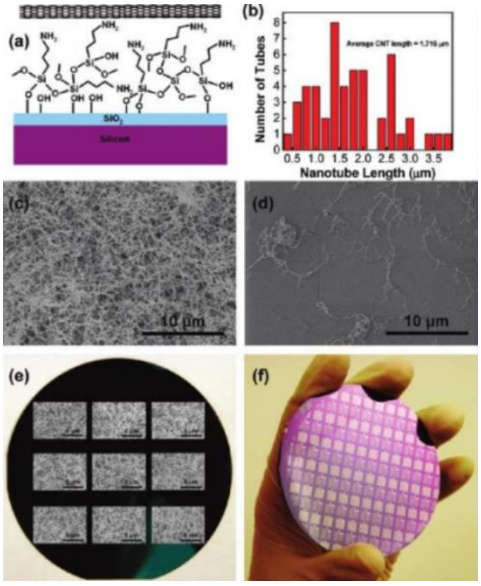

Figure 1.28 (a) Schematic diagram of APTES assisted nanotube deposition on Si/SiO_2 substrate. (b) Length distribution of the separated nanotubes; the average nanotube length is 1.716 μm. (c, d) FE-SEM images of separated nanotubes deposited on Si/SiO_2 substrates with (c) and without (d) APTES functionalization, respectively. (e) Photograph of 3 in. Si/SiO_2 wafer after APTES assisted nanotubes deposition. Inset: FE-SEM images showing nanotubes deposited at different locations on the wafer, the locations of the SEM images on the wafer correspond to the approximate locations on the wafer where the images were taken. All the scale bars are 5 μm. (f) Photograph of the same wafer after electrode patterning.[82]

1.6.3 CVD Method

Kono group grew vertical SWNT arrays by chemical vapor deposition (CVD), and the rolled down to form films of horizontally aligned SWNTs thin film which can be transferred on any subsrtrate (Figure 1.29). The SWNT arrays produced by CVD method are the mixture of semiconducting and metallic tubes, it is not suitable to preparation of the devices based on semiconducting SWNTs thin film.[83-84]

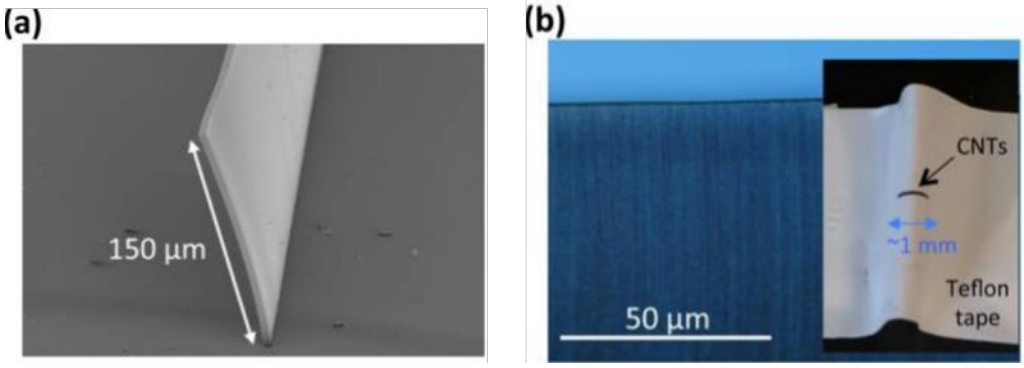

Figure 1.29 (a) Scanning electron microscopy image of vertically aligned CNTs grown on a silicon substrate. (b) An optical microscope image of horizontally aligned CNTs after transfer to a Teflon substrate.[83]

There are also some other techniques to prepare SWNTs thin film like dry transferring method, printing method and spraying method.[85-86] In our group, we prepared most of SWNT thin films by vacuum filtration method as described above (Figure 1.30), as it has much more advantages than other methods such as:

1) Homogenous SWNTs thin film can be fabricated with high efficiency;

2) The thickness of SWNTs thin film can be controlled by the amount of SWNTs;

3) Uniform thin film with different bundles can be prepared by changing the paremeters like filtration rate, pore size of membrane, and the surfactant concentration;

4) The membrane can be easily washed away without residue and the thin film can be transferred on any substrate.

(a) 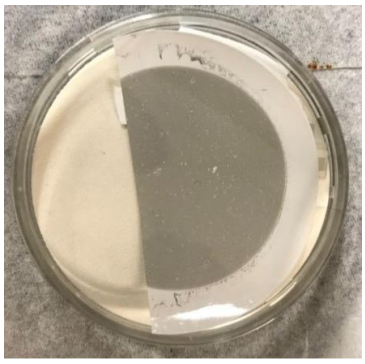 (b) 

Figure 1.30 Metallic SWNTs (a) and semiconducting SWNTs (b) thin film on membrane prepared by vacuum-filtration method.

To prepare SWNT thin films with small bundles, the casting method has been used as described in published reports.[76] SWNTs wrapped by conjugated polymer (PFDD) from National Research Council Canada were dispered in tolunene and sonicated by bath sonicator for 10 min to obtain PFDD/SWNT dispersion.[76] To clean and obtain the negatively charged substrate, SiO_2 wafer was treated by UV-Ozone for 20 mins which resulted in improving the quality and density of the SWNT thin film. The well-dispersed PFDD/SWNT solution was spread on treated SiO_2 substrate for 15 min before rinsing by toluene and drying by nitrogen gas. The average bundles size of SWNTs is 3 nm measured by atomic force microscopy (AFM) as shown in Figure 1.31.

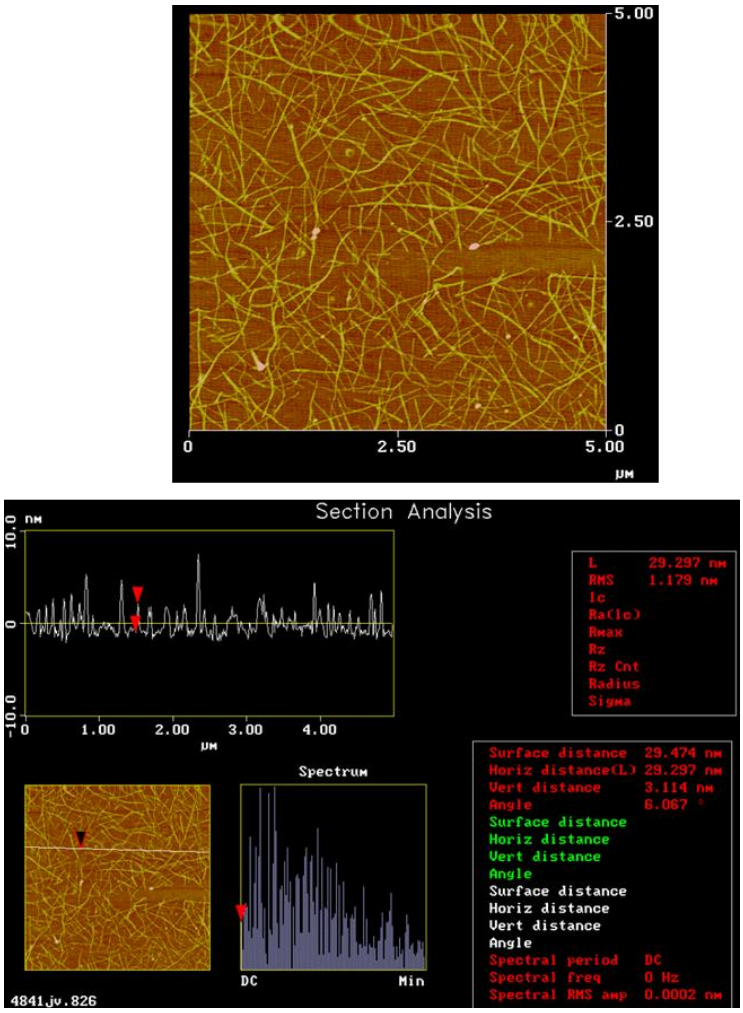

Figure 1.31 AFM image of SWNT thin film prepared by casting method.

1.7 Applications of the SWNTs Thin Film

1.7.1 Field-Effect Transistor (FET)

SC-SWNT is a semiconductor with high mobility and transiconductance. FET is the basic unit of the logic circuits. Compared with current FET channel materials, such as polysilicon, amorphous silicon, and some organic materials, SWNTs thin films have some advantages, including high trnasparency, easy to process, flexibilty, and

extraordinary electrical properties. Jialu Wang et al. achieved wafer-scale fabrication of SWNT thin film based FET devices with the on/off ratio > 10^4.[82] Gerald J. Brady *et al*. prepared FET based on aligned SWNTs thin film with on-state current as high as 900 μA μm^{-1}, which is similar or exceeds the Si FET at the equivalent gate oxide thickness and same off-state current density.[87] Chengguang Qiu *et al*. fabricated SWNT FET with a gate length of 5 nm performing better than the conventional silicon compementary metal-oxide semiconductor FET at the same scale (Figure. 1.32).[88]

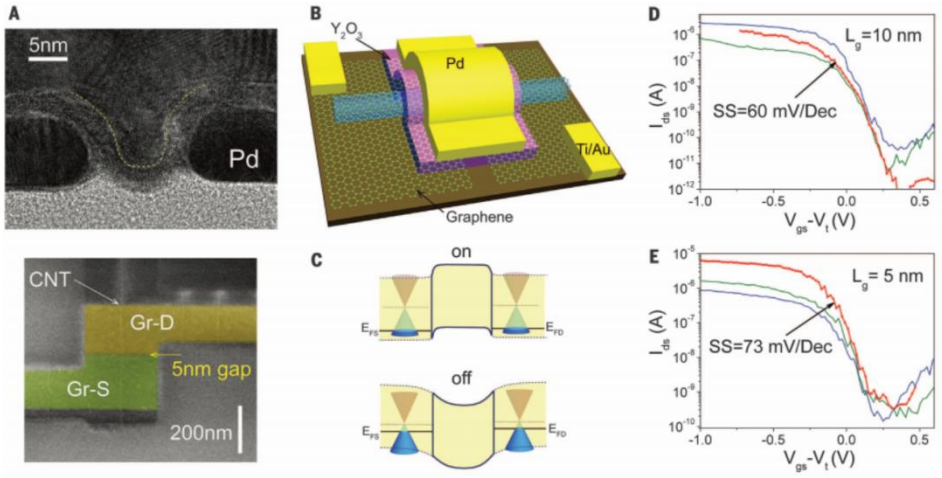

Figure 1.32 (A) TEM (top) and SEM (bottom) image of a Pd-contacted CNT FETwith gate length (*Lg*) of 5 nm. Schematic diagram showing the structure of a graphene-contacted (GC) CNT FET (B) and its band diagrams (C) in its on-state (top) and off-state (bottom). Transfer characteristics of GC CNT FETs with *Lg* = 10 nm (D) and 5 nm (E). [88]

1.7.2 Photodectors Based on SWNTs Thin Films

SWNTs thin films have great potential for applications in the next-generation opto-electronic devices. Itkis et al. developed suspended SWNT film technology, and it was found that the photoresponse of the suspended film was dramatically enhanced in vacuum

(Figure 1.33).[89] The photoresponse of the suspended SWNT film originated from the temperature rise under light irradiation which causes a decrease in resistance. Electron-phonon interactions lead to ultrafast relaxation of photoexcited carriers and the energy of incident infrared (IR) radiation is efficiently transferred to the crystal lattice. The suspended SWNTs thin film shows sufficiently high photoresponse and can work as the sensitive material of the IR bolometric detector. [89]

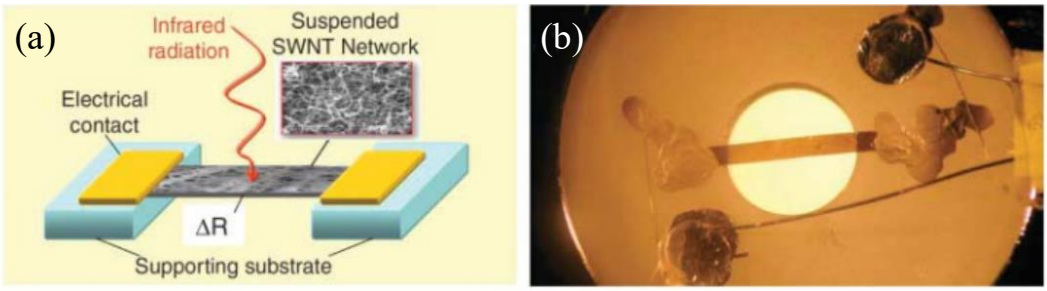

Figure 1.33 (a) Diagram of SWNT network suspended between electrical contacts. (b) 100-nm-thick SWNT film suspended across 3.5-mm opening of a sapphire ring.[89]

1.7.3 Light Modulators

Semiconducting SWNTs have unique opto-electronic properties. The interband transitions can be modulated using different doping methods. Moser et al. fabricated electro-optical modulator controlled by ionic liquid polarization.[90] Ionic liquid contains an extremely high density of cations and anions, which can be polarized by applying bias. When the ions surround the SWNTs, SWNTs are doped by electrons or holes, the Fermi level is shifting up and down, respectively, resulting in the light absorption change. By optimizing the thickness of semiconducting SWNT film and the type of counter-electrode material, the electro-optical modulator achieved high modulation depth of 3.7 dB and a fast operation with millisecond range (Figure 1.34).[90]

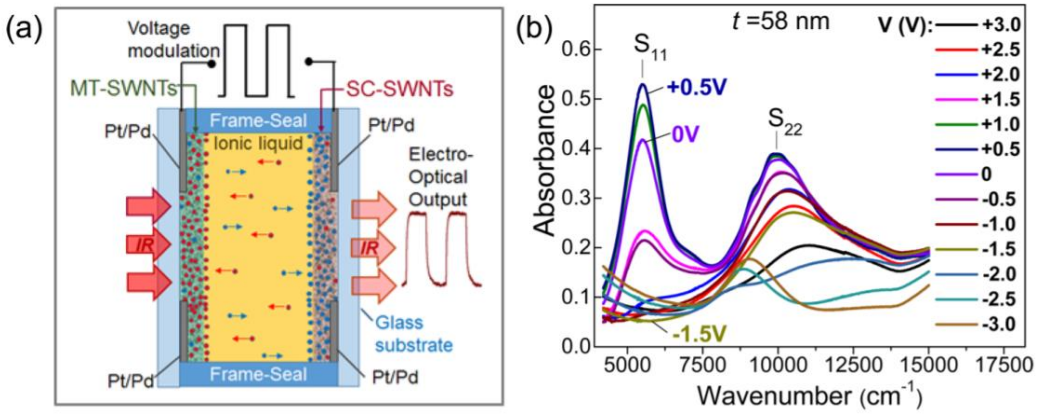

Figure 1.34 (a) Schematics of SWNT thin film based electrochromic cell with electro-optically active SC-SWNT electrode and MT-SWNT counter electrode. (b) Spectral modulation of SC-SWNT thin films with the thickness of 58 nm.[90]

1.7.4 Chemical Sensors

SWNTs are composed of one layer of carbon atoms with huge surface area which can absorb large quantities of gases on their surface. Moreover, SWNTs are very sensitive to chemical dopants due to their delocalized electronic structure, resulting in the change of the electric resistance and S_{11} optical absorption when absorb dopants.[91] Therefore, SWNTs have been viewed as extremely suitable candidate of active material for chemical sensors. Bekyarova et al. developed NH_3 gas sensor based on SWNTs chemically functionalized with poly(m-aminobenzene sulfonic acid) (SWNT-PABS). Compared with the purified SWNTs, SWNT-PABS based sensor has shown two times higher change in resistance upon the same exposure of NH_3.[91] Up to now, many types of gas sensors based on SWNTs have been fabricated and studied, including NO_2, NH_3, and H_2S. For increasing selectivity, SWNTs can also be functionalized with special groups to capture specific gas molecules.[92-95]

1.7.5 Solar Cells

As SWNTs have a strong absorption in near-infrared light and fast exciton and charge transport, they are promising light absorbers for devices related to light, such as photodetectors, transparent electrodes, and solar cells. As SC-SWNTs show p-type behavior, they can work as both active materials and transparent conducting electrodes in terms of solar cells. Up to now, much work has been done to prepare solar cells based on SWNT thin films to improve the conversion efficiency, such as separating metallic SWNTs to avoid exciton quenching, optimizing the nanotube bandgap distribution to increase external quantum efficiency.[96-97] [98] Michael S. Arnold group prepared solar cell using highly monochiral (7,5) SWNTs and C_{60}, which reach external quantum efficiency (*QE*) of 43% and power conversion efficiency of 0.95% and 1.02% at 1.0 and 1.5 suns.[99]

1.7.6 Transparent Electrodes

Grüner group developed a technique to transfer SWNT thin film on various substrates by combining transfer-printing method with filtration method.[86] Briefly, the SWNT thin film was firstly transferred from filtration membrane to patterned PDMS substrate by conformal contact followed by transferring SWNT film from PDMS to the desired substrate like SiO_2 wafer, PET, and PMMA. When the transmittance of SWNT thin films reaches 80%, the resistance is around 120 Ω, which is comparable to the commercial ITO films on plastic substrates.

During my research in UCR, I utilized SWNT thin film technology for various purposes. Using the SWNTs in a form of the thin film, I was able to study the encapsulation of sulfur in SWNTs by spectroscopic techniques as discussed in Chapter 2.

I have utilized the SC-SWNT thin film on ZnO substrate to fabricate SWNTs/ZnO heterojunction working as UV photodetector as discussed in Chapter 3. In my other work, I prepared SWNT thin films with small bundles by casting method and doped them into n-type by HfO_2 deposited by ALD method. By transferring p-type SWNT thin film on the top of n-type SWNT thin film, I obtained the p-n junction based on the SWNT thin films for applications in NIR photodetection.

References

(1) Kroto, H. W.; Heath, J. R.; O'Brien, S. C.; Curl, R. F.; Smalley, R. E. C60: Buckminsterfullerene. *Nature* **1985,** *318*, 162-164.

(2) Haddon, R. C.; Brus, L. E.; Raghavachari, K. Electronic Structure and Bonding in Icosahedral C60. *Chem. Phys. Lett.* **1986,** *125*, 459-464.

(3) Iijima, S. Helical Microtubules of Graphitic Carbon. *Nature* **1991,** *354*, 56-58.

(4) Horiuchi, S.; Gotou, T.; Fujiwara, M.; Asaka, T.; Yokosawa, T.; Matsui, Y. Single Graphene Sheet Detected in a Carbon Nanofilm. *Appl. Phys. Lett.* **2004,** *84* (13), 2403-2405.

(5) Haddon, R. C.; Hebard, A. F.; Rosseinsky, M. J.; Murphy, D. W.; Duclos, S. J.; Miller, B.; Fleming, R. M.; Siegrist, T.; Glarum, S. H.; Tycko, R. Fullerenes: Synthesis, Properties, and Chemistry of Large Carbon Clusters. In *ACS Symposium Series*; Hammond, G. S.; Kuck, V. J., Eds.; 1992; p 71.

(6) Niyogi, S.; Bekyarova, E.; Itkis, M. E.; McWilliams, J. L.; Hamon, M. A.; Haddon, R. C. Solution Properties of Graphite and Graphene. *J. Am. Chem. Soc.* **2006,** *128* (24), 7720-7721.

(7) Haddon, R. C. Graphene - The Mother of Two Dimensional (2-D) Materials. *Acc. Chem. Res.* **2013,** *46*, 2191-2192.

(8) Geim, A. K.; Novoselov, K. S. The Rise of Graphene. *Nat. Mater.* **2007,** *6*, 183-191.

(9) Iijima, S.; Ichihashi, T. Single-Shell Carbon Nanotubes of 1-nm Diameter. *Nature* **1993,** *363*, 603-605.

(10) Bethune, D. S.; Kiang, C. H.; de Vries, M. S.; Gorman, G.; Savoy, R.; Vazquez, J.; Bevers, R. Cobalt-Catalized Growth of Carbon Nanotubes with Single-Atomic-Layer Walls. *Nature* **1993,** *363*, 605-607.

(11) Bekyarova, E.; Kalinina, I.; Itkis, M. E.; Beer, L.; Cabrera, N.; Haddon, R. C. Mechanism of Ammonia Detection by Chemically Functionalized Single-Walled Carbon Nanotubes: In Situ Electrical and Optical Study of Gas Analyte Detection *J. Am. Chem. Soc.* **2007,** *129* (35), 10700-10706.

(12) Li, G.; Suja, M.; Chen, M.; Bekyarova, E.; Haddon, R. C.; Liu, J. L.; Itkis, M. E. Visible-Blind UV Photodetector Based on Single-Walled Carbon Nanotube Thin Film/ZnO Vertical Heterostructures. *ACS Appl. Mater. Interfaces* **2017,** *9*, 37094-37104.

(13) Rowell, M. W.; Topinka, M. A.; McGehee, M. D.; Prall, H. J.; Dennler, G.; Sariciftci, N. S.; Hu, L. B.; Gruner, G. Organic Solar Cells with Carbon Nanotube Network Electrodes. *Appl. Phys. Lett.* **2006,** *88* (23), 233506-3.

(14) Wang, F.; Itkis, M. E.; Bekyarova, E.; Haddon, R. C. Charge-Compensated, Semiconducting Single-Walled Carbon Nanotube Thin Film as an Electrically Configurable Optical Medium. *Nat. Photonics* **2013,** *7*, 459-465.

(15) Fu, C.; Oviedo, M. B.; Zhu, Y.; Cresce, A. v. W.; Xu, K.; Li, G.; Itkis, M. E.; Haddon, R.; Chi, M.; Han, Y.; Wong, B. M.; Guo, J. Confined Lithium–Sulfur Reactions in Narrow-Diameter Carbon Nanotubes Reveal Enhanced Electrochemical Reactivity. *ACS Nano* **2018,** *12*, 9775-9784.

(16) Durkop, T.; Getty, S. A.; Cobas, E.; Fuhrer, M. S. Extraordinary Mobility in Semiconducting Carbon Nanotubes. *Nano Lett.* **2004,** *4*, 35-39.

(17) Anilkumar, P.; Fernando, K. A. S.; Cao, L.; Lu, F. S.; Yang, F. C.; Song, W. L.; Sahu, S.; Qian, H. J.; Thorne, T. J.; Anderson, A.; Sun, Y. P. Noncovalent Interactions of Derivatized Pyrenes with Metallic and Semiconducting Single-Walled Carbon Nanotubes. *J. Phys. Chem. C* **2011,** *115* (22), 11010-11015.

(18) Dai, H. Carbon Nanotubes: Synthesis, Integration, and Properties. *Acc. Chem. Res.* **2002,** *35*, 1035-1044.

(19) Terrones, M. SCIENCE AND TECHNOLOGY OF THE TWENTY-FIRST CENTURY: Synthesis, Properties, and Applications of Carbon Nanotubes. *Annu. Rev. Mater. Res.* **2003,** *33*, 419-501.

(20) Charlier, J.-C.; Blase, X.; Roche, S. Electronic and Transport Properties of Nanotubes. *Rev. Mod. Phys.* **2007,** *79*, 677-732.

(21) Popov, V. N. Carbon Nanotubes: Properties and Application. *Mater. Sci. Eng. R* **2004,** *43*, 61-102.

(22) Avouris, P. Graphene: Electronic and Photonic Properties and Devices. *Nano Lett.* **2010,** *10* (11), 4285-4294.

(23) Itkis, M. E.; Niyogi, S.; Meng, M.; Hamon, M.; Hu, H.; Haddon, R. C. Spectroscopic Study of the Fermi Level Electronic Structure of Single Walled Carbon Nanotubes. *Nano Lett.* **2002,** *2*, 155-159.

(24) Odom, T. W.; Huang, J.-L.; Kim, P.; Lieber, C. M. Atomic Structure and Electronic Properties of Single-Walled Carbon Nanotubes. *Nature* **1998,** *391*, 62-64.

(25) Zhao, B.; Hu, H.; Niyogi, S.; Itkis, M. E.; Hamon, M.; Bhowmik, P.; Meier, M. S.; Haddon, R. C. Chromatographic Purification and Properties of Soluble Single Walled Carbon Nanotubes. *J. Am. Chem. Soc.* **2001,** *123*, 11673-11677.

(26) Rao, A. M.; Richter, E.; Bandow, S.; Chase, B.; Eklund, P. C.; Williams, K. A.; Fang, S.; Subbaswamy, K. R.; Menon, M.; Thess, A.; Smalley, R. E.; Dresselhaus, G.; Dresselhaus, M. Diameter-Selective Raman Scattering from Vibrational Modes in Carbon Nanotubes. *Science* **1997,** *275*, 187-191.

(27) Lemay, S. G.; Janssen, J. W.; van den Hout, M.; Mooji, M.; Bronikowski, M. J.; Willis, P. A.; Smalley, R. E.; Kouwenhoven, L. P.; Dekker, C. Two-Dimensional Imaging of Electronic Wavefunctions in Carbon Nanotubes. *Nature* **2001,** *412*, 617-620.

(28) Hamon, M. A.; Itkis, M. E.; Niyogi, S.; Alvaraez, T.; Kuper, C.; Menon, M.; Haddon, R. C. Effect of Rehybridization on the Electronic Structure of Single-Walled Carbon Nanotubes. *J. Am. Chem. Soc.* **2001,** *123*, 11292-11293.

(29) Kataura, H.; Kumazawa, Y.; Maniwa, Y.; Umezu, I.; Suzuki, S.; Ohtsuka, Y.; Achiba, Y. Optical Properties of Single-Wall Carbon Nanotubes. *Synth. Met.* **1999,** *103*, 2555-2558.

(30) Bekyarova, E.; Itkis, M. E.; Cabrera, N.; Zhao, B.; Yu, A.; Gao, J.; Haddon, R. C. Electronic Properties of Single-Walled Carbon Nanotube Networks. *J. Am. Chem. Soc.* **2005,** *127*, 5990-5995.

(31) Dresselhaus, M. S.; Dresselhaus, G.; Jorio, A.; Souza Filsho, A. G.; Pimenta, M. A.; Saito, R. Single Nanotube Raman Spectroscopy. *Acc. Chem. Res.* **2002,** *35*, 1070-1078.

(32) Dresselhaus, M. S.; Dresselhaus, G.; Saito, R.; Jorio, A. Raman spectroscopy of carbon nanotubes. *Phys. Rep* **2005,** *409* (2), 47-99.

(33) Dresselhaus, M. S.; Dresselhaus, G.; Jorio, A.; Souza, A. G.; Saito, R. Raman Spectroscopy on Isolated Single Wall Carbon Nanotubes. *Carbon* **2002,** *40* (12), 2043-2061.

(34) Dresselhaus, M. S.; Jorio, A.; Hofmann, M.; Dresselhaus, G.; Saito, R. Perspectives on Carbon Nanotubes and Graphene Raman Spectroscopy. *Nano Lett.* **2010,** *10* (3), 751-758.

(35) Saito, R.; Dresselhaus, G.; Dresselhaus, M. S. *Physical Properties of Carbon Nanotubes*, Imperial College Press: Singapore, 1998.

(36) Li, G.; Fu, C.; Oviedo, M.; Chen, M.; Tian, X.; Bekyarova, E.; Itkis, M. E.; Wong, B.; Guo, J.; Haddon, R. C. Giant Raman Response to the Encapsulation of Sulfur in Narrow Diameter Single-Walled Carbon Nanotubes. *J. Am. Chem. Soc* **2015,** *138*, 40 - 43, DOI: doi: 10.1021/jacs.5b10598.

(37) Wu, J. B.; Lin, M. L.; Cong, X.; Liu, H. N.; Tan, P. H. Raman Spectroscopy of Graphene-Based Materials and Its Applications in Related Devices. *Chem. Soc. Rev.* **2018,** *47*, 1822-1873.

(38) Ferrari, A. C.; Basko, D. M. Raman Spectroscopy as a Versatile Tool for Studying the Properties of Graphene. *Nature Nanotech.* **2013,** *8* (4), 235-246.

(39) Jorio, A.; Pimenta, M. A.; Souza, A. G.; Saito, R.; Dresselhaus, G.; Dresselhaus, M. S. Characterizing Carbon Nanotube samples with Resonance Raman Scattering. *New J. Phys*. **2003,** *5*.

(40) Maultzsch, J.; Telg, H.; Seich, S.; Thomsen, C. Radial Breathing Mode of Single-Walled Carbon Nanotubes: Optical Transition Energies and Chiral-Index Assignment. *Phys. Rev. B* **2005,** *72*, 205438.

(41) Jorio, A.; Souza Filho, A. G.; Dresselhaus, G.; Dresselhaus, M. S.; Saito, R.; Hafner, J. H.; Lieber, C. M.; Matinaga, F. M.; Dantas, M. S. S.; Pimenta, M. A. Joint Density of Electronic States for One Isolated Single-Wall Carbon Nanotube Studied by Resonant Raman Scattering. *Phys. Rev. B* **2001,** *63*, 245416.

(42) Saito, R.; Hofmann, M.; Dresselhaus, G.; Jorio, A.; Dresselhaus, M. S. Raman Spectroscopy of Graphene and Carbon Nanotubes. *Adv. Phys.* **2011,** *60*, 413-550.

(43) Ferrari, A. C. Raman Spectroscopy of Graphene and Graphite: Disorder, Electron-Phonon Coupling, Doping and Nonadiabatic Effects. *Solid State Commun.* **2007,** *143*, 47-57.

(44) Wang, J.; Yang, J.; Zhang, D.; Li, Y. Structure Dependence of the Intermediate-Frequency Raman Modes in Isolated Single-Walled Carbon Nanotubes. *J. Phys. Chem. C* **2012,** *116*, 23826-23832.

(45) Fantini, C.; Jorio, A.; Souza, M.; Laderia, L. O.; Souza Filho, A. G.; Saito, R.; Samsonidze, G. G.; Dresselhaus, G.; Dresselhaus, M. S.; Pimenta, M. A. One-Dimensional Character of Combination Modes in the Resonance Raman Scattering of Carbon Nanotubes. *Phys. Rev. Lett.* **2004,** *93*, 087401.

(46) Wang, J.; Yang, J.; Zhang, D.; Li, Y. Structure Dependance of the Intermediate-Frequency Raman Modes in Isolated Single-Walled Carbon Nanotubes. *j. phys. Chem. C* **2012,** *116*, 23826-23832.

(47) Fantini, C.; Jorio, A.; Souza, M.; Saito, R.; Samsonidze, G. G.; Dresselhaus, M. S.; Pimenta, M. A. Steplike Dispersion of the Intermediate-Frequency Raman Modes in Semiconducting and Metallic Carbon Nanotubes. *Phys. Rev. B.* **2005,** *72*, 085446.

(48) Guo, T.; Nikolaev, P.; Thess, A.; Colbert, D. T.; Smalley, R. E. Catalytic Growth of Single-Walled Nanotubes by Laser Vaporization. *Chem. Phys. Lett.* **1995,** *243*, 49-54.

(49) Cassel, A. M.; Raymakers, J. A.; Kong, J.; Dai, H. Large Scale CVD Synthesis of Single-Walled Carbon Nanotubes. *J. Phys. Chem. B* **1999,** *103* (31), 6484-6492.

(50) Kraetschmer, W.; Lamb, L. D.; Fostiropoulos, K.; Huffman, D. R. Solid C60: A New Form of Carbon. *Nature* **1990,** *347*, 354-358.

(51) Journet, C.; Maser, W. K.; Bernier, P.; Loiseau, A.; Lamy de la Chappelle, M.; Lefrant, S.; Deniard, P.; Lee, R.; Fischer, J. E. Large Scale Production of Single-Walled Carbon Nanotubes by the Electric-Arc Technique. *Nature* **1997,** *388*, 756-758.

(52) Saito, Y.; Tani, Y.; Miyagawa, N.; Mitsushima, K.; Kasuya, A.; Nishina, Y. High Yield of Single-Walled Carbon Nanotubes by Arc Discharge using Rh-Pt Catalysts. *Chem. Phys. Lett.* **1998,** *294*, 593-598.

(53) Itkis, M. E.; Perea, D.; Niyogi, S.; Rickard, S.; Hamon, M.; Hu, H.; Zhao, B.; Haddon, R. C. Purity Evaluation of As-Prepared Single-Walled Carbon Nanotube Soot by Use of Solution Phase Near-IR Spectroscopy. *Nano Lett.* **2003,** *3*, 309-314.

(54) Niyogi, S.; Hamon, M. A.; Hu, H.; Zhao, B.; Bhowmik, P.; Sen, R.; Itkis, M. E.; Haddon, R. C. Chemistry of Single-Walled Carbon Nanotubes. *Acc. Chem. Res.* **2002,** *35*, 1105-1113.

(55) Kokai, F.; Takahashi, K.; Yudasaka, M.; Iijima, S. Laser Ablation of Graphite-Co/Ni and Growth of Single-Wall Carbon Nanotubes in Vortexes Formed in an Ar Atmospere. *J. Phys. Chem. B* **2000,** *104*, 6777-6784.

(56) Yang, P.; Yan, H.; Mao, S.; Russo, R.; Johnson, J.; Saykally, R.; Morris, N.; Pham, J.; He, R.; Choi, H. Controlled Growth of ZnO Nanowires and Their Optical Properties. *Adv. Funct. Mater.* **2002,** *12*, 323-331.

(57) De Arco, L. G.; Zhang, Y.; Kumar, A.; Zhou, C. W. Synthesis, Transfer, and Devices of Single- and Few-Layer Graphene by Chemical Vapor Deposition. *Ieee Transactions on Nanotechnology* **2009,** *8* (2), 135-138.

(58) Zhang, W.; Huang, J. K.; Chen, C. H.; Chang, H. Y.; Cheng, Y. J.; Li, L. J. High-Gain Phototransistors Based on a CVD MoS_2 Monolayer. *Adv. Mater.* **2013,** *25*, 3456-3461.

(59) Joselevich, E.; Lieber, C. M. Vectorial Growth of Metallic and Semiconducting Single-Wall Carbon Nanotubes. *Nano Lett.* **2002,** *2*, 1137-1141.

(60) Haddon, R. C.; Sippel, J.; Rinzler, A. G.; Papadimitrakopoulos, F. Purification and Separation of Carbon Nanotubes. *MRS Bull.* **2004,** *29*, 252-259.

(61) Sen, R.; Rickard, S. M.; Itkis, M. E.; Haddon, R. C. Controlled Purification of Single-Walled Carbon Nanotube Films by Use of Selective Oxidation and Near-IR Spectroscopy. *Chem. Mater.* **2003,** *15*, 4273-4279.

(62) Hu, H.; Zhao, B.; Itkis, M. E.; Haddon, R. C. Nitric Acid Purification of Single-Walled Carbon Nanotubes. *J. Phys. Chem. B* **2003,** *107*, 13838-13842.

(63) Yu, A.; Bekyarova, E.; Itkis, M. E.; Fakhrutdinov, D.; Webster, R.; Haddon, R. C. Application of Centrifugation to the Large-Scale Purification of Electric Arc Produced Single-Walled Carbon Nanotubes. *J. Am. Chem. Soc.* **2006,** *128* (30), 9902-9908.

(64) Dujardin, E.; Ebbesen, T. W.; Krishnan, A.; Treacy, M. M. J. Purification of Single-Shell Nanotubes. *Adv. Mater.* **1998,** *10*, 611-613.

(65) Lian, Y.; Maeda, Y.; Wakahara, T.; Akasaka, T.; Kazaoui, S.; Minami, N.; Shimizu, T.; Choi, N.; Tokumoto, H. Nondestructive and High-Recovery-Yield Purification of Single-Walled Carbon Nanotubes by Chemical Functionalization. *J. Phys. Chem. B* **2004,** *108* (26), 8848-8854.

(66) Shelimov, K. B.; Esanaliev, R. O.; Rinzler, A. G.; Huffman, C. B.; Smalley, R. E. Purification of Single-Wall Carbon Nanotubes by Ultrasonically Assisted Filtration. *Chem. Phys. Lett.* **1998,** *282* (5,6), 429-434.

(67) Itkis, M. E.; Perea, D.; Jung, R.; Niyogi, S.; Haddon, R. C. Comparison of Analytical Techniques for Purity Evaluation of Single-Walled Carbon Nanotubes. *J. Am. Chem. Soc.* **2005,** *127*, 3439-3448.

(68) Huang, W. J.; Fernando, S.; Lin, Y.; Zhou, B.; Allard, L. F.; Sun, Y. P. Preferential Solubilization of Smaller Single-Walled Carbon Nanotubes in Squential Fnctionalization Ractions. *Langmuir* **2003,** *19* (17), 7084-7088.

(69) Arepalli, S.; Freiman, S. W.; Hooker, S., A,; Migler, K. D. Measurement Issues in Single-Wall Carbon Nanotubes. *NIST* **2008,** *Special Publication(NIST SP)-960-19*.

(70) Niyogi, S.; Hu, H.; Hamon, M. A.; Bhowmik, P.; Zhao, B.; Rozenzhak, S. M.; Chen, J.; Itkis, M. E.; Meier, M. S.; Haddon, R. C. Chromatographic Purification of Soluble Single-Walled Carbon Nanotubes (s-SWNTs). *J. Am. Chem. Soc.* **2001,** *123*, 733-734.

(71) Itkis, M. E.; Perea, D.; Niyogi, S.; Love, J.; Tang, J.; Yu, A.; Kang, C.; Jung, R.; Haddon, R. C. Optimization of the Ni-Y Composition in Bulk Electric Arc Synthesis of Single-Walled Carbon Nanotubes by Use of Near-Infrared Spectroscopy. *J. Phys. Chem. B* **2004,** *108*, 12770-12775.

(72) Krupke, R.; Linden, S.; Rapp, M.; Hennrich, F. Thin Film of Metallic Carbon Nanotubes Prepared by Dielectrophoresis. *Adv. Mater.* **2006,** *18*, 1468-1470.

(73) Tanaka, K.; Jin, H.; Miyata, Y.; Fujii, S.; Suga, H.; Naitoh, Y.; Minar, T.; Miyadera, T.; Tsukagoshi, K.; Kataura, H. Simple and Scalable Gel-Based Separation of Metallic and Semiconducting Carbon Nanotubes. *Nano Lett.* **2009,** *9*, 1497-1500.

(74) Arnold, M. S.; Stupp, S. I.; Hersam, M. C. Enrichment of Single-Walled Carbon Nanotubes by Diameter in Density Gradients. *Nano Lett.* **2005,** *5*, 713-718.

(75) Arnold, M. S.; Green, A. A.; Hulvat, J. F.; Stupp, S. I.; Hersam, M. C. Sorting Carbon Nanotubes by Electronic Structure Using Density Differentiation. *Nature Nanotech.* **2006,** *1* (1), 60-65.

(76) Li, Z.; Ding, J.; Lefebvre, J.; Malenfant, P. R. L. Surface Effects on Network Formation of Conjugated Polymer Wrapped Semiconducting Single Walled Carbon Nanotubes and Thin Film Transistor Performance. *Org. Electron.* **2015,** *26*, 15-19.

(77) Ding, J.; Li, Z.; Lefebvre, J.; Cheng, F.; Dubey, G.; Zou, S.; Finnie, P.; Hrdina, A.; Scoles, L.; Lopinski, G.; Kingston, C.; Simard, B.; Malenfant, P. Enrichment of Large-

diameter Semiconducting SWNTs by Polyfluorene Extraction for High Network Density Thin Film Transistor. *Nanoscale* **2014,** *6*, 2328-2339.

(78) Lu, F. S.; Wang, W.; Fernando, K. A. S.; Meziani, M. J.; Myers, E.; Sun, Y. P. Metallic Single-Walled Carbon Nanotubes for Transparent Conductive Films. *Chem. Phys. Lett.* **2010,** *497* (1-3), 57-61.

(79) Wang, W.; Fernando, K. A. S.; Lin, Y.; Meziani, M. J.; Veca, L. M.; Cao, L.; Zhang, P.; Kimani, M. M.; Sun, Y. P. Metallic Single-Walled Carbon Nanotubes for Conductive Nanocomposites. *J. Am. Chem. Soc.* **2008,** *130* (4), 1415-1419.

(80) Zhang, D.; Ryu, K.; Liu, X.; Polikarpov, E.; Ly, J.; Tompson, M. E.; Zhou, C. Transparent, Conductive, and Flexible Carbon Nanotube Films and Their Applications in Organic Light-Emitting Diodes. *Nano Lett.* **2006,** *6* (9), 1880-1886.

(81) Wu, Z.; Chen, Z.; Du, X.; Logan, J. M.; Sippel, J.; Nikolou, M.; Kamaras, K.; Reynolds, J. R.; Tanner, D. B.; Hebard, A. F.; Rinzler, A. G. Transparent, Conductive Carbon Nanotube Films. *Science* **2004,** *305*, 1273-1276.

(82) Wang, C.; Zhang, J.; Ryu, K.; Badmaev, A.; Arco, L.; Zhou, C. Wafer-Scale Fabrication of Separated Carbon Nanotube Thin-Film Transistors for Display Applications. *Nano Lett.* **2009,** *9*, 4285-4291.

(83) He, X. W.; Fujmura, N.; Loyd, M.; Erickson, K. J.; Talin, A. A.; Zhang, Q.; Gao, W. L.; Jiang, Q. J.; Kwawano, Y.; Hauge, R. H.; Leonard, F.; Kono, J. Carbon Nanotube Terahertz Detector. *Nano Lett.* **2014,** *14* (7), 3953-3958.

(84) He, X.; Wang, X.; Nano, S.; Cong, K.; Jiang, Q.; Kane, A.; Goldsmith, J. E. M.; Hauge, R. H.; Leonard, F.; Kono, J. Photothermoelctric p-n Junction Photodetector with

Instrinsic Broadband Polarimetry Based on Macroscopic Carbon Nanotube Films. *ACS Nano* **2013,** *7*, 7271-7277.

(85) Kaskela, A.; Nasibulin, A. G.; Timmermans, M. Y.; Aitchison, B.; Papadimitratos, A.; Tian, Y.; Zhu, Z.; Jiang, H.; Brown, D. P.; Zakhidov, A.; Kauppinen, E. I. Aerosol-Synthesized SWNT Networks with Tunable Conductivity and Transparency by a Dry Transfer Technique. *Nano Lett.* **2010,** *10*, 4349-4355.

(86) Zhou, Y. X.; Hu, L. B.; Gruner, G. A Method of Printing Carbon Nanotube Thin Films. *Appl. Phys. Lett.* **2006,** *88* (12), 123109.

(87) Brady, G. J.; Way, A. J.; Safron, N. S.; Evensen, H. T.; Gopalan, P.; Arnold, M. S. Quasi-ballistic Carbon Nanotube Array Transistors with Current Density Exceeding Si and GaAs. *Science Advances* **2016,** *2* (9).

(88) Qiu, C.; Zhang, Z.; Xiao, M.; Yang, Y.; Zhong, D.; Peng, L. Scaling Carbon Nanotube Complementary Transistors to 5-nm Gate Lengths. *Science* **2017,** *355*, 271-276.

(89) Itkis, M. E.; Borondics, F.; Yu, A.; Haddon, R. C. Bolometric Infrared Photoresponse of Suspended Single-Walled Carbon Nanotube Films. *Science* **2006,** *312*, 413-416.

(90) Moser, M. L.; Li, G.; Chen, M.; Bekyarova, E.; Itkis, M. E.; Haddon, R. C. Fast Electrochromic Device Based on Single-Walled Carbon Nanotube Thin Films. *Nano Lett.* **2016,** *19* (9), 5386–5393.

(91) Bekyarova, E.; Davis, M.; Burch, T.; Itkis, M. E.; Zhao, B.; Sunshine, S.; Haddon, R. C. Chemically Functionalized Single-Walled Carbon Nanotubes for Ammonia Sensors. *J. Phys. Chem. B* **2004,** *108*, 19717-19720.

(92) Kong, J.; Franklin, N. R.; Zhou, C. W.; Chapline, M. G.; Peng, S.; Cho, K. J.; Dai, H. J. Nanotube Molecular Wires as Chemical Sensors. *Science* **2000,** *287* (5453), 622-625.

(93) Cao, Q.; Rogers, J. A. Ultrathin Films of Single-Walled Carbon Nanotubes for Electronics and Sensors: A Review of Fundamental and Applied Aspects. *Adv. Mater.* **2009,** *21* (1), 29-53.

(94) Li, J.; Lu, Y.; Ye, Q.; Cinke, M.; Han, J.; Meyyappan, M. Carbon Nanotube Sensors for Gas and Organic Vapor Detection. *Nano Lett.* **2003,** *3*, 929-933.

(95) Mubeen, S.; Zhang, T.; Chartuprayoon, N.; Rheem, Y.; Mulchandani, A.; Myung, N. V.; Deshusses, M. A. Sensitive Detection of H_2S Using Gold Nanoparticles Decorated Single-Walled Carbon Nanotubes. *Anal. Chem.* **2010,** *82*, 250-257.

(96) Bindl, D. J.; Wu, M. Y.; Prehn, F. C.; Arnold, M. S. Efficiently Harvesting Excitons from Electronic Type-Controlled Semiconducting Carbon Nanotube Films. *Nano Lett.* **2011,** *11*, 455-460.

(97) Arnold, M. S.; Zimmerman, J. D.; Renshaw, C. K.; Xu, X.; Lunt, R. R.; Austin, C. M.; Forrest, S. R. Broad Spectral Response Using Carbon Nanotube/Organic Semiconductor/C60 Photodetectors. *Nano Lett.* **2009,** *9* (9), 3354-3358.

(98) Bindl, D. J.; Safron, N. S.; Arnold, M. S. Dissociating Excitons Photogenerated in Semiconducting Carbon Nanotubes at Polymeric Photovoltaic Heterojunction Interfaces. *ACS Nano* **2010,** *4*, 5657-5664.

(99) Shea, M. J.; Arnold, M. S. 1% Solar Cells Derived from Ultrathin Carbon Nanotube Photoabsorbing Films. *Appl. Phys. Lett.* **2013,** *102*, 243101.

Chapter 2 Giant Raman Response to the Encapsulation of Sulfur in Narrow Diameter Single-Walled Carbon Nanotubes

2.1 Introduction

In the modern society, the development of new improved energy sources became extremely important as it is closely related to the development of society, population, economy, and lifestyles. Currently, the main source of energy is fossil fuel which is causing serious environmental issues.[1] Therefore, much effort has been done to develop renewable and sustainable energy sources, such as wind power, solar energy, and hydropower, to replace the traditional fuel and alleviate the environmental problems. However, all these energy sources are intermittent, and it is important and necessary to develop technologies to store these energies. Rechargeable batteries with superior performance are one of the most promising storage technologies to solve this problem. Up to now, many battery systems have been developed and commercialized, such as lead-acid, nickel-cadmium, nickel metal hydride, and lithium ion battery.[2-4] Among these storage systems, Lithium ion (Li-ion) batteries are viewed as the most promising due to their higher energy density than other systems. In the past decades, many Li-ion systems including $LiMO_2$/Graphite, $LiMO_2$/silicon, and Li/sulfur, have been developed to improve their energy densities, decrease the cost, and increase the cycle life.[5] From the theoretical calculation, the lithium-sulfur (Li/S) system has higher energy density than others and has attracted much more attention (Figure 2.1). [5]

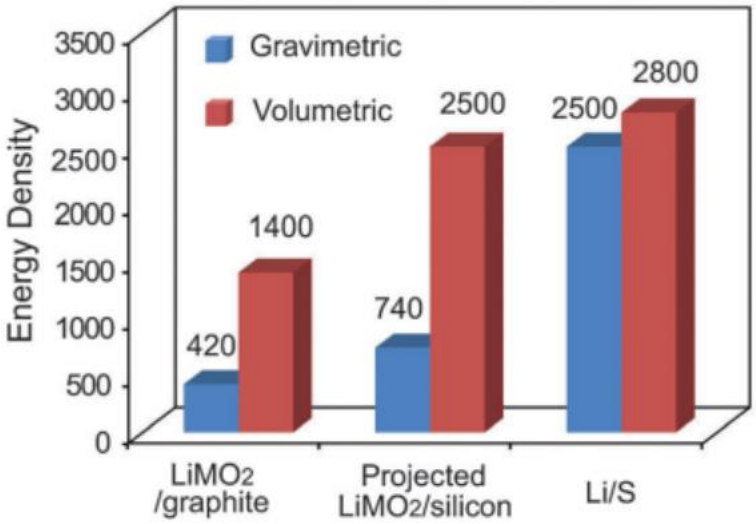

Figure 2.1 The theoretical energy density of different Li-ion batteries based on active materials only.[5]

Sulfur and lithium has the theoretical capacity of 1673 mAh g^{-1} and 3861 mAh g^{-1} respectively. With pairing lithium anode and sulfur cathode the voltage of the cell can reach 2.15 V, resulting in the gravimetric energy density of 2567 Wh Kg^{-1}.[6-7] Moreover, sulfur also has more advantages than other cathode materials such as low cost, natural abundance on Earth, and environmental benignity.

The common Li-S battery is composed of sulfur cathode, metallic lithium anode, organic liquid, and separator (Figure 2.2). [1, 5]

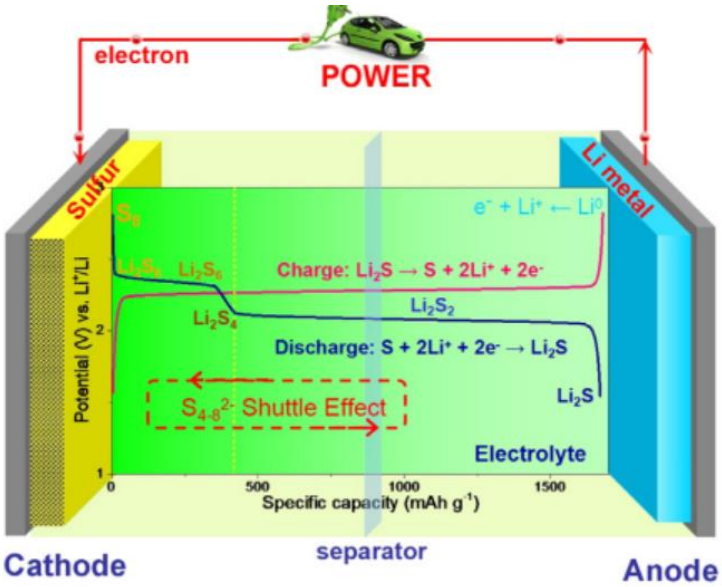

Figure 2.2 Schematic of Li-S battery and the charge and discharge processes.[1]

Even though Li-S battery has been regarded as promising systems when considering the energy density and cost, there are still many challenges to increase its cycle life and energy efficiency. For example, polysulfide species will be produced and dissolved during the discharge process, resulting in the material loss, the increase of impedance, and shuttle effect. Li_2S_2 and Li_2S produced in the discharge process are insoluble in electrolyte and precipitate out at the cathode, which will prevent further lithiation due to their high resistivity. Moreover, sulfur is natural insulator which is another factor limiting its electrochemical utilization.[5, 8-9]

To solve these challenges, novel electrode materials and structures are needed. In the past several years, nanostructured sulfur electrodes were regarded as promising candidates to improve the performance of Li-S batteries. Combining sulfur with other nanomaterial, like carbon nanotubes, can increase the conductivity of the electrode to improve its performance.

Carbon nanotubes are 1D nanomaterials which show unique structure and outstanding physical and electric properties, such as high carrier mobility and current-carrying capacity, unique optoelectronic properties, large surface area, and high electrochemical stability, which has great potential for applications in thin-film transistors (TFTs), novel electronic and optoelectronic devices, logic circuits, solar cell, and lithium-sulfur battery.

The use of carbon-based materials, including single-walled carbon nanotubes (SWNTs) to encapsulate sulfur provides an interesting approach to the study of the electrochemical lithiation process at the cathode in which there is confinement of the active sulfur species.[10-15] Apart from the electrochemical experiments, these materials have been studied by X-ray diffraction, Raman spectroscopy, XPS, TGA and theoretical calculations.[16-17] The results of these studies have been interpreted in terms of metallic, linear one-dimensional chains of sulfur confined within the SWNTs. As far as we could ascertain the previous studies made use of electric arc (EA) produced materials which are known to lead to SWNTs of relatively large diameter ($D_{av} \approx 1.55$ nm),[18-20] and the response of the Raman spectra to the presence of encapsulated sulfur is relatively modest as shown in prior reports and in our own experiments. However when we employed HiPCO-SWNTs in an essentially identical set of sulfur encapsulation experiments we observed an extremely large modulation of the Raman peak intensities.

In the present study we report our studies and interpretation of the effect of sulfur encapsulation on the spectroscopic properties of EA- and HiPCO-SWNTs of average diameter, $D_{av} = 1.55 \pm 0.1$nm and 1.0 ± 0.2nm, respectively.[18-20] In order to

unambiguously characterize the effect of sulfur incorporation on the HiPCO-SWNTs we prepared samples as thin films (thickness, t = 50nm), by filtration of dispersions.[21]

2.2 Experimental Section

1. SWNTs Thin Film Preparation

SWNTs prepared by electric-arc method (EA-SWNTs) and high-pressure of carbon monoxide (HIPCO-SWNTs) are dispersed in sodium cholate solution. In a typical experiment HiPCO-SWNTs (Nanointegris, 2mg), were dispersed in 100ml of an aqueous solution of sodium cholate (1g) by sonication (5 h). The dispersion was centrifuged at 8000 rpm (11000 G) for 15m, and then filtered through a cellulose membrane (pore size 50nm).

2. Preparation of S@SWNTs Thin Film

SWNT films (EA-SWNTs and HIPCO-SWNTs) were transferred to quartz substrates by dissolving cellulose membrane via acetone vapor. S@SWNTs was prepared by Dr. Chengyin Fu from Prof. Juchen Guo's group. The resulting samples were used for spectroscopic characterization. For the removal of sulfur from SWNTs, S@SWNTs thin films were annealed at 650 ^{o}C in flowing argon gas for 10 hours. To clearly interpret the interaction between SWNTs and Sulfur, the isotope ^{34}S were filled into SWNTs via the same process.

3. Raman and UV-Vis Spectra Characterization

All the Raman spectra of SWNTs thin films with or without sulfur on quartz were collected by Thermo Scientific Nicolet Almega XR Dispersive Raman Spectrometer. The

wavelength of the laser used in Raman spectrometer is 532 nm. UV-vis-NIR absorbance spectra were collected by Cary 5000 spectrophotometer.

4. XPS Measurement

The X-ray photoelectron spectroscopy (XPS) was performed using a Kratos AXIS ULTRADLD XPS system equipped with an Al *Kα* monochromated X-ray source. The vacuum pressure was kept below 3×10^{-9} torr and a charge neutralizer was applied during the data acquisition. The survey spectra were recorded using 0.5 eV step size, 100 ms dwell time, and 80 pass energy. The high-resolution spectra were recorded with 0.05 eV step size, 200 ms dwell time, and 20 pass energy. For the measurements, 8 nm thin films were transferred on glass substrates.

2.3 Results and Discussions

Here we first fill sulfur in EA-SWNTs thin film and characterize it by Raman spectroscopy. In agreement with previous work, the response of EA-SWNTs to the encapsulation of sulfur (denoted as S@EA-SWNTs) is quite weak (Figure 2.3).[14-15] There is a discernible effect on the radial breathing mode (*RBM*) which appears at 150-200 $cm^{-1}$and an enhancement of peaks centered at 375 cm^{-1},[15] which may correspond to a peak that was previously observed at 390 cm^{-1} in a similar sample.

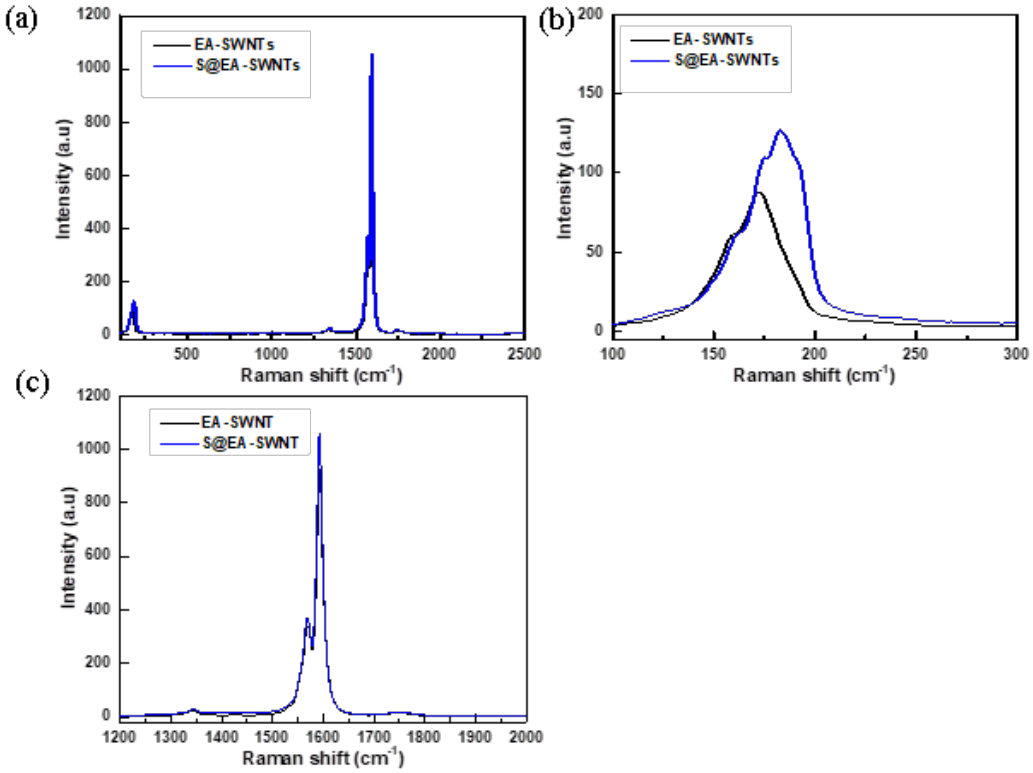

Figure 2.3 Raman spectra of EA-SWNTs and S@EA-SWNTs: (a) full spectrum, (b) *RBM* region, (c) G-peak region (laser excitation wavelength: 532 nm).

The response of the HiPCO-SWNTs to the encapsulation of sulfur is much more pronounced (Figure 2.4a, Figure 2.4b-d), and prominent peaks appear at 319 and 395 cm^{-1} together with a series of peaks at about 715 cm^{-1}.

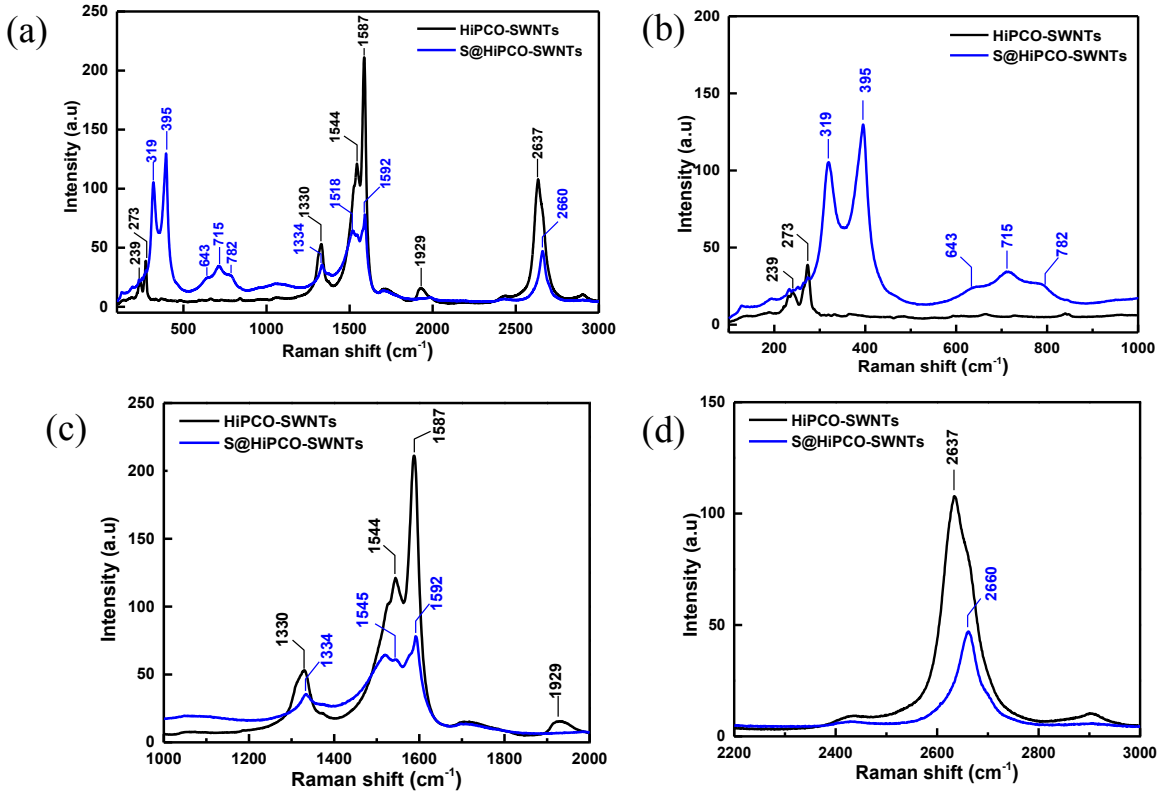

Figure 2.4 (a) Raman spectra of HiPCO-SWNTs and S@HiPCO-SWNTs films at laser excitation wavelength 532 nm. (b) *RBM* and *IFM* region, (c) *G*-peak region, (d) *2D*-peak region (laser excitation wavelength: 532 nm).

We compare the Raman spectroscopy of these new features with the Raman spectroscopy of the Sulfur shown in Figure 2.5. The main Raman features of Sulfur are at 146 cm^{-1}, 211 cm^{-1}, and 466 cm^{-1} which are different to the new features of S@SWNTs (319 cm^{-1}, 395 cm^{-1}, 643 cm^{-1}, 715 cm^{-1}, and 782 cm^{-1}). Therefore, the new Raman features of S@SWNTs are not from the pure sulfur coating on the surface of the SWNTs.

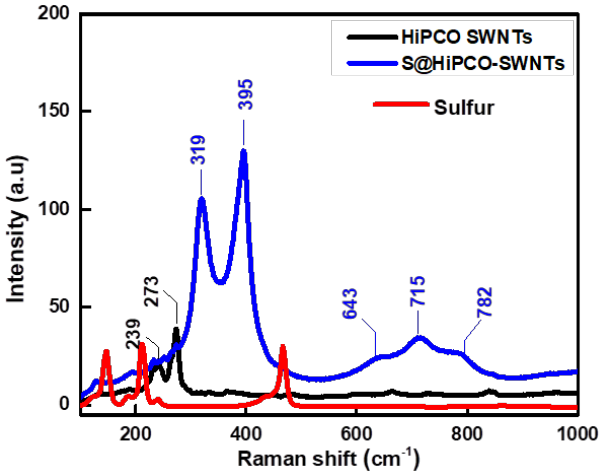

Figure 2.5 Raman spectroscopies of HiPCO SWNTs, S@HiPCO SWNTs, and pure sulfur.

We find that these new features disappear when the SWNTs are annealed at high temperatures (Figure 2.6a) and in the case of HiPCO-SWNTs the sulfur removal process is completed after annealing at 650 ºC for 10 hours under argon; furthermore we do not find any obvious effect on pristine SWNTs that have been annealed at these temperatures (Figure 2.6b).

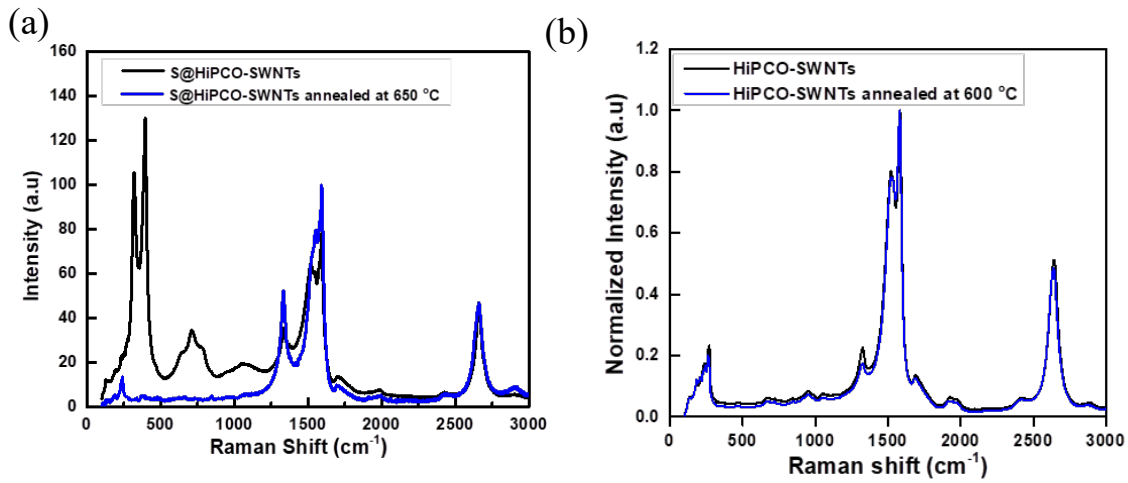

Figure 2.6 (a) Raman spectra of S@HiPCO-SWNTs and S@HiPCO-SWNTs annealed at 650 ^{o}C in Ar atmosphere. (b) Raman spectra of HiPCO-SWNTs and HiPCO-SWNTs annealed at 600 ^{o}C in Ar atmosphere.

The intensities of Raman features are affected by changes in the electronic structure of the carbon nanotubes as well as to perturbations to the restoring forces of the vibrational modes.[22] Thus in order to provide direct information on the effect of sulfur incorporation on the electronic structure of the SWNTs we examined the near-infrared and Visible (NIR/VIS) spectra of the samples and the results are shown in Figure 2.7a. It is quite clear that the features due to the SWNT interband electronic transitions in the S_{11}, S_{22} (semiconducting) and M_{11} (metallic) regions are strongly affected in the S@HiPCO-SWNTs while there is little change in the NIR/VIS spectrum of S@EA-SWNTs (Figure 2.7b).

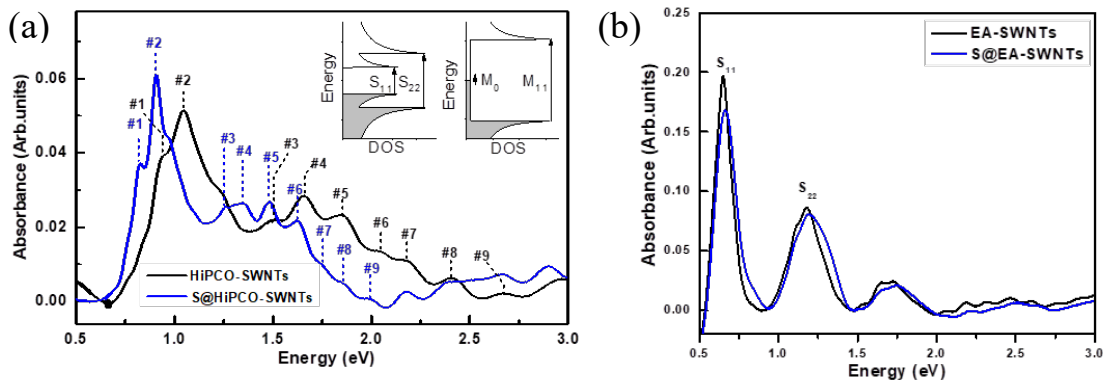

Figure 2.7 (a) Baseline subtracted near NIR/VIS absorption spectra of HiPCO-SWNTs and S@HiPCO-SWNTs films in the vicinity of the S_{11}, S_{22} and M_{11} interband electronic transitions; Inset: Schematic energy band diagram for semiconducting and metallic SWNTs; (b) Baseline subtracted NIR/VIS absorption spectra of EA-SWNTs and S@EA-SWNTs films.

The baseline subtracted NIR/VIS spectra are shown in Figure 2.7a and our best estimates for the assignments are given in Table 2.1 (nomenclature is shown in inset to Figure 2.7a; note that peak 7 can be assigned to the S_{22} or the M_{11} set of transitions). Thus the percentage decrease in the NIR/VIS transitions due to sulfur encapsulation are ΔS_{11} = -13% (1), -13 (2); ΔS_{22} = -16 (3), -18 (4), -20 (5), -20(6), -20 (7); ΔM_{11} = -20 (7), -23 (8), -26 (9).

Table 2.1 Peak assignments for the NIR/VIS spectra of HiPCO-SWNTs and S@HiPCO-SWNTs films.

Peaks		**SWNTs (eV)**	**S@ SWNTs (eV)**	**Shift (eV)**
S_{11}	#1	0.948	0.826	0.122
	#2	1.046	0.907	0.139
S_{22}	#3	1.504	1.260	0.244
	#4	1.650	1.349	0.301
	#5	1.856	1.481	0.375
	#6	2.042	1.625	0.417
M_{11}	#7	2.181	1.750	0.431
	#8	2.404	1.858	0.546
	#9	2.679	1.991	0.688

The assignments are based on previous studies of individual HiPCO-SWNTs using absorption and fluorescence spectroscopy,[23-25] and there is a clear trend toward larger shifts in the interband transitions as the band gap energies increase which is reflected in the percentage decrease in the band gaps among the transitions. There are a number of distinct effects which could be responsible for the shifts in the interband electronic transition energies and we discuss some of the more likely scenarios below.

We begin by emphasizing that the shifts in the band gap energies as result of sulfur encapsulation scale roughly with the energy gaps and thus could be accounted for by an increase in the SWNT diameters or a weakening of the resonance or transfer integral (β), of the C-C bonds as the simple tight binding form of the interband transition energies is

given by: $S_{11}=2\alpha\beta/d$, $S_{22}=4\alpha\beta/d$, and $M_{22}=6\alpha\beta/d$ (where a is the carbon-carbon bond length (nm) and d is the SWNT diameter (nm)).[22] If we scale the percentage decreases in the observed interband transition energies by the ratios of the numerical prefactors from the tight binding calculation, we obtain: ΔS_{11} = -13% (1), -13 (2); $\Delta S_{22}/2$ = -8 (3), -9 (4), -10 (5), -10(6), -10(7); $\Delta M_{11}/3$ = -7 (7), -8 (8), -9 (9). Thus based on the interband electronic transitions, sulfur encapsulation has a large effect on the electronic structure of the SWNTs and if this were to be attributed to a change in geometry it would imply an increase in the SWNT diameters by about 10%, which is not supported by our calculations (Table 2.1).

Given the intimate contact between the sulfur chain and the walls of the HiPCO-SWNTs it is natural to consider the formation of excimers or exciplexes between the two materials,[26] but the nature of the necessary charge transfer complex does not seem very plausible. Rehybridization effects are known to be important in small diameter SWNTs and probably play a role in the phenomena reported herein.[18, 27-28] An important manifestation of this effect is polygonization[29] in which the walls of the SWNTs undergo the type of faceting which is well known in fullerenes.[30] Polygonization of the SWNT walls is inevitable given the fourfold axial profile of the S_x chain found in our calculations which was done by M. Belén Oviedo from Prof. Bryan M. Wong group. As in the fullerenes, this distortion serves to concentrate the pyramidalization at certain carbon atoms that become strongly rehybridized.[30-31]

There have been a number of studies of the effect of strain and external pressure on SWNTs that throw light on the origins of the shifts that we observe (Figure 2.7a). Matrix-

imposed stress on SWNTs has been shown to produce a chirality-dependent shift of the photoluminescence spectra that divides the samples into two groups depending on their helicity: the first group of SWNTs shows an increase in the energy of the S_{11} transitions and a decrease in the S_{22} energies on cooling frozen dispersions, whereas the second group of SWNTs shows exactly the opposite behavior.[32] These results are in full accord with calculations of the effect of stress along the axis of the SWNTs,[33-34] and thus it appears that the frozen matrix generates uniaxial compressive stress along the SWNTs.

A study of the effect of hydrostatic pressure on the interband transition energies of debundled HiPCO-SWNT suspensions in diamond anvil cells found that the band gap energies moved to lower energies, although the second set of interband transitions (S_{22} in this paper), were much less sensitive to pressure.[28] The authors were unable to fully rationalize these results in terms of previous studies although they noted the likely importance of the rehybridization of the SWNT electronic structure. Our results are not consistent with either of these previous reports on strain as we find that all of the electronic transitions move to lower energies with the greatest shifts associated with the higher excitation levels.

The spectral intensity of the Raman features of SWNT samples is strongly enhanced when the experimental laser light is resonant with an interband (excitonic) transition in individual carbon nanotubes.[22, 35] As a result, variations in the Raman intensity are usually ascribed to a change in the resonance condition and there are a number of reports in the literature on the observation of such effects in doped samples.[36-41] In virtually all these cases the Raman intensities are reduced; the only mention we could find of strongly

increased intensities in Raman spectra was a report on individual, pristine, suspended quasi-metallic SWNTs in which it was found that all of the transitions are strongly modulated by electrostatic gating due to the proximity of a Mott insulator transition.[42]

The resonant Raman intensity in the Stokes process is given by

$$I^{\mu}(E_L) = C\left|\int \frac{M^{oa}M^{ep}M^{oe}dk}{E_R[E_R - E_{ph}]}\right|^2 \qquad (2.6)$$

where C is a constant, $E_R = E_L - E_\mu - i\gamma$ is the resonance condition, E_L is the laser energy (2.41 eV), E_μ is the exciton transition energy for the μth set of subbands, E_{ph} is the phonon energy, γ is the resonance broadening energy, M^{oa} is the matrix element for the optical absorption process, M^{ep} is the electron-phonon coupling matrix element, and M^{oe} is the matrix element for the optical emission process.[42-46]

As noted above a likely cause of the drastic modification to the Raman spectra of HiPCO-SWNTs on sulfur encapsulation is a change in the resonance condition (E_R), and this scenario is supported by both the NIR/VIS spectroscopy and the DFT calculations carried out by Prof. Wong group on the S@HiPCO-SWNTs (below). The resonance term includes both the interband transition energy (E_μ) and the resonance broadening energy (γ) and it is clear from Figure 2.7a that both of these quantities are affected by the incorporation of sulfur into HiPCO-SWNTs. The resonance broadening energy is very small in individual SWNTs (γ = 8 meV for a SWNT on Si/SiO_2)[44] but this term is quite sensitive to the nanotube environment and values of γ = 60 meV (SDS wrapped SWNTs) and γ = 120 meV (SWNT bundles) have been reported for HiPCO-SWNTs.[45] Thus it is to be expected that the incorporation of the S_x-helix would further increase the value of γ in

the S@HiPCO-SWNTs. As discussed above, the strain induced by the incorporation of sulfur into the HiPCO-SWNTs affects the interband transition energies [E_μ (S_{11}, S_{22} and M_{11}, above)] and may also be expected to modify the electron-phonon coupling term (M^{ep}).

Most of the HiPCO-SWNT Raman intensities are decreased by the incorporation of sulfur in agreement with previous work on perturbed SWNTs,[36, 39-40, 46] and it is only in the region from 300-800 cm^{-1} that new, very strong peaks appear; given the proximity of this region to sulfur-sulfur vibrations in the Raman spectra of the various molecular and polymeric sulfur species it is natural to consider electron-phonon coupling between the excited states of the SWNTs and the phonons of the sulfur species that are encapsulated. In this way molecular vibrations of the sulfur species could be enhanced in the Raman spectra by the excitonic absorptions of the SWNTs and we note that the band at 715 cm^{-1} observed in the S@HiPCO-SWNTs is quite close to the value of 716 cm^{-1} observed for S_2 ($^3\Sigma_g^-$) in an argon matrix.[47] Polymeric sulfur (S_x) has bands at ~460 and ~425 cm^{-1} [48] which do not correspond to the bands at 395 and 319 cm^{-1} observed in our spectra, although the distortions of the sulfur chains discussed below would likely weaken the stretching frequencies of the vibrations of the S_x@HiPCO-SWNTs and thus these features could possibly originate from encapsulated sulfur species. Therefore we carried out encapsulation experiments in which $^{34}S_8$ was used as the source for infusion of sulfur into the HiPCO-SWNTs. Based on prior work in the literature the isotopic shift in such species is known to closely follow the simple spring constant relationship which gives $\nu_1(^{34}S)/\nu_1(^{32}S) = (32/34)^{1/2} = 0.970$ (Figure 2.8a).[48] As we show in Figure 2.8b, the new

peaks in the Raman spectra of S@HiPCO-SWNTs exhibit the expected shift for isotopic substitution in species possessing S-S bonds and this shows unequivocally that the new Raman vibrations originate from encapsulated sulfur species which obtain intensity from electron-phonon coupling to the resonant SWNT excited states.

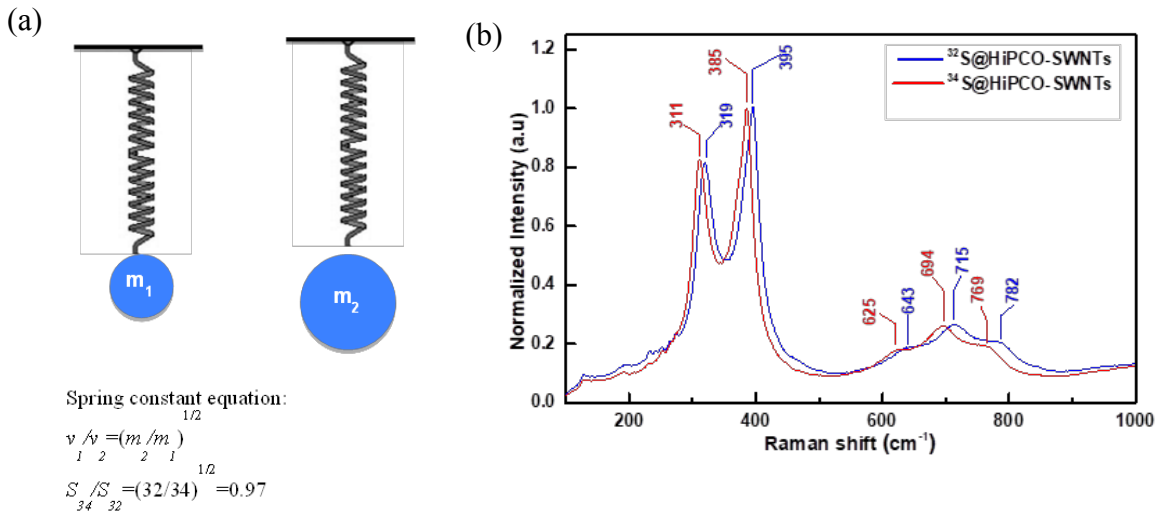

Figure 2.8 (a) The mechanism of spring constant equation; (b) Raman spectra of ^{32}S@HiPCO-SWNTs and ^{34}S@HiPCO-SWNTs films.

Dr. M. Belén Oviedo from Professor Wong research group carried out DFT calculations on the S@SWNTs, and it is clear that there is ample space inside the EA-SWNTs to accommodate sulfur in the form of S_8 molecules or in polymeric form but this is not the case for the HiPCO-SWNTs which have a much smaller diameter. The most compact form for sulfur encapsulated in SWNTs was found to be a helix with a screw order of four atoms as shown in Figure 2.9.

Figure 2.9 Calculated structure for the sulfur helix in S@SWNTs: (a) side-view, (b) cross-sectional view. (Calculation was done by Dr. M. Belén Oviedo from Professor Wong group)

When this structure was encapsulated in an (11,11) EA-SWNT of diameter 1.6 nm the preferred diameter of the helix was found to be about 0.33 nm which gives a van der Waals diameter of about 0.7 nm. This is easily accommodated in the (11,11) SWNT which has an internal van der Waals diameter of 1.26 nm but for HiPCO-SWNTs the corresponding typical chirality might be that of a (7,7) SWNT which has a calculated diameter of 0.95 nm and internal van der Waals diameter of ~0.61 nm. Thus we anticipate a non-bonded interaction between the sidewalls of HiPCO-SWNTs that is not present in EA-SWNTs, and it may be seen that the preferred helical S_x structure is expected to break the quasi-rotational symmetry of the HiPCO-SWNTs by imposing a fourfold distortion of the sidewalls.

DFT optimizations of HiPCO SWNT (7,7) is shown in Figure 2.10, the diameter of SWNT is 0.993 nm. The sulfur chain inside of SWNT tends to accommodate conformations that resemble the cylo-S8 allotrope which is similar to the cyclo-S8 allotrope geometry, which is recognized as the most thermodynamically stable form at ambient temperature.[49]

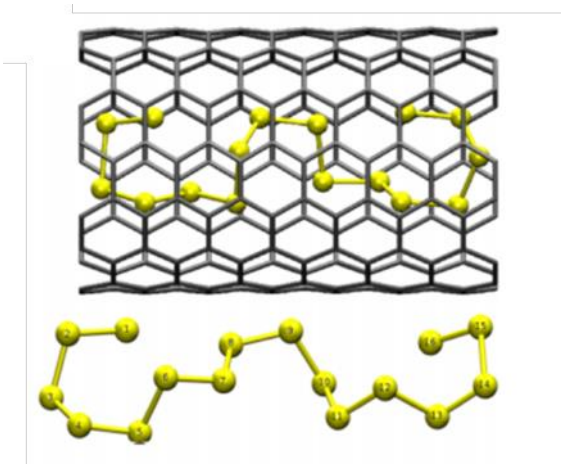

Figure 2.10 Optimized geometry of a sulfur chain inside a (7,7) SWNT (top) and view of the sulfur chain without (7,7) SWNT (bottom).[49] (Calculation was done by Dr. M. Belén Oviedo from Professor Wong research group).

The encapsulation experiments are run at 600°C in a static vacuum and we note that thermodynamic analysis indicates that S_2 comprises about 5% of the vapor above sulfur at 500°C under a total pressure of 0.2 MPa, and thus it will be possible to rapidly fill the SWNTs with S_2.[50-52] In the suggested mechanism of encapsulation the S_2 molecules enter the SWNTs and polymerize to diradicals particularly after cooling to room temperature. High level calculations confirm conducted by Prof. Wong research group indicate that cis- and trans-isomers of S_4 are considerably more stable than 2 S_2 ($^3\Sigma_g^-$),[53] and so the dimerization and subsequent polymerization reactions should occur spontaneously under the reaction conditions.

XPS measurements show 8 atomic percent internal sulfur after encapsulation experiments on HiPCO-SWNTs, which is reduced to 2% after treatment at 450^{0}C (Figure 2.11). The survey spectrum of S@HiPCO SWNTs clearly showed the presence of sulfur,

whereas no sulfur peaks were detected in the survey spectra of S@HiPCO SWNTs annealed at 450 ºC in vacuum. Both spectra show a strong *C1s* peak, and the additional peaks - *O1s*, *Si2s*, and *Si2p* - are assigned to the glass substrate; XPS spectra of powdered materials (not shown) showed traces of oxygen content. The high resolution *C1s* spectra of S@HiPCO SWNTs and S@HiPCO SWNTs annealed at 450 ºC (Figure 2.11c), show that the SWNTs are largely preserved after the annealing process, while the S2p spectra (Figure 2.11d) illustrates that after annealing the sulfur content is significantly reduced.

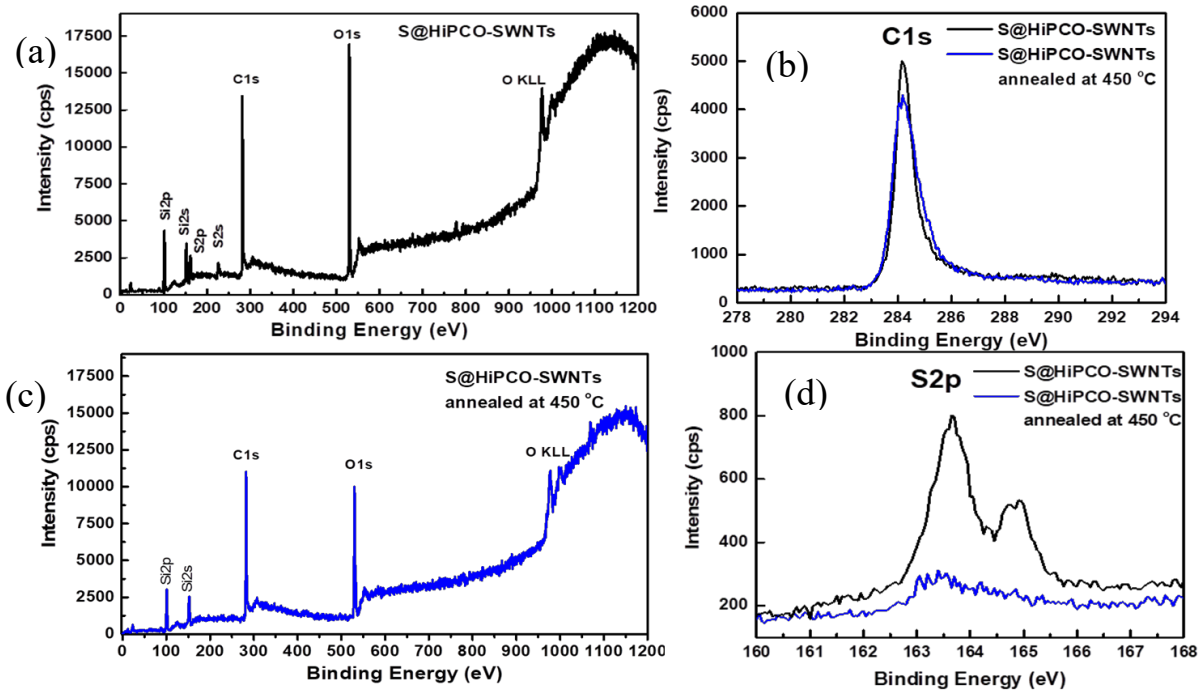

Figure 2.11 (a) Survey spectrum of S@HiPCO SWNTs. (b) Survey spectrum of S@HiPCO-SWNT annealed at 450 ºC in vacuum. (c) *C1s* spectra of S@HiPCO SWNTs and S@HiPCO SWNTs annealed at 450 ºC in vacuum. (d) *S2p* spectra of S@HiPCO SWNTs and S@HiPCO SWNTs annealed at 450 ºC in vacuum.

2.4 Conclusions

In summary, we discovered that the encapsulation of sulfur in HiPCO-SWNTs leads to large changes in the Raman spectra with dramatic enhancements to peaks in the vicinity of the *RBM* and *IFM* regions (319, 395 and 710 cm^{-1}), while the high frequency bands ($\nu >$ 1200 cm^{-1}) are decreased in intensity. The encapsulated species also shifts the near-IR interband electronic transitions to lower energy by more than 10%. These effects seem to originate with the van der Waals interaction of the confined sulfur species with the walls of the SWNTs which are not expected to be significant in the case of the previously studied large diameter SWNTs. We suggest that sulfur in the small diameter SWNTs exists as a helical polymeric sulfur chain.

References

(1) Wang, J.; Xie, K.; Wei, B. Advanced Engineering of Nanostructured Carbons for Lithium-Sulfur Batteries. *Nano Energy* **2015,** *15*, 413-444.

(2) Manthiram, A.; Fu, Y.; Chung, S. H.; Zu, C.; Su, Y. S. Rechargeable Lithium-Sulfur Batteries. *Chem. Rev.* **2014,** *114*, 11751-11787.

(3) Manthiram, A. Materials Challenges and Opportunities of Lithium Ion Batteries. *J. Phys. Chem. Lett.* **2011,** *2*, 176-184.

(4) Goodenough, J. B.; Kim, Y. Challenges for Rechargeable Li Batteries. *Chem. Mater.* **2010,** *22*, 587-603.

(5) Yang, Y.; Zheng, G.; Cui, Y. Nanostructured Sulfur Cathodes. *Chem. Soc. Rev.* **2013,** *42*, 3018-3032.

(6) Ji, X. L.; Nazar, L. F. Advances in Li-S Batteries. *J. Mater. Chem.* **2010,** *20*, 9821-9826.

(7) Mikhaylik, Y. V.; Akridge, J. R. Polysulfide Shuttle Study in the Li/S Battery System. *J. Electrochem. Soc. 151*, A1969-A1976.

(8) Kumaresan, K.; Mikhaylik, Y.; White, R. E. A Mathematical Model for a Lithium-Sulfur Cell. *J. Electroanal. Soc.* **2008,** *155*, A576-A582.

(9) Yamin, H.; Pelde, E. Electrochemistry of a Nonaqueous Lithium/Sulfur Cell. *J. Power Sources* **1983,** *9*, 281-287.

(10) Guo, J.; Xu, Y.; Wang, C. Sulfur Impregnated Disordered Carbon Nanotubes Cathode for Lithium-Sulfur Batteries. *Nano Lett.* **2011,** *11*, 4288-4294.

(11) Zheng, G.; Yang, Y.; Cha, J. J.; Hong, S. S.; Cui, Y. Hollow Carbon Nanofiber-Encapsulated Sulfur Cathodes for High Specific Capacity Rechargeable Lithium Batteries. *Nano Lett.* **2011,** *11*, 4462 - 4467.

(12) Dörfler, S.; Hagen, Y. A., H; Tübke, J.; Kaskel, S.; Hoffmann, M. J. High capacity vertical aligned carbon nanotube/sulfur composite cathodes for lithium-sulfur batteries. *Chem. Commun.* **2012,** *48*, 4097-4099.

(13) Zhou, G.; Wang, D.; Li, F.; Hou, P.; Yin, L.; Liu, C.; Lu, G.; Gentle, I. R.; Cheng, H. A flexible nanostructured sulphur–carbon nanotube cathode with high rate performance for Li-S batteries. *Energy Environ. Sci.* **2012,** *5*, 8901-8906.

(14) Fujimori, T.; Morelos-Go´mez, A.; Zhu, Z.; Muramatsu, H.; Futamura, R.; Urita, K.; Terrones, M.; Hayashi, T.; Endo, M.; Hong, S. Y.; Choi, Y. C.; Tomanek, D.; Kaneko, K. Conducting linear chains of sulphur inside carbon nanotubes. *Nature Comm.* **2013,** *4*, 3162.

(15) Yang, C.; Yin, Y.; Guo, Y.; Wan, L. Electrochemical (De)Lithiation of 1D Sulfur Chains in Li−S Batteries: A Model System Study. *J. Am. Chem. Soc.* **2015,** *137* 2215–2218.

(16) Loiseau, A.; Pascard, H. Synthesis of Long Carbon Nanotubes Filled with Se, S, Sb, and Ge by the Arc Method. *Chem. Phys. Lett.* **1996,** *256*, 246-252.

(17) Demoncy, N.; Stephan, O.; Brun, N.; Colliex, C.; Loiseau, A.; Pascard, H. Sulfur: The Key for Filling Carbon Nanotubes with Metals. *Syn. Metals* **1999,** *103*, 2380-2383.

(18) Hamon, M. A.; Itkis, M. E.; Niyogi, S.; Alvaraez, T.; Kuper, C.; Menon, M.; Haddon, R. C. Effect of Rehybridization on the Electronic Structure of Single-Walled Carbon Nanotubes. *J. Am. Chem. Soc.* **2001,** *123*, 11292-11293.

(19) Wang, F.; Itkis, M. E.; Haddon, R. C. Enhanced Electromodulation of Infrared Transmittance in Semitransparent Films of Large Diameter Semiconducting Single-Walled Carbon Nanotubes. *Nano Lett.* **2010,** *10*, 937-942.

(20) Wang, F.; Itkis, M. E.; Bekyarova, E.; Haddon, R. C. Charge-Compensated, Semiconducting Single-Walled Carbon Nanotube Thin Film as an Electrically Configurable Optical Medium. *Nat. Photonics* **2013,** *7*, 459-465.

(21) Tian, X.; Moser, M. L.; Pekker, A.; Sarkar, S.; Ramirez, J.; Bekyarova, E.; Itkis, M. E.; Haddon, R. C. Effect of Atomic Interconnects on Percolation in Single-Walled Carbon Nanotube Thin Film Networks. *Nano Lett.* **2014,** *14*, 3930-3937.

(22) Dresselhaus, M. S.; Dresselhaus, G.; Eklund, P. C. *Science of Fullerenes and Carbon Nanotubes*, Academic: San Diego, 1996.

(23) Bachilo, S. M.; Strano, M. S.; Kittrell, C.; Hauge, R. H.; Smalley, R. E.; Weisman, R. B. Structure-Assigned Optical Spectra of Single-Walled Carbon Nanotubes. *Science* **2002,** *298*, 2361-2366.

(24) O'Connell, M. J.; Bachilo, S. M.; Huffman, C. B.; Moore, V. C.; Strano, M. S.; Haroz, E. H.; Rialon, K. L.; Boul, P. J.; Noon, W. H.; Kittrell, C.; Ma, J.; Hauge, R. H.; Weisman, R. B.; Smalley, R. E. Band Gap Fluorescence from Individual Single-Walled Carbon Nanotubes. *Science* **2002,** *297*, 593-596.

(25) Ostojic, G. N.; Zaric, S.; Kono, J.; Strano, M. S.; Moore, V. C.; Hauge, R. H.; Smalley, R. E. Interband Recombination Dynamics in Resonantly Excited Single-Walled Carbon Nanotubes. *Phys. Rev. Lett.* **2004,** *92*, 117402.

(26) Klan, P.; Wirz, J. *Photochemistry of Organic Compounds: From Concepts to Practice*, Wiley: Chichester, UK, 2009.

(27) Blase, X.; Benedict, L. X.; Shirley, E. L.; Louie, S. G. Hybridization Effects and Metallicity in Small Radius Carbon Nanotubes. *Phys. Rev. Lett.* **1994,** *72* (12), 1878-1881.

(28) Wu, J.; Walukiewicz; Shan, W.; Bourret-Courchesne, E.; Ager III, J. W.; Yu, K. M.; Haller, E. E.; Kissell, K.; Bachilo, S. M.; Weisman, R. B.; Smalley, R. E. Structure-Dependent Hydrostatic Deformation Potentials of Individual Single-Walled Carbon Nanotubes. *Phys. Rev. Lett.* **2004,** *93*, 017404.

(29) Charlier, J.-C.; Lambin, P.; Ebbesen, T. W. Electronic Properties of Carbon Nanotubes with Polygonized Cross Sections. *Phys. Rev. B.* **1996,** *54*, R8377-R8380.

(30) Haddon, R. C.; Scuseria, G. E.; Smalley, R. E. C240 - The Most Chemically Inert Fullerene? *Chem. Phys. Lett.* **1997,** *272*, 38-42.

(31) Haddon, R. C. Chemistry of the Fullerenes: The Manifestation of Strain in a Class of Continuous Aromatic Molecules. *Science* **1993,** *261*, 1545-1550.

(32) Arnold, K.; Lebedkin, S.; Kiowski, O.; Hennrich, F.; Kappes, M. M. Matrix-Imposed Stress-Induced Shifts in the Photoluminescence of Single-Walled Carbon Nanotubes at Low Temperatures. *Nano Lett.* **2004,** *4*, 2349-2354.

(33) Yang, L.; Anantram, M. P.; Han, J.; Lu, J. P. Band Gap Change of Carbon Nanotubes: Effect of Small Uniaxial and Torsional Strain. *Phys. Rev. B.* **1999,** *60*, 13874-13878.

(34) Yang, L.; Han, J. Electronic Structure of Deformed Carbon Nanotubes. *Phys. Rev. Lett.* **2000,** *85*, 154-157.

(35) Rao, A. M.; Richter, E.; Bandow, S.; Chase, B.; Eklund, P. C.; Williams, K. A.; Fang, S.; Subbaswamy, K. R.; Menon, M.; Thess, A.; Smalley, R. E.; Dresselhaus, G.; Dresselhaus, M. Diameter-Selective Raman Scattering from Vibrational Modes in Carbon Nanotubes. *Science* **1997,** *275*, 187-191.

(36) Kavan, L.; Rapta, P.; Dunsch, L.; Bronikowski, M. J.; Willis, P.; Smalley, R. E. Electrochemical Tuning of Electronic Structure of Single-Walled Carbon Nanotubes: In-Situ Raman and Vis-NIR Studies. *J. Phys. Chem. B* **2001,** *105*, 10764-10771.

(37) Rao, A. M.; Chen, J.; Richter, E.; Eklund, P. C.; Haddon, R. C.; Venkateswaran, U. D.; Kwon, Y.-K.; Tomanek, D. Effect of van der Waals Interactions on the Raman Modes in Single Walled Carbon Nanotubes. *Phys. Rev. Lett.* **2001,** *86*, 3895-3898.

(38) Corio, P.; Santos, P. S.; Brar, V. W.; Samsonidze, G. G.; Chou, S. G.; Dresselhaus, M. S. Potential dependent surface Raman spectroscopy of single wall carbon nanotube films on platinum electrodes. *Chem. Phys. Lett.* **2003,** *370*, 675-682.

(39) Cronin, S. B.; Barnett, R.; Tinkham, M.; Chou, S. G.; Rabin, O.; Dresselhaus, M. S.; Swan, A. K.; Ünlü, M. S.; Goldberg, B. B. Electrochemical gating of individual single-wall carbon nanotubes observed by electron transport measurements and resonant Raman spectroscopy. *App. Phys. Lett.* **2004,** *84*, 2052-2054.

(40) Rafailov, P. M.; Maultzsch, J.; Thomsen, C.; Kataura, H. Electrochemical switching of the Peierls-like transition in metallic single-walled carbon nanotubes. *Phys. Rev. B* **2005,** *72*, 045411.

(41) Das, A.; Sood, A. K.; Govindaraj, A.; Saitta, A. M.; Lazzeri, M.; Mauri, F.; Rao, C. R. Doping in carbon nanotubes probed by Raman and transport measurements. *Phys. Rev. Lett.* **2007,** *99*, 136803.

(42) Bushmaker, A. W.; Deshpande, V. V.; Hsieh, S.; Bockrath, M.; Cronin, S. B. Large Modulation in the Intensity of Raman-Scattered Light from Pristine Carbon Nanotubes. *Phys. Rev. Lett.* **2009,** *103*, 067401.

(43) Saito, R.; Dresselhaus, G.; Dresselhaus, M. S. *Physical Properties of Carbon Nanotubes*, Imperial College Press: Singapore, 1998.

(44) Jorio, A.; Souza Filho, A. G.; Dresselhaus, G.; Dresselhaus, M. S.; Saito, R.; Hafner, J. H.; Lieber, C. M.; Matinaga, F. M.; Dantas, M. S. S.; Pimenta, M. A. Joint Density of Electronic States for One Isolated Single-Wall Carbon Nanotube Studied by Resonant Raman Scattering. *Phys. Rev. B* **2001,** *63*, 245416.

(45) Fantini, C.; Jorio, A.; Souza, M.; Strano, M. S.; Dresselhaus, M. S.; Pimenta, M. A. Optical Transition Energies for Carbon Nanotubes from Resonant Raman Spectroscopy: Environment and Temperature Effects. *Phys. Rev. Lett.* **2004,** *93*, 147406.

(46) Saito, R.; Hofmann, M.; Dresselhaus, G.; Jorio, A.; Dresselhaus, M. S. Raman Spectroscopy of Graphene and Carbon Nanotubes. *Adv. Phys.* **2011,** *60*, 413-550.

(47) Barletta, R. E.; Claassen, H. H.; McBeth, R. L. Raman Spectrum of S2. *J. Chem. Phys.* **1971,** *55*, 5409-5410.

(48) Eckert, B.; Steudel, R. Molecular Spectra of Sulfur Molecules and Solid Sulfur Allotropes. *Top. Curr. Chem* **2003,** *231*, 31-98.

(49) Fu, C.; Oviedo, M. B.; Zhu, Y.; Cresce, A. v. W.; Xu, K.; Li, G.; Itkis, M. E.; Haddon, R.; Chi, M.; Han, Y.; Wong, B. M.; Guo, J. Confined Lithium–Sulfur Reactions in Narrow-Diameter Carbon Nanotubes Reveal Enhanced Electrochemical Reactivity. *ACS Nano* **2018,** *12*, 9775-9784.

(50) Rau, h.; Kutty, T. R. N.; Guedes De Carvalho, J. R. F. High Temperature Saturated Vapour Pressure of Sulphur and the Estimation of Its Critical Quantities. *J. Chem. Thermo.* **1973,** *5*, 291 - 302.

(51) Rau, H.; Kutty, T. R. N.; Guedes De Carvalho, J. R. F. Thermodynamics of Sulphur Vapour. *J. Chem. Thermo.* **1973,** *5*, 833 - 844.

(52) Steudel, R.; Steudel, Y.; Wong, M. W. Speciation and Thermodynamics of Sulfur Vapor. *Top. Curr. Chem.* **2003,** *230*, 117 - 134.

(53) Wong, M. W.; Steudel, R. Structure and Spectra of Tetrasulfur S4 – an Ab Initio MO Study. *Chem. Phys. Lett.* **2003,** *379*, 162 - 169.

Chapter 3 Visible-Blind UV Photodetector Based on Single-Walled Carbon Nanotube Thin Film/ZnO Vertical Hereostructures

3.1 Introduction

Ultraviolet (UV) light is an electromagnetic radiation with the wavelength ranging from 10 nm to 400 nm, which is between X-rays and visible light. There is about 10 % UV light in sunlight and excess of UV exposure can affect human health (Figure 3.1). UV spectral range from 10 nm to 400 nm can be subdivided into a few sub-ranges such as Ultraviolet A (315 nm$\leq\lambda\leq$400 nm), Ultraviolet B (280 nm$\leq\lambda\leq$315 nm), Ultraviolet C (100 nm$\leq\lambda\leq$280 nm), middle Ultraviolet (200 nm$\leq\lambda\leq$300 nm), and vacuum Ultraviolet (10 nm$\leq\lambda\leq$200 nm).[1] As UV light has short wavelength and high photon energy, it can cause ionizing radiation, chemical reactions, and be beneficial or harmful to human health. Up to now, UV light with different wavelengths have been widely used in various applications like photolithography in semiconductor industry, water treatment, air disinfection, polymer degradation, military and space communication. Little UV light exposure can be beneficial to human health by producing vitamin D and leading to the creation of serotonin in our body. However, excessive exposure to UV light for long time will cause harmful effects on human health, especially on eyes, skin, and immune system. All the UV light is invisible to the humans, so it is difficult to avoid the undesired UV light and estimate its intensity. Moreover, the UV light only accounts for less than 10% of sunlight, while visible radiations have higher intensity which complicates UV

detection. Therefore, it is necessary to develop visible-blind UV photodetector for UV light detection.

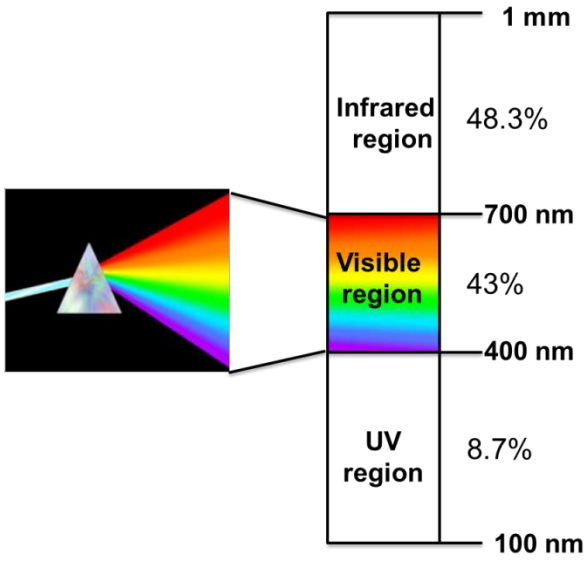

Figure 3.1 The composition of solar irradiation.

UV photodetectors have attracted a great deal of interest in recent years due to their widespread applications such as biological and chemical sensors, missile plume detection, space-to space communication, fire alarm, and solar UV monitoring (Figure 3.2).[2-3] For example, the aircraft is equipped with a suite of self-protection system, which includes UV photodetection system. As most of the UV light from solar irradiation is absorbed by ozone, the UV radiation background at the Earth surface is much less than the infrared light. Therefore, the false-alarm level is quite low.[3]

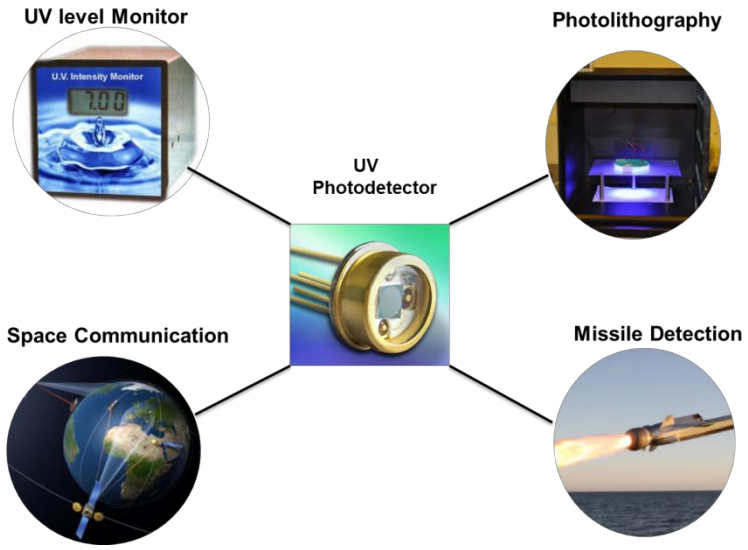

Figure 3.2 Applications of UV photodetectors.

One of the most promising material for UV detector applications is ZnO. ZnO is an II–VI compound semiconductor which crystal structure is based on sp^3 hybridized covalent bonding. As shown in Figure 3.3 the conduction-band minimum (CBM) is formed of Zn^{2+} 4*s* orbitals, while the valence-band (VBM) of the O^{2-} 2*p* orbitals.[4] As a result, the bonding sp^3 states form the valence band, while the corresponding antibonding counterpart forms the conduction band.

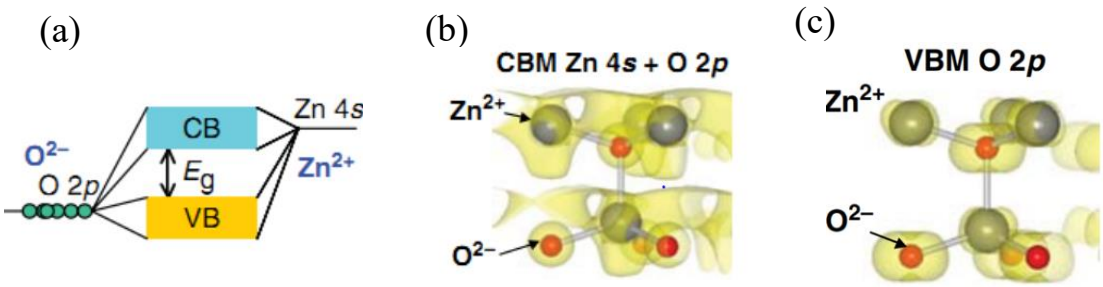

Figure 3.3 Schematic band structures of ZnO; (b) conduction-band minimum (CBM); (c) valence-band maximum (VBM).[4]

Generally, there are two types of crystal structure of ZnO which are cubic zincblende and hexagonal wurtzite. ZnO naturally crystalizes in hexagonal wurtzite structure in ambient due to its high bond polarity which is as high as 3.5.[5] In the wurtzite structure of ZnO, each Zn^{2+} is surrounded by four oxygen ions as shown in Figure 3.4, in which the lattice constants in ZnO are a=b=0.3249 nm with an angle of 120°, and c=0.52042 nm.[6]

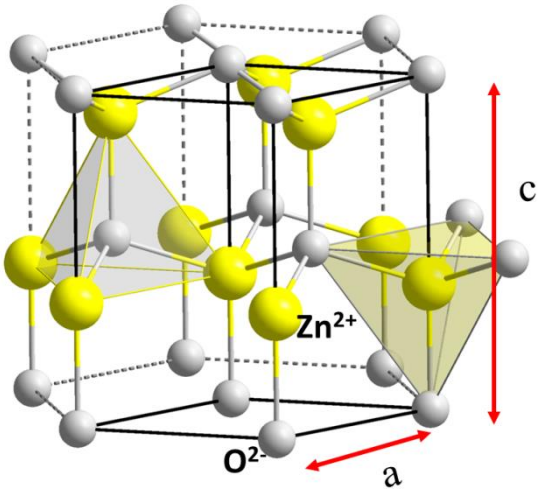

Figure 3.4 The wurtzite structure model of ZnO.[6]

ZnO is a natural n-type semiconductor due to the intrinsic donor type defects such as oxygen vacancies (V_o) and zinc interstitials (Zn_i) produced during the growth process.[7] Compared with the other wide bandgap semiconductor GaN, ZnO has many advantages like availability of large single crystals for homo epitaxy, less cost, biocompatibility, and large exciton binding energy (60 mV vs 25 mV for GaN). Therefore, many techniques have been developed to grow high-quality ZnO thin film or nanostructures, including chemical vapor deposition (CVD), [8] molecular beam epitaxy (MBE),[9-10] solution phase synthesis,[11] and physical vapor deposition (PVD) method.[12] Due to its outstanding electric and optical properties, ZnO has much potential applications in many fields like photodetectors, lasers, gas sensors, light-emitting diodes, and photocatalyst.[13-20]

ZnO is a wide bandgap semiconductor with a direct bandgap of 3.37 eV matching the spectral range desired for solid state UV photodetectors.[21-24] Schottky barrier types of ZnO photodetectors have some advantages over bulk ZnO photoconductors due to built-in electric field efficiently separating photoexcited electron-hole pairs before they recombine, and the performance of such devices has been improved by introducing interdigitated electrode configuration.[24-28] P-N homojunction photodiodes are also utilized to generate built-in electric field, but in the case of ZnO this option is limited as a reliable growth technique of p-type ZnO is still under development.[9, 23, 29-31]

The closest alternative to ZnO p-n junction photodetector is a heterojunction device in which n-type ZnO is combined with p-type conventional semiconductor, typically of smaller bandgap, such as Si, Ge or GaAs.[32-35] Such heterojunction was shown to provide high built-in electric field sufficient for separation of photogenerated electrons and holes

and satisfactory photodetector performance, but additional interface layer was needed to preclude unwanted visible spectral range sensitivity.[35] In addition to bulk ZnO layers, nanostructured forms of ZnO such as nanoparticles and nanowires have been explored,[11, 36-45] showing improved performance in terms of higher UV responsivity,[11, 38, 41, 43, 45-46] and in some cases, faster response time.[11, 38-42, 44, 46-47]

Despite these recent advances, inorganic wide bandgap semiconductor based UV photodetectors with visible blindness and fast response times still dominate commercial market. Nevertheless, these photodetectors have relatively low responsivity of ~0.1 A/W. Thus, it is necessary to develop optimized device structures by the integration of a variety of new nanostructured materials for the all-around competitiveness in the performance and manufacturability in the UV photodetectors market.

Single-walled carbon nanotubes (SWNTs) possess unique combination of electrical and optical properties originated from their one-dimensional structure, such as being metallic (MT) or semiconducting (SC) depending on their diameter and chirality.[48] Thin films of SWNTs can be prepared by a variety of techniques utilizing scalable and manufacturing friendly solution based processes, which are cost effective because of microgram quantities of SWNTs needed for large area applications,[49-51] and with the choice of being made selectively of MT- or SC- SWNTs[52] provide a platform for development of a wide range of electronic and photonic applications, for example, as large area transparent conducting electrodes for touch screen displays, solar cells, light emitting diodes, and smart windows.[50-51, 53-56]

The bandgap of typical SC-SWNTs falls in the range 0.6-1.2 eV matching the bandgaps of conventional semiconductors such as Ge, Si or GaAs. Patterning of SWNT thin films utilizing conventional lithography in combination with chemical and electrostatic doping of p- and n-types allowed to demonstrate all-SWNT thin film based logical integrated circuits,[57-58] infrared photodetectors and electrochromic devices with different functions performed by MT- and SC-SWNTs counterparts.[59-64] The combination of SWNT thin films with conventional semiconductors resulted in the demonstration of high-performance vertical field effect transistors and solar cells.[53, 55]

Here we used a highly transparent film of SC-SWNTs in place of a conventional semiconductor to build a vertical p-SC-SWNT/n-ZnO heterojunction with a high current rectification ratio capable of performing as visible blind UV photodetector with high responsivity and low dark current. In this vertical configuration, UV radiation penetrates the top semitransparent SC-SWNTs layer with low losses (10-20%) and excites photocarriers within n-ZnO layer in the close proximity to the p-SWNT/n-ZnO interface where electron-hole pairs are efficiently separated by high built-in electric field associated with the heterojunction. This work was done in collaboration with Prof. Jianlin Liu group who grew ZnO thin film on sapphire by molecular beam epitaxy method.

3.2 Experimental Section

3.2.1 Preparation of ZnO Layer and SWNTs Thin Film

The ZnO thin film was grown on *c*-sapphire (0001) substrate by Mohammad Sujia in Prof. Jian Lin Liu's group via radio frequency (RF) plasma-assisted SVTA (SVT Associates, Inc.) The ZnO film yields a total thickness of ~400 nm (Figure 3.5a).

Although the film was not intentionally doped, it exhibits n-type behavior with a carrier density of 2.9×10^{17} cm^{-3}, and a resistivity of 6.2 Ω·cm. The aqueous dispersion of 99% SC-SWNTs of large diameter (~1.5 ± 0.1 nm) was purchased from Nanointegris Inc (Figure 3.5b). Semitransparent SC-SWNTs thin films were prepared by vacuum filtration of the SC-SWNTs dispersion utilizing cellulose membrane (Millipore, type VMWP, pore size 0.05 μm) (Figure 3.5c).

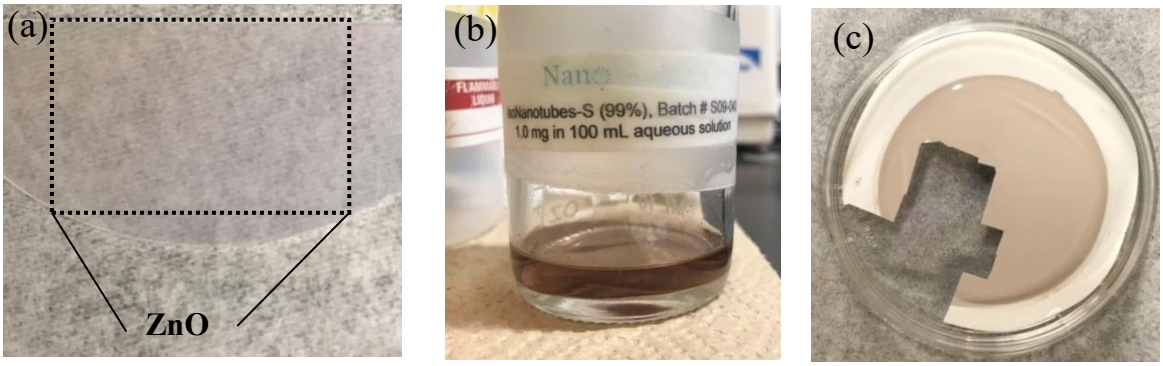

Figure 3.5 (a) ZnO thin film grown on a *c*-sapphire substrate; (b) S-SWNTs dispersion from Nanointegris; (c) SWNTs thin film prepared by vacuum-filtration method.

3.2.2 Device Fabrication

The ZnO film grown on a sapphire substrate was treated by 30% H_2O_2 solution (Fisher Chemical) for 3 min at 100ºC, washed in DI water and dried under nitrogen gas flow according to procedure described in literature.[65-66] SWNTs thin film on cellulose membrane was transferred on the ZnO layer via the membrane dissolution in acetone vapor, and additional washing in acetone and DI water. The thickness of the SC-SWNT film was defined by the amount of filtered SC-SWNT material taking into account the effective area of the membrane and assuming SWNT film density of 0.5±0.1 $g\cdot cm^{-3}$ as

described in our previous reports.[67] The thickness was confirmed by measurement of the optical density of the SC-SWNT layer and Dektak profilometry measurements.[67-68]

3.2.3 Electrical and Photoelectrical Device Characterization

Current-voltage (I-V) measurements were conducted utilizing Keithley 236 Source-Measure Unit employing LabView based acquisition system. UV-Vis-NIR spectra of ZnO and SC-SWNTs films and photoconductivity spectra were collected utilizing Cary 5000 spectrophotometer (Agilent Technologies). Calibrated wideband semiconductor GaP UV photodetector (GaP, Model FGAP71, Thorlabs) was utilized to measure the incident UV light intensity. LED (Model 370E, Thorlabs) with the central wavelength of 370 nm was used as a source of UV radiation for the single wavelength measurements. The LED irradiation was modulated utilizing function generator SRS-DS345 (Stanford Research Systems), and the amplitude of the photoresponse under various light intensities and modulation frequencies were studied using lock-in amplifier (SRS 830, Stanford Research Systems) (Figure 3.6 a, b). The noise voltage V_n on the load resistance R_L= 10 kΩ (Δf = 1 Hz bandwidth) at different frequencies f of UV light modulation was measured utilizing SRS 830 lock-in amplifier signal processing capabilities and converted to the noise current $I_n = V_n/R_L$, where R_L is a load resistance in the detector bias circuit. The temporal traces of the photoresponse were collected utilizing Tektronix TDS 1001C-EDU oscilloscope.

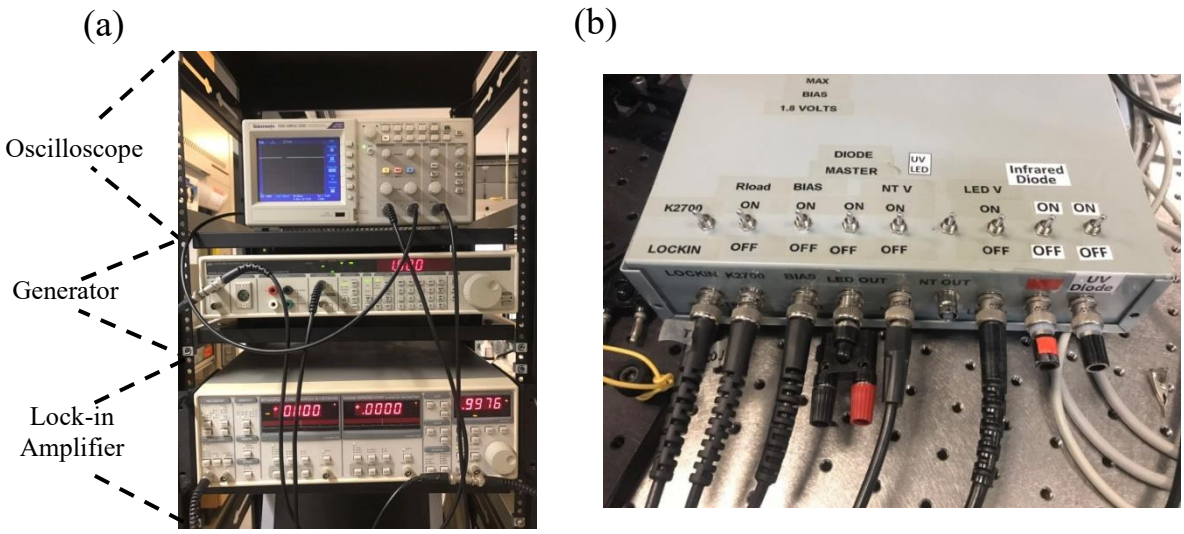

Figure 3.6 (a) Oscilloscope, function generator, and lock-in amplifier system used in the photoconductivity measurement; (b) Control box for connections between photodetector and measuring system in (a).

3.3 Results and Discussions

We prepared the vertical p-n junction based on SWNTs and ZnO thin films by transferring SWNTs thin film on H_2O_2-treated and untreated ZnO and explored the their electric characters in dark. We explore the effect of H_2O_2 treatment on ZnO by comparing the I-V curves of treated and untreated ZnO/SWNTs device in dark. The n-type ZnO layer of 400 nm was grown on *c*-sapphire substrate by molecular beam epitaxy (MBE) technique by Suja in Prof. Jianlin Liu's group (see Experimental Section for details).[29, 69]

For this study, we utilized 99% semiconducting (SC-) SWNTs of large diameter (1.5 ± 0.1 nm). We use the energy value of 0.68 eV corresponding to the position of the

maximum of the optical absorption in the lowest S_{11} absorption band (Figure 3.7) as an average bandgap for these SC-SWNTs. The width of the S_{11} absorption band at half maximum of absorption also gives a width of the bandgaps distribution of ± 0.07 eV for the ensemble of the SC-SWNTs.

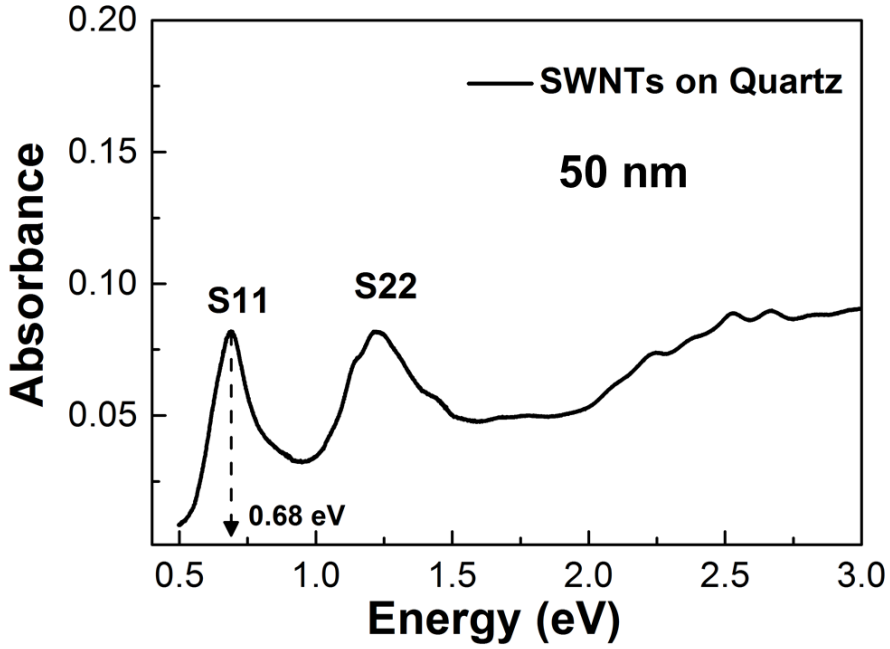

Figure 3.7 The UV-Vis spectra of absorption of the SWNTs thin film with the thickness of 50 nm.

A schematic of the vertical p-SC-SWNT/n-ZnO heterojunction device is presented in Figure 3.8a. A rectangular fragment of semitransparent SC-SWNT film with an effective thickness of 50 nm, a length of 2 mm and a width of 1.2 mm was transferred on the ZnO layer. Prior to the SWNT film transfer, the ZnO layer was pretreated with hydrogen peroxide in order to tune the band bending and the conduction band offset at the p-SC-SWNT/n-ZnO interface.[24, 65-66, 70] Two indium electrodes were deposited to complete the

device fabrication: one electrode provides an electrical contact to the top SC-SWNT film layer (just outside the ZnO layer), and the second electrode addresses the bottom ZnO layer just outside the SC-SWNT film. This configuration carries some lateral motif, as the charge carriers travel in lateral direction along the SWNT thin film and ZnO layer before entering or exiting the vertical heterojunction. However, as we show below, the voltage drop associated with such lateral current is several orders of magnitude smaller than the voltage drop across the heterojunction when it is reverse-biased, so it effectively acts as a vertical heterojunction. For comparison, a lateral n-ZnO device of the same area with two indium electrodes, as shown in Figure 3.8 b, was investigated.

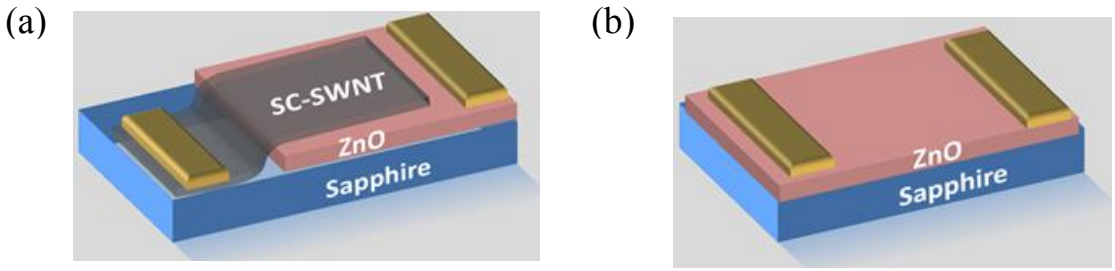

Figure 3.8 (a) Schematic of vertical p-SC-SWNT/n-ZnO heterojunction; (b) Structure of lateral In-ZnO-In device.

Figure 3.9a shows the I-V characteristics of p-SC-SWNT/n-ZnO heterojunction devices with and without hydrogen peroxide pre-treatment of the ZnO surface. Without the pre-treatment no significant rectification was observed while the device with pre-treated ZnO surface showed a significant degree of rectification of about 10^3 at ± 2.0 V. In contrast, the lateral ZnO device with pre-treated ZnO surface layer shows a linear I-V curve (Figure 3.9b) corresponding to ohmic In-ZnO contacts and a lateral resistance of

the ZnO layer of 7×10^5 Ω. Additional measurements provide a value of the lateral resistance of SC-SWNT film of ~20 kΩ as shown below.

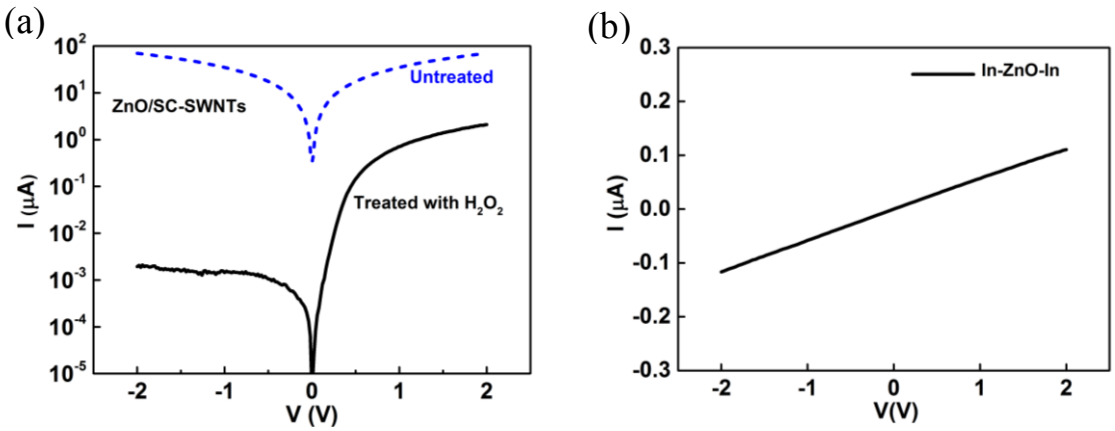

Figure 3.9 (a) I-V curves of the p-SC-SWNT/n-ZnO heterojunction before (dashed line) and after (solid line) hydrogen peroxide treatment; (b) I-V curves of the lateral In-ZnO-In device.

One should note, that in any vertical optoelectronic device, the lateral travelling of the carriers is inevitable independent on the nature of the top transparent conducting electrode, but the resistance and voltage drop associated with such lateral current should be minimized. Both lateral resistances are orders of magnitude smaller than the total resistance of the device of 10^9 Ω at a negative bias -2.0 V, which is dominated by the resistance of the heterojunction, thus supporting the earlier statement of functionally dominating vertical motif of the device architecture.

Figure 3.10a presents the sketch of the heterojunction device under UV illumination and Figure 3.10b shows I-V curves of the p-SC-SWNT/n-ZnO heterojunction device in dark and under illumination from an ult raviolet LED (central wavelength λ=370 nm) of an incident light intensity of 3 μW/cm^2 (power P=75 nW).

Multiple p-SC-SWNT/n-ZnO heterojunction devices were prepared following the procedure described above showing a similar dark rectification of the I-V curve and a similar photoresponse to UV irradiation. At the negative bias of -2.0 V, the dark current is 2 nA and the photocurrent approaches 3 μA which corresponds to UV photoresponsivity of 40 A/W.

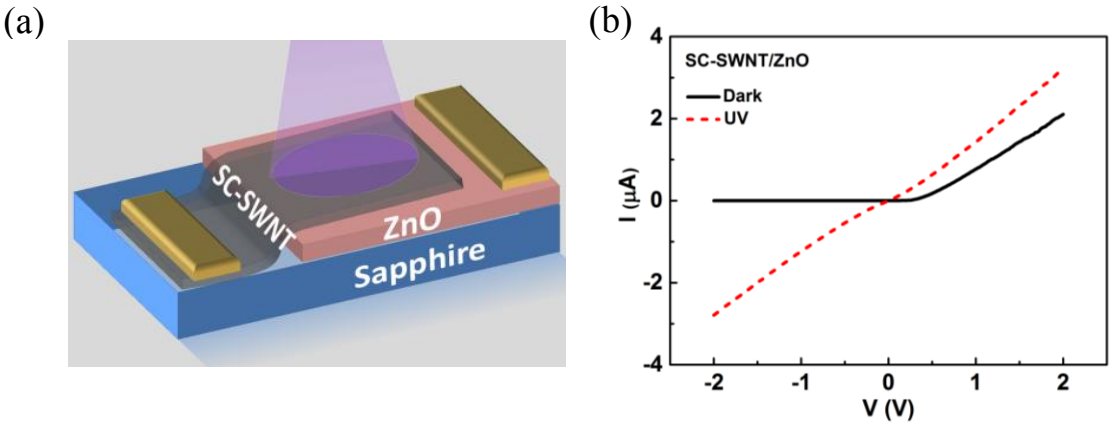

Figure 3.10 (a) Schematic of p-SC-SWNTs/n-ZnO heterojunction under UV irradiation. I-V curves of SC-SWNT/ZnO heterojunction (b), lateral In-ZnO-In device (c), and lateral In-SWNT-In device (d) in dark (black solid curves) and under UV (370 nm, 3μW/cm^2) irradiation (red dashed curves).

In comparison, lateral In-ZnO-In device shows much lower photoresponsivity of < 1 A/W and much higher dark current of 120 nA as shown in Figure 3.11a. As an alternative to the vertical architecture, the lateral device can be improved by introducing Schottky barrier type interdigitated electrode configuration with higher width to length aspect ratio and a higher photocarriers collection efficiency associated with shorter inter-electrode distance and presence of a Schottky barrier introducing high built-in electric field separating the photoexcited electron-hole pairs at the ZnO-metal interface.[27-28, 71]

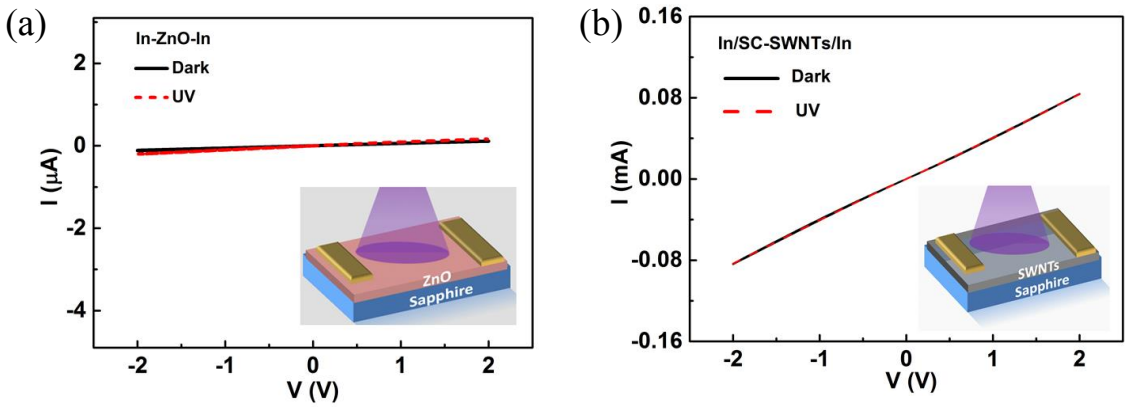

Figure 3.11 (a) I-V curves of lateral In-ZnO-In device (a), and lateral In-SWNT-In device (b) in dark (black solid curves) and under UV (370 nm, 3μW/cm^2) irradiation (red dashed curves).

Figure 3.11b shows I-V characteristics of p-SC-SWNT film of the same thickness and lateral dimensions as in the heterojunction device with similar indium electrodes. Those I-V curves are linear with the slope corresponding to the value of the lateral resistance of SC-SWNT film of ~20 kΩ, and no measurable photocurrent was observed under UV illumination. We should note that indium electrode would make a Schottky type contact to p-type individual SWNT, and the corresponding I-V curve would have been non-linear. However, in the case of macroscopic (mm size) SWNT thin film the total resistance of the SWNT network is usually dominated by the resistances of thousands of intertube junctions with negligible contact resistance between the large area indium electrode and SWNT film (as confirmed by 4-probe measurements), resulting in linear I-V curve as shown in Figure 2d.

The presented comparison of the performance of individual components of the device indicates that introduction of a vertical structure with p-SC-SWNT/n-ZnO

heterojunction provides a significant gain of UV photoresponse in comparison with utilization of the same n-ZnO UV sensitive layer in lateral configuration. To verify this point, a micrometer controlled narrow slit diaphragm of width 200 μm was used to measure the device photoresponse as a function of the position of illumination spot across the width of the device as schematically shown in Figure 3.12a. The scan width includes the areas of ZnO layer not coated with SC-SWNT film (see positions 1 and 5 in Figure 3.12a). The resulted photoresponse scan is presented in Figure 3.12b and shows high photocurrent values of ~ 1 μA when the UV light (λ=370 nm) illuminates the area of p-SC-SWNT/n-ZnO heterojunction (positions 2-4) and a decrease of photocurrent by 50 to 100 times when the UV irradiated spot moves from the SC-SWNT film to the adjacent ZnO area (positions 1 and 5).

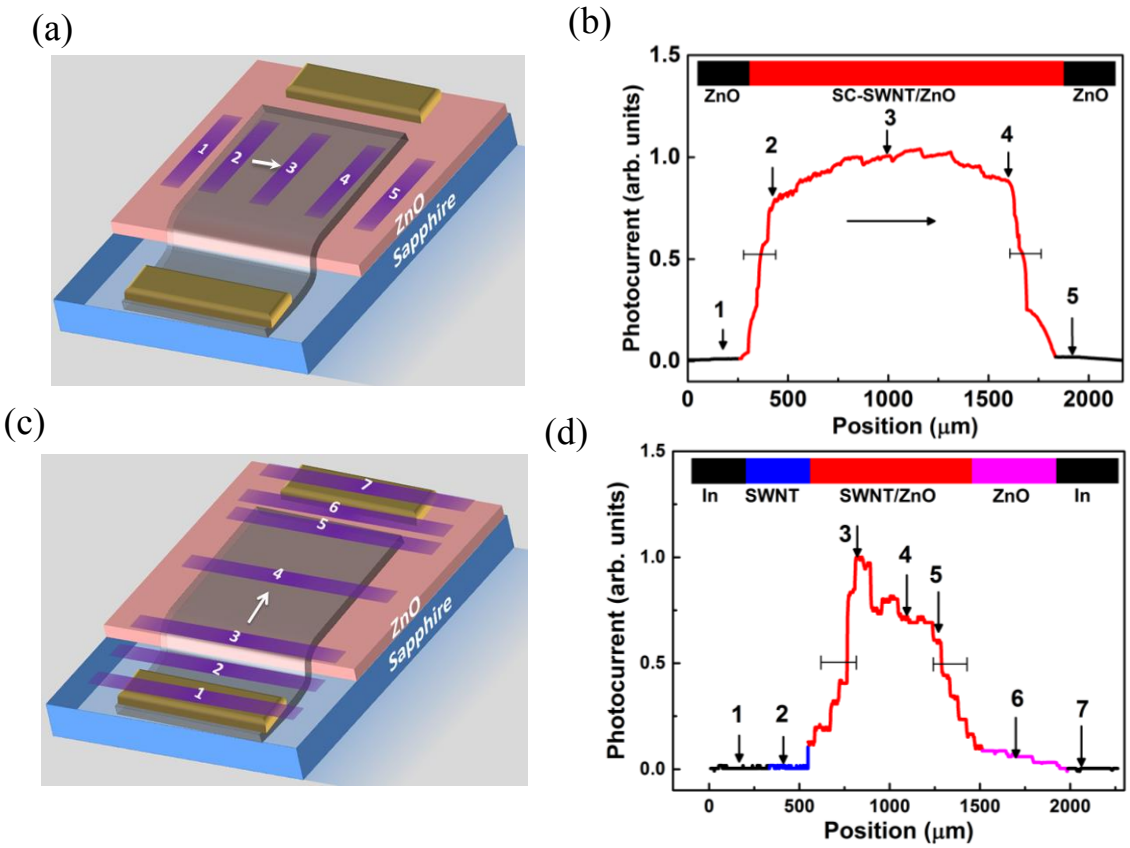

Figure 3.12 (a) Schematic of position dependent photocurrent measurements across the width of p-SC-SWNT/n-ZnO heterojunction device and (b) corresponding photocurrent measurements as a function of position across the device at the reverse bias of -2 V. (c) Schematic of position dependent photocurrent measurements along the length of p-SC-SWNT/n-ZnO heterojunction device and (d) corresponding photocurrent measurements as a function of position along the device at the reverse bias of -2 V. Horizontal error bars in (b) and (d) show a spatial resolution corresponding to the width of the slit diaphragm.

Another scan was conducted along the length of the device across the space between indium electrodes as illustrated in Figure 3.12c and the results of the scan are presented in

Figure 3.12d. To conduct this scan, the heterojunction device was modified by increasing the length of the uncovered ZnO layer between the edge of SC-SWNT film and the indium electrode from 100 to 500 μm, while the length of the heterojunction area in this device was 700 μm. The scan showed no photoresponse in the SC-SWNT film area adjacent to the 1st indium electrode (position 2), strong photoresponse in the central area where the ZnO and SWNT layers overlap (positions 3-5), and a significant drop of the photoresponse in the area adjacent to the 2nd indium electrode where only ZnO layer is present. Thus, to achieve efficient UV photoresponse the photoexcited carriers should be generated in the ZnO layer covered by SWNT film in the vicinity of p-SC-SWNT/n-ZnO interface.

UV-Vis-NIR absorption spectra of the ZnO and SC-SWNT layers and the spectral dependence of the photoresponse are presented in Figure 3.13a and 3.13b, respectively. The onset of strong absorption in ZnO layer appears at a wavelength near 380 nm with absorption maximum (ABS=1.8) at 370 nm in agreement with the known bandgap of ZnO of 3.37 eV.[21-23]

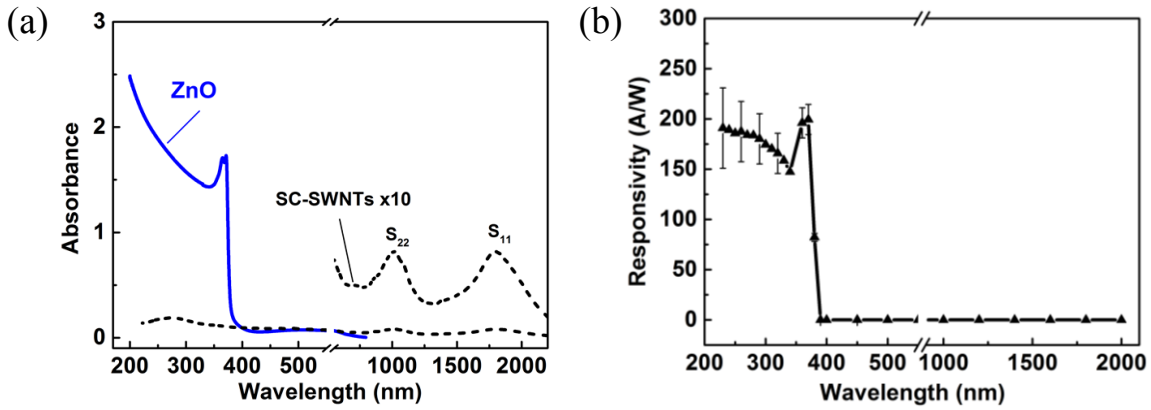

Figure 3.13 (a) UV-Vis-NIR absorption spectra of ZnO (blue solid curve) and SC-SWNTs thin films (black dashed curve); (b) Spectral dependence of photoresponsivity of p-SC-SWNT/n-ZnO heterojunction at the incident power of 10 nW (light intensity of 250 nW/cm^2) at -2 V bias.

Absorption of semitransparent 50 nm thick film of SC-SWNT is only 0.1 at 370 nm (transmittance of 79%) because of its small thickness sufficient to form the heterojunction and, at the same time, to function as a transparent conducting electrode. The UV absorption is averaging 0.15 in the range of SWNT π-plasmon maximum 220-330 nm. The thickness of the SWNT film can be further decreased to less than 10 nm (transmittance >90%) in order to reduce the loss of UV light intensity. The characteristic absorption bands S_{11} and S_{22} corresponding to the set of separations between van Hove singularities of one-dimensional SC-SWNTs appear in near-IR spectral range centered around wavelength 1750 and 1000 nm, respectively, with the maximum of absorption not exceeding a value of 0.1 in the near-IR and visible spectral range as shown in Figure 3.10a.

Figure 3.13b shows the spectral responsivity of the p-SC-SWNT/n-ZnO heterojunction device. The onset of photoconductivity appears at 380 nm with the photoresponsivity reaching ~200 A/W at 370 nm and extending from UB-A to UV-B and UV-C spectral range at least up to wavelength of 230 nm, the spectral limit of our instrumentation. These photoresponsivity values are on the high end of the typical values achieved for UV photodetectors,[11, 21-23, 37-41] however recently, much higher photoresponsivity values such as 26000 and 1.7×10^{6} A/W were reported for interdigitated Au/ZnO and ZnO quantum dots/carbon nanodots based devices, respectively.[43, 45]

In the visible spectral range the photoresponse drops practically to zero; more accurate responsivity measurements utilizing blue (λ=470 nm), yellow (λ=520 nm) and red (λ=630 nm) LEDs with the incident power in the range from 1 μW to 0.2 mW were performed. For blue and red LEDs measurable photoresponse was observed and the resulted responsivities were evaluated at the level of 10^{-3} A/W and 1×10^{-5} A/W, respectively (Figure 3.14). For yellow LED no measurable photoresponse was observed as the power was limited to 5 μW and the level of responsivity not exceeding 4×10^{-5} A/W was estimated from the measured noise of the photodetector current under a reverse bias of -2 V. Thus, we conclude that the current responsivity in the visible range does not exceed 0.001 A/W, and UV to visible light responsivity ratio exceeds 10^{5} making the p-SC-SWNT/n-ZnO heterojunction photodetector, practically, visible blind. The visible blindness is an important benefit for UV photodetector application taking into account the high intensity of the background visible radiation in the typical UV photodetector applications.

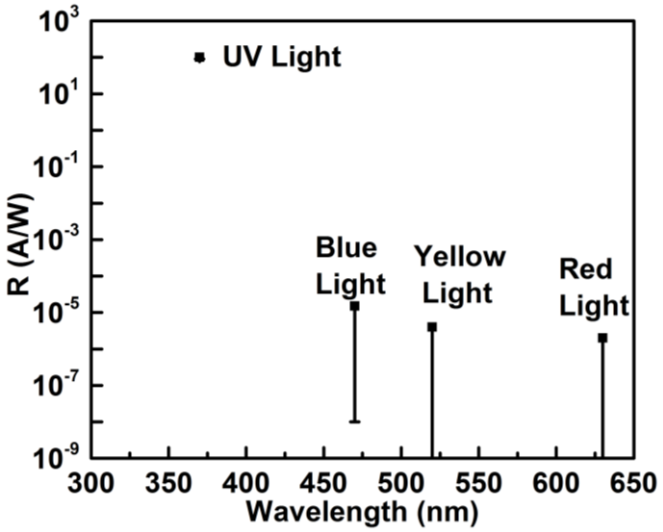

Figure 3.14 Current photoresponsivities of p-SC-SWNT/n-ZnO vertical heterojunction device measured using irradiation from UV, blue, red and yellow LEDs with the central wavelengths λ= 370, 470, 520, and 630 nm, respectively, with incident LEDs irradiation power in the range from 100 nW to 0.2 mW, under reverse bias of -2 V.

It should be noted that graphene is an alternative carbon based nanostructured material, which has been utilized as a transparent conducting electrode for wide range of optoelectronic applications, and it can also be n- or p-doped depending on the application needs.[72] Recently, several reports presented UV photodetectors based on junctions of graphene with the arrays of ZnO nanowires or nanorods, demonstrating high UV range responsivity up to 113 A/W and millisecond range response times.[11, 73] However, these graphene based photodetectors are not visible blind as they show photosensitivity not only in UV range, but also in visible and near-IR range, which was associated with either continuous spectral absorption in the gapless graphene or defects in ZnO and graphene layers.[11, 73]

Figure 3.15a presents a temporal photoresponse of the p-SC-SWNT/n-ZnO heterojunction device to square-wave pulses of UV radiation of an incident power of 3 μW/cm^2 generated by UV LED (λ=370 nm) electrically modulated at a low frequency of 0.005 Hz. It shows a relatively fast onset of the photocurrent followed by slow approach to saturation with 10-90% rise and decay times of 14s and 23 s, respectively.

Frequency dependence of the photoresponse is presented in Figure 3.15b: it shows decreasing responsivity R with increasing frequency which can be fitted to $R \propto f^{-\alpha}$ dependence with an exponent α=0.5 usually associated with a wide distribution of lifetimes of the photoexcited carriers in the range from tens of seconds to milliseconds. For comparison, the temporal response of the lateral In-ZnO-In device measured under the same irradiation conditions is presented in Figure 3.15c. It shows significant non-zero dark current and ~6 times smaller amplitude of the current modulation. Corresponding 10-90% rise and decay times exceed 100 s and 600 s, respectively. Thus, introduction of SWNT/ZnO heterojunction not only enhance the amplitude of the photoresponse, but also makes it significantly faster in comparison with the lateral In-ZnO-In device. In fact, a measurable photoresponse of the SWNT/ZnO heterojunction device can be observed up to frequency of 2000 *Hz* as can be seen in the oscilloscope traces presented in Figure 3.15d.

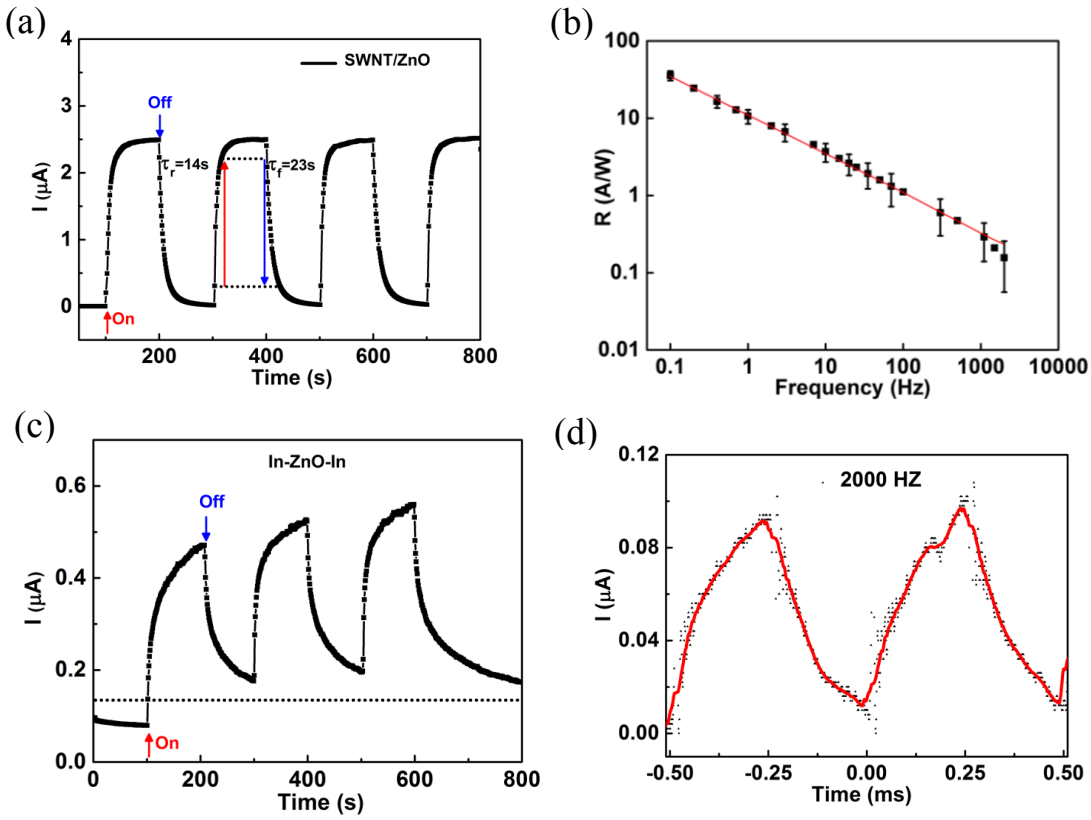

Figure 3.15 (a) Temporal photoresponse of p-SC-SWNT/n-ZnO heterojunction device under 370 nm light at frequency 0.005 Hz; (b) Frequency dependence of photoresponse under UV light intensity of 2 μW/cm^2 (squares); straight lines correspond to $R \propto f^{-\alpha}$ fitting with α=0.5; (c) Temporal photoresponse of In-ZnO-In lateral device under 370 nm light at frequency 0.005 *Hz* (V_{bias}=-2V); (d) Oscilloscope traces of photoresponse of p-SC-SWNT/n-ZnO heterojunction device at 2000 Hz. V_{bias}= -2V for all plots (a-d).

Figure 3.16a presents dependences of the photocurrent on the incident power of the UV radiation at the LED central wavelength λ=370 nm. At the UV light intensity range of 1 to 100 nW/cm^2 a practically linear relationship between the photocurrent and

incident power is observed which changes to a sublinear dependence with a tendency to saturation under further increase of the incident power.

Figure 3.16b presents corresponding photoresponsivity *R*. At lower incident UV light intensity below 100 nW/cm^2 responsivity reaches 400 A/W, which is on the high end of the typical values reported for UV detectors,[11, 21-23, 37-41] although much higher values up to 1.7×10^6 A/W have been reported recently.[43, 45] With increasing light intensity above 400 nW/cm^2, the photoresponsivity decreases below 100 A/W, but sustains quite high value of ~ 10 A/W at an incident power of a few μW/cm^2. Such tendency of the photoresponse towards saturation and corresponding photoresponsivity decrease with increasing power indicate an involvement of the trap states in the mechanism of photoconductivity as we discuss below.

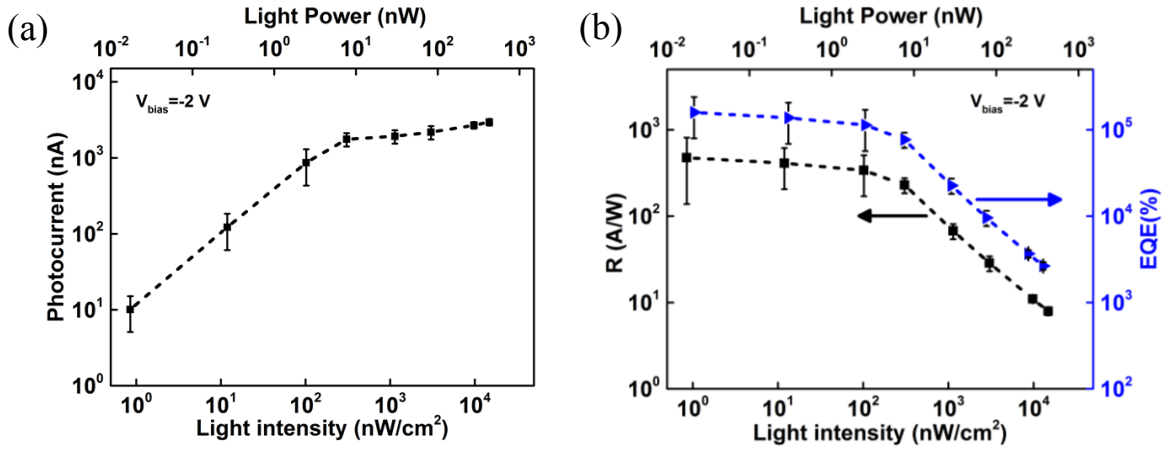

Figure 3.16 (a) Photocurrent and (b) photoresponsivity (black squares) and external quantum efficiency (blue triangles) of p-SC-SWNT/n-ZnO heterojunction device as a function of incident 370 nm light intensity at reverse bias of -2V.

The external quantum efficiency (*EQE*) of the photodetector can be evaluated at wavelength λ=370 nm using the following equation:

$$EQE\% = \frac{R \times 1240}{\lambda} \times 100 \qquad (3.1)$$

The resulting plot of EQE as a function of the UV light intensity is presented in Figure 3.8b and shows high EQE value up to 1.0×10^5 % indicating a high photocurrent gain associated with long photocarriers lifetimes due to efficient separation of photoexcited electron and holes.

A major figure of merit of the detector performance specific detectivity, *D**, of UV photodetectors is often evaluated on the basis of quasi-static measurements using the following equation under assumption that the noise current is dominated by the shot noise from the dark current I_{dark} of the device:[38, 40-41, 74]

$$D^* = \frac{R}{(2e \times I_{dark}/A)^{\frac{1}{2}}} \qquad (3.2)$$

where *R* is current responsivity (A/W), *e* is the electron charge (1.6×10^{-19} Coulombs), and *A* is the effective area of the photodetector. Using experimental dark current value of 2 nA at reverse bias (-2 V) and active detector area of 2x1.2 mm^2 (0.024 cm^2) a *D**=3.2x10^{15} $Hz^{1/2}$cm/W can be obtained which is comparable to the best values reported for UV photodetectors under the same noise origin assumptions.[38-40] More general evaluation of the detectivity *D** can be obtained on the basis of following equation:[75]

$$D^* = \frac{R(A\Delta f)^{\frac{1}{2}}}{\mathrm{NEP}} = \frac{R(A\Delta f)^{\frac{1}{2}}}{I_n} \qquad (3.3)$$

where *NEP* is noise equivalent power of the detector at UV light modulation frequency f, I_n is a root mean square (RMS) value of the measured noise current in the detector circuit

in the electrical bandwidth Δf (Hz), and a relationship $NEP = I_n/R$ is utilized. For calculations at UV light modulation frequency of 10 Hz, experimental values of current responsivity and noise current of 30 A/W and 6×10^{-12} A, respectively, were utilized resulting in NEP=2×10^{-13} W/Hz$^{1/2}$ and a more realistic value of D*=0.8×10^{12} (Hz$^{1/2}$*cm)/W. Such difference in D* values obtained using equations 2 and 3 indicate that in addition to shot noise other sources of noise such as a "flicker" ($1/f$) noise and Johnson noise are important in the case of our p-SC-SWNT/n-ZnO heterojunction, and further optimization of the components of the heterojunction device is required. For example, decreasing of a series resistance of the photodetector by optimizing the preparation and processing of ZnO layer can significantly reduce both Johnson and $1/f$ noise and improve the linearity of the detector response.

Majority of studies on ZnO based UV photodetectors and other inorganic UV detectors report responsivity values in the range of 1 mA/W to 10 A/W and response times of a few seconds to hundreds of seconds typically limited by oxygen desorption-absorption processes under UV irradiation.[21-22, 37-38, 76] Faster response times in sub-second range were recently reported on ZnO based nanostructured systems, but with responsivities in mA/W range.[77] High responsivity values in the range 100 to 1000 A/W were reported for nanostructured forms of ZnO,[11, 41, 46] and, recently, a significant enhancement of the responsivity up to 1.7×10^6 A/W was reported.[43, 45] Also, in some of the recent reports the response time was reduced to milliseconds and sub-millisecond range, however, with reduced UV to visible responsivities ratio (<100).[11, 41] In our p-SC-SWNT/n-ZnO heterojunction UV detector, a significant response can be observed up to a

frequency of 2000 Hz (Figure 5d) indicating a presence of fast processes which can be potentially enhanced by tuning the properties of SWNT and ZnO layers, their geometry and the photocarriers extraction pathways.

In order to describe the current transport in our p-SC-SWNT/n-ZnO heterojunction device in dark and under UV illumination we applied a model developed for the case of p-Ge/n-GaAs heterojunction.[78-79] It should be noted that the SC-SWNT film itself presents a complex network of entangled SWNTs with the electrical transport limited by the charge carriers hoping (tunneling) across the intertube junctions, while here, for simplicity, SC-SWNT layer is treated as a bulk conventional semiconductor with bandgap $E_g \approx 0.68$ eV,[80] evaluated from the absorption spectrum of the SC-SWNT film (Figure 3.7) and close to E_g of Ge of 0.67 eV at 300 K. [80] The band diagram schematic of p-SC-SWNT and n-ZnO layers after establishing of the heterojunction is presented in Figure 3.17a in detail.

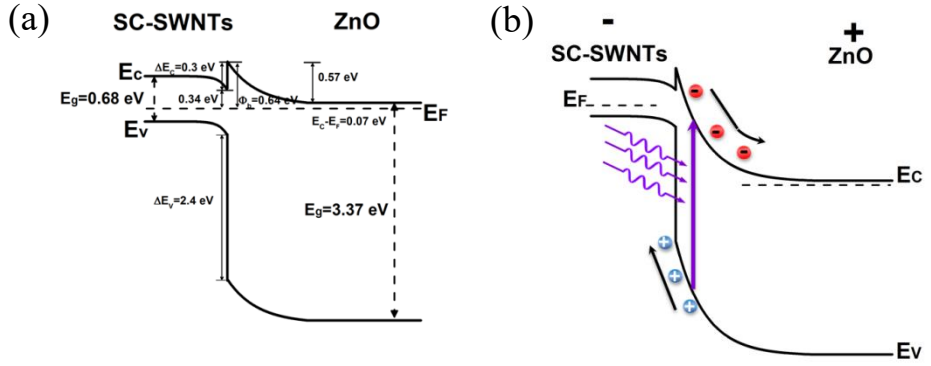

Figure 3.17 (a) Band diagram of p-SC-SWNT/n-ZnO heterojunction under zero bias; (b) Band diagram of p-SC-SWNT/n-ZnO heterojunction under reverse bias and UV illumination showing photoexcitation of electron-hole pairs and their separation in ZnO layer in the vicinity of heterojunction interface.

For the construction of the band diagram, the work function and electron affinity χ_{SWNT} of p-type SC-SWNTs are 4.3 and 4.8 eV, respectively, based on literature report.[55, 81-82] The electron affinity of ZnO, χ_{ZnO}, is 4.0±0.2 eV.[21-24, 83] According to R. L. Anderson consideration of heterojunction the conduction band discontinuity ΔEc is equal to the difference of the electron affinities of the contacting materials thus giving $\Delta Ec = \chi_{SWNT} - \chi_{ZnO} \approx 0.3\pm0.1$ eV,[78-79] and the corresponding valence band discontinuity ΔEv can be estimated as $\Delta Ev = Eg_{ZnO} - Eg_{SWNT} - \Delta Ec \approx 2.4$ eV. [78-79] With the majority carrier (electron) concentration in n-ZnO of $n \approx 2.9\times10^{17}$ cm^{-3} obtained from Hall effect measurements, the minority carrier (hole) concentration p is extremely low ($p \approx 1.7\times10^{-37}$ cm^{-3}), and the calculated Fermi level position is 0.07 eV below the conduction band edge E_C as described in detail as follows:

Using carrier concentration in ZnO obtained from Hall effect measurements n=2.9×10^{17} cm^{-3}, the position of Fermi level (E_F) below the conduction band (E_c) can be obtained using the Expression 3.4:[84]

$$E_F - E_i = kT\ ln\frac{n}{n_i} \qquad (3.4)$$

where n_i is the carrier density in intrinsic ZnO:

$$n_i = \sqrt{N_V N_C} \times e^{-E_g/2kT} \qquad (3.5)$$

where $N_C = 2(2\pi\ m_n{*}kT/h^2)^{3/2}$ and $N_V = 2(2\pi\ m_p{*}\ kT/h^2)^{3/2}$ are the effective densities of states in conduction and valence bands, respectively; m_n^* and m_p^* are the effective masses of electrons and holes in ZnO, respectively ($m_n^* = 0.24\ m_0$; $m_p^* = 0.45\ m_0$);[85] m_0=9.11×10^{-31} kg is free electron mass, k is the Boltzmann constant (1.38×10^{-23} J/K), T

is the room temperature (295 K); h is the Planck's constant (6.63×10^{-34} J-s), n is equilibrium carrier concentration in conduction band; E_C, E_V, E_F, E_G are conduction band, valence band, Fermi level, and bandgap of ZnO, respectively. Based on the Equations 3.4 and 3.5, we obtain the intrinsic carrier concentration in ZnO $n_i \approx 0.7 \times 10^{-10}$ cm^{-3} and $E_C - E_F = Eg/2 - (E_F - E_i) \approx 0.07\ eV$. Using the relationship of the constant product of the electron and hole concentrations,[84] $n \times p = n_i^2$, independent on the Fermi level position, gives an estimation of the minority carrier (hole) concentration in n-ZnO of $p \approx 1.7 \times 10^{-37}$ cm^{-3} which is extremely low.

Following the reported theoretical calculations of the carrier density in SC-SWNTs [86]we estimated the hole and electron concentrations in environmentally p-doped SWNTs of a diameter ~1.5 nm as $p_{SWNT} \approx 5\times10^{19}$ cm^{-3} and $n_{SWNT} \approx 6\times10^{13}$ cm^{-3}, respectively. Very often, in one-dimensional case linear carrier concentrations (per SWNT length) are utilized: the above obtained volume concentrations correspond to linear hole and electron concentrations of $\sim1.4\times10^{5}$ cm^{-1} and $\sim1.7\times10^{-1}$ cm^{-1}, respectively. An independent estimation on the basis of the measured electrical conductivity of p-SC-SWNT film of ~30 $\Omega^{-1}cm^{-1}$ and a typical mobility in the range 1-10 cm^2/Vs gives similar values of majority (hole) carrier densities in the range of $p_{SWNT} \approx 10^{19}$-10^{20} cm^{-3}. Therefore, the hole and electron concentrations in environmentally p-doped SC-SWNTs were estimated at the level of $p_{SWNT} \approx 5\times10^{19}$ and $n_{SWNT} \approx 6\times10^{13}$ cm^{-3}, respectively, as discussed above. Corresponding hole and electron linear concentrations (per p-SC-SWNT length) are estimated as $\sim1.4\times10^{5}$ cm^{-1} and $\sim1.7\times10^{-1}$ cm^{-1}, respectively.

According to previous reports, hydrogen peroxide treatment leads to the removal of highly conducting electron accumulation layer formed by several monolayers of hydroxide, and generation of Zn vacancies within depth of few hundred nanometers resulting in an upward band bending in the vicinity of the p-SC-SWNT/n-ZnO interface up to 0.6 eV, which correlates with our experimental observation of four-fold increase of the lateral resistance of the ZnO layer.[65, 83] In addition, during the heterojunction formation, the work function difference forces the electron transfer from n-ZnO to p-SC-SWNTs resulting in the increase of upward band bending in the n-ZnO layer close to the interface and corresponding downward band bending in the p-SC-SWNT layer. Downward band bending at the SC-SWNT side towards the intrinsic state is confirmed by the observed ~3 times increase of the lateral resistance of the SC-SWNT layer compared to similar SC-SWNT film transferred to a glass substrate. It also correlates with the partial restoration of the strength of the S_{11} absorption band after transfer of the SWNT film on top of the ZnO layer as would be expected in case of reduced average level of p-doping across the thickness of the SC-SWNT layer.

The distance between Fermi level and a peak value of *Ec* in ZnO estimated to be ϕ_b = 0.64 ±0.1 eV which together with a conduction band discontinuity ΔEc of ~0.3±0.1 eV is responsible for the high rectification ratio of the *I-V* curve (Figure 3.18). Fitting of the experimental *I-V* curve to the expression describing thermionic emission across the Schottky barrier at the metal-semiconductor junction (Figure 3.15)[84] as described below:

$$I = I_0 \times \left[e^{\frac{q(V-IR_S)}{nkT}} - 1 \right] \qquad (3.6)$$

$$I_0 = A \times A^* \times T^2 \times e^{(-\frac{q\phi_b}{kT})} \qquad (3.7)$$

where I_0 is the saturation current, ϕ_b is the barrier, q is the absolute value of electron charge, R_s is the series resistance, n is the ideality factor, k is the Boltzmann constant, T is the room temperature (K), A is the area of the device, A^* is the effective Richardson constant. The following numerical values were utilized:

$A = 2.4 \times 10^{-6} m^2, T = 295\ K, A^* = 1.2 \times 10^{-6} A \cdot m^{-2} \cdot K^{-2}$. [66]

Using Equation 3.7 and a value of series resistance R_S =700 kΩ, and a Schottky barrier height of 0.806 eV. This number is larger than the above value of ϕ_b= 0.64±0.1 eV, which may be due to the limitations of the utilized Schottky barrier approximation.

A satisfactory fitting of the experimental I-V with Equation 3.6 was obtained, as shown in Figure 3.15, with fitting parameters R_s=700 kΩ and n=1.95.

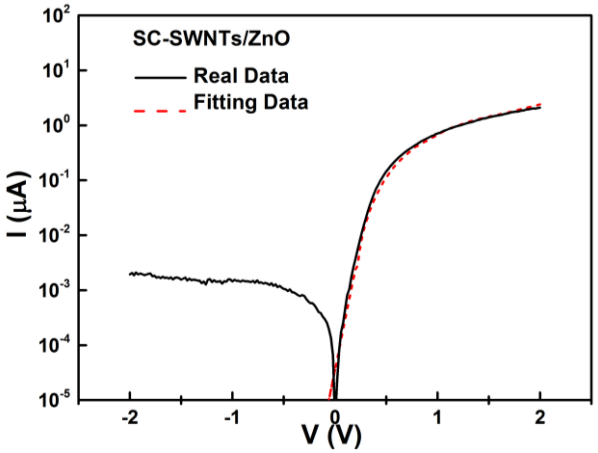

Figure 3.18 Experimental I-V curve of SC-SWNTs/ZnO heterojunction in dark and the fitting curve based on the procedure described above.

Under the reverse bias (negative polarity on the SWNT side) the flow of holes (minority carriers in n-ZnO) to the SC-SWNT layer can be neglected because of the large

bandgap and n-type doping of the ZnO layer, and the overall current is provided by electron transport from SWNTs to ZnO. The I-V curve in Figure 3.9a shows that the reverse current remains low, at the level of ~2 nA, as it is limited by the barrier ϕ_b which also includes the conduction band discontinuity ΔE_c. The forward dark current is ~ 3 orders of magnitude larger than the reverse current at similar bias because of reduced band bending at the n-ZnO side, and is dominated by electron (n-ZnO majority carriers) flow into the SC-SWNT layer as the hole component of the current from SWNTs to ZnO should be negligible due to a large barrier ΔE_v corresponding to the valence band discontinuity. This description does not take into account tunneling and recombination processes which may be important for the current transport across the heterojunction.[87]

The mechanism of photocurrent of p-SC-SWNT/n-ZnO heterojunction is illustrated qualitatively in Figure 3.17b. UV illumination with photon energies higher than the bandgap of ZnO of 3.37 eV (λ<368 nm) enters the ZnO after passing through the semitransparent SC-SWNT layer with small losses (~10-20%) and excites electron-hole pairs in close proximity to the SC-SWNT/n-ZnO heterojunction interface in the region of the maximum band bending and the highest built-in electric field associated with the heterojunction formation. The reverse bias enhances the band bending and a built-in internal electric field on the ZnO side in the vicinity of the p-SC-SWNT/n-ZnO interface leading to efficient separation of photoexcited electrons and holes before they recombine.

UV illumination with photon energies higher than the bandgap of ZnO of 3.37 eV (λ<368 nm) enters the ZnO after passing with small losses (~10-20%) through the semitransparent SC-SWNT layer and excites electron-hole pairs which are being

separated by the high electric field in the n-ZnO layer adjacent to the p-SC-SWNT/n-ZnO interface before they recombine. The photoexcited holes are being swept into SC-SWNT layer and electrons from the depleted high resistance ZnO interface layer to the bulk (deep) n-ZnO layer of higher electrical conductivity. In this configuration p-doped SC-SWNT film acts as a transparent electrode and also as a hole current collector, simultaneously, while the deep n-ZnO layer act as current collectors delivering photoexcited electrons and holes towards the respective indium ohmic contacts thus completing the photocurrent circuit.

The improved photoresponse is associated with the most efficient use of the whole area of the heterojunction which is illuminated by UV light through the highly transparent SC-SWNT film and the preferential photoexcitation of electron-hole pairs in the region of the highest built-in electric field leading to the efficient separation and collection of photoexcited carriers. Relatively large barrier ϕ_b = 0.64±0.1 eV which also includes the conduction band discontinuity $\Delta Ec \approx 0.3$ eV limits the dark current to the low value of ~ 2 nA resulting in the high on/off contrast.

The frequency dependence of photoresponsivity $R \propto f^{-\alpha}$ with exponent α =0.5 (Figure 3.16a) indicates a wide distribution of lifetimes of photoexcited carriers and points out to contribution of traps, such as Zn vacancies, capturing and releasing one type of carriers thus extending the photocarrier lifetimes and enhancing the photocurrent, but also slowing down the photoresponse.[88]

At high intensity of UV radiation, the limited concentration of available trap states and a shift of quasi-Fermi level in ZnO lead to a saturation of the photoresponse as

observed in Figure 3.16b.[88] Another possible cause of saturation is the relatively high series resistance of ZnO layer limiting the photocurrent. The photons with energy below the ZnO bandgap, but higher than the bandgap of SC-SWNTs (E_g=0.68 eV), are capable to excite electron-hole pairs within the SC-SWNT layer, but strong electron-phonon interaction in 1D-SWNTs leads to the formation of exciton bound states within the time frame of less than 10^{-12} s following by the energy relaxation to the lattice phonons (heat) as shown by theoretical study,[89] and experimentally, utilizing time-resolved fluorescence,[90] polarized pump-probe photomodulation and photoluminescence,[91] two-photon excitation technique,[92] and bolometric spectroscopy.[59] This difference in UV and visible mechanisms of photoexcitation in ZnO and SC-SWNTs, respectively, leads to the observed high UV to a visible photoresponsivity ratio exceeding 10^5.

Under forward bias a positive photocurrent was observed leading to a quasi-linear I-V curve under UV light irradiation which is unusual for the case of photodiode or heterojunction based photodetectors. It should be noted that the equivalent circuit of heterojunction (or photodiode) includes a series resistor of ZnO layer, which is quite large (700 kΩ) in our heterojunction device and originates from the lateral flow of the charge carriers in the ZnO layer. Thus, some contribution to the positive photoresponse in the forward bias can come from the ZnO layer acting as a photoresistor. On the other hand, similar observations of positive photoresponse in forward bias and a linear I-V curve were reported for the cases of Au - ZnO nanowire - Au device and graphene-ZnO nanorod device.[11, 16] In those reports it was suggested that the holes generated by UV irradiation refill (compensate) the deep traps responsible for the depletion region and the

upward band bending in the ZnO layer adjacent to the interface, thus reducing the height of the potential barrier responsible for the rectification of the I-V curves which can be an alternative explanation of the nature of the photoresponse observed in our SWNT-ZnO heterojunction device. The exact nature of the photoresponse needs to be clarified in future studies.

The detector performance can be further optimized by tuning the degree of doping of the SWNT and ZnO layers, the thickness of both layers, and the surface treatment of ZnO for further improvement of rectification ratio and enhancement of internal electric field for more efficient separation and extraction of photoexcited carriers. The linearity (dynamic range) of the response can be improved by decreasing the series resistance of the device associated with the lateral transport of extracted photocarriers along the ZnO layer. Alternative to SC-SWNT/ZnO can be MT-SWNT/ZnO junction which would correspond to vertical Schottky barrier rather than heterojunction type of a photodetector. For practical applications a fast response time is extremely important, so the nature of the interface and bulk states controlling the photocarrier lifetimes needs to be elucidated and optimized by varying the ZnO layer growth technique and conditions, its surface processing, and the SWNT layer transfer during the formation of the heterojunction with an ultimate target to decrease the response time from 10 s to milliseconds range.

3.4 Conclusions

UV photodetector was built on the basis of a semitransparent p-SC-SWNT thin film/n-ZnO vertical heterojunction. The device constitutes a simple planar two-layer structure: after initial MBE growth of ZnO layer the device preparation can be completed

by the solution based SWNT thin film preparation and transfer, so both large and small area devices can be prepared by this technique, and the patterning can be added to prepare an array or modify the geometry of such photodetectors. The novelty and merit of the introduced SC-SWNT/ZnO vertical heterojunction device is in the efficiency of the SC-SWNT layer to enhance the UV performance of ZnO as shown by the comparison with the lateral ZnO device made on the basis of the identical ZnO layer. In this vertical device architecture, the SC-SWNT thin film serves two functions simultaneously, firstly, as a transparent conducting electrode and, secondly, as a semiconducting material forming the heterojunctions thus fully utilizing the multifunctionality of the SWNT thin films. The resulted UV photodetector shows high responsivity up to 400 A/W at wavelength range 370 to 230 nm, and is visible blind with the UV to visible photoresponsivity contrast ratio exceeding 10^5. The detector operates at relatively low reverse bias of 1 to 2 V and shows dark current rectification ratio of 10^3. The p-SC-SWNT/n-ZnO heterojunction is rationalized in terms of the model developed for heterojunction of conventional bulk semiconductors such as p-Ge/n-GaAs.[78-79, 84] Mechanism of photodetection includes efficient separation of photoexcited electron-hole pairs in the strong electric built-in field on the ZnO side of the heterojunction with the involvement of the interface and bulk ZnO intra-gap states trapping and releasing photoexcited carriers thus increasing the photocarrier lifetimes. The presented approach illustrates a synergistic improvement of the UV detector performance when carbon nanomaterials and wide bandgap semiconductors are combined in a single device architecture.

References

(1) Razeghi, M.; Rogalski, A. Semiconductor Ultraviolet Detectors. *J. Appl. phys.* **1996,** *79*, 7433-7473.

(2) Monroy, E.; Calle, F.; Pau, J. L.; Munoz, E.; Omnes, F.; Beaumont, B.; Gibart, P. AlGaN-Based UV Photodetectors. *J. Cryst. Growth* **2001,** *230*, 537-543.

(3) Neele, F.; Schleijpen, R. Electro-Optical Missile Plume Detection. *Proc. of SPIE* **2003,** *5075*, 270-280.

(4) Kamiya, T.; Kawasaki, M. ZnO-Based Semiconductors as Building Blocks for Active Devices. *MRS Bull.* **2008,** *33*, 1061-1066.

(5) Klingshirn, C. ZnO: From Basics Towards Applications. *Phys. Stat. Sol. (b)* **2007,** *244*, 3027-3073.

(6) Zhang, Y.; Ram, M. K.; Stefanakos, E. K.; Goswami, D. Y. Synthesis, Characterization, and Applications of ZnO Nanowires. *J. Nanomater.* **2012,** *2012*, 624520.

(7) Kohan, A. F.; Morgan, D.; Van de Walle, C. G. First-Principles Study of Native Defects in ZnO. *Phys. Rev. B* **2000,** *61*, 15019-15027.

(8) Yang, P.; Yan, H.; Mao, S.; Russo, R.; Johnson, J.; Saykally, R.; Morris, N.; Pham, J.; He, R.; Choi, H. Controlled Growth of ZnO Nanowires and Their Optical Properties. *Adv. Funct. Mater.* **2002,** *12*, 323-331.

(9) Xiu, F.; Yang, Z.; Zhao, D.; Liu, J.; Alim, K. A.; Balandin, A. A.; Itkis, M. E.; Haddon, R. C. ZnO Growth on Si with Low-Temperature ZnO Buffer Layers by ECR-Assisted MBE. *J. Cryst. Growth* **2005,** *286* (1), 61-65.

(10) Xiu, F. X.; Yang, Z.; Mandalapu, L. J.; Zhao, D. T.; Liu, J. L. High-mobility Sb-doped p-type ZnO by Molecular-beam Epitaxy. *App. Phys. Lett.* **2005,** *87*, 152101.

(11) Nie, B.; Hu, J. G.; Luo, L. B.; Xie, C.; Zeng, L. H.; Lv, P.; Li, F. Z.; Jie, J. S.; Feng, M.; Wu, C. Y.; Yu, Y. Q.; Yu, S., H,. Monolayer Graphene Film on ZnO Nanorod Array for High-Performance Schottky Junction Ultraviolet Photodetectors. *Small* **2013,** *9* (19), 2872-2879.

(12) Qi, J.; Gao, D.; Liu, J.; Yang, W.; Wang, Q.; Zhou, J.; Yang, Y.; Liu, J. Magnetic Properties of Er-Doped ZnO Films Prepared by Reactive Magnetron Sputtering. *Appl. Phys. A* **2010,** *100*, 79-82.

(13) Aranovich, J. A.; Golmayo, D.; Fahrenbruch, A. L.; Bube, R. H. Photovoltaic Properties of ZnO/CdTe Heterojunctions Prepared by Spray Pyrolysis. *J. Appl. Phys.* **1980,** *51*, 4260-4268.

(14) D.C, L. Recent Advances in ZnO Materials and Devices. *Mat.Sci. Eng. B* **2001,** *80*, 383-387.

(15) Basak, D.; Amin, G.; Mallik, B.; Paul, G. K.; Sen, S. K. Phtoconductive UV Detectors on Sol-Gel-Synthesized ZnO films. *J. Cryst. Growth* **2003,** *256*, 73-77.

(16) Keem, K.; Kim, H.; Kim, G. T.; Lee, J. S.; Min, B.; Cho, K.; Sung, M. Y.; Kim, S. Photocurrent in ZnO Nanowires Grown from Au Electrodes. *Appl. Phys. Lett.* **2004,** *84*, 4376.

(17) Chu, S.; Lim, J. H.; Mandalapu, L. J.; Yang, Z.; Li, L.; Liu, J. L. Sb-doped p-ZnO/Ga-doped n-ZnO Homojunction Ultraviolet Light Emitting Diodes. *Appl. Phys. Lett.* **2008,** *92*, 152103.

(18) Fan, S. W.; Srivastava, A. K.; Dravid, V. P. UV-Activated Room-Temperature Gas Sensing Mechanism of Polycrystalline ZnO. *Appl. Phys. Lett.* **2009,** *95*, 142106.

(19) Chu, S.; Wang, G.; Zhou, W.; Lin, Y.; Chemyak, L.; Zhao, J. Z.; Kong, J.; Li, L.; Ren, J.; Liu, J. L. Electrically Pumped Waveguide Lasing from ZnO Nanowires. *Nat. Nanotechnol.* **2011,** *6*, 506-510.

(20) Bashar, S.; Suja, M.; Morshed, M.; Gao, F.; Liu, J. L. An Sb-doped p-type ZnO Nanowire Based Random Laser Diode. *Nanotechnology* **2016,** *27*, 065204.

(21) Monroy, E.; Omnès, F.; Calle, F. Wide-Bandgap Semiconductor Ultraviolet Photodetectors. *Semiconductor Science and Technology* **2003,** *18*, R33-R51.

(22) Liu, K.; Sakurai, M.; Aono, M. ZnO-Based Ultraviolet Photodetectors. *Sensors* **2010,** *10*, 8604-8634.

(23) Hou, Y.; Mei, Z.; Du, X. Semiconductor Ultraviolet Photodetectors Based on ZnO and $Mg_xZn_{1-x}O$. *J. Phys. D: Appl. Phys.* **2014,** *47*, 283001.

(24) Brillson, L. J.; Lu, Y. ZnO Schottky Barriers and Ohmic Contacts. *J. Appl. Phys.* **2011,** *109*, 121301.

(25) Allen, M. W.; Alkaisi, M. M.; Durbin, S. M. Metal Schottky Diodes on Zn-polar and O-polar Bulk ZnO. *Appl. Phys. Lett.* **2006,** *89*, 103520.

(26) Han, S.; Zhang, Z.; Zhang, J.; Wang, L.; Zheng, J.; Zhao, H.; Zhang, Y.; Jiang, M.; Wang, S.; Zhao, D.; Shan, C.; Li, B.; Shen, D. Photoconductive Gain in Solar-blind Ultraviolet Photodetector Based on $Mg_{0.52}Zn_{0.48}O$ Thin Film. *Appl.Phys. Lett.* **2011,** *99*, 242105.

(27) Chang, S. P.; Chang, S. J.; Chiou, Y. Z.; Lu, C. Y.; Lin, T. K.; Lin, Y. C.; Kuo, C. F.; Chang, H. M. ZnO Photoconductive Sensors Epitaxially Grown on Sapphire Substrates. *Sens. Actuators, A* **2007,** *140*, 60-64.

(28) Lin, T. K.; Chang, S. J.; Su, Y. K.; Huang, B. R.; Fujita, M.; Horikoshi, Y. ZnO MSM Photodetectors with Ru Contact Electrodes. *J. Cryst. Growth* **2005,** *281*, 513-517.

(29) Mandalapu, L. J.; Xiu, F. X.; Yang, Z.; Zhao, D. T.; Liu, J. L. P-Type Behavior From Sb-Doped ZnO Heterojunction Photodiodes. *Appl. Phys. Lett.* **2006,** *88*, 112108.

(30) Liu, J. L.; Xiu, F. X.; Mandalapu, L. J.; Yang, Z. P-type ZnO by Sb Doping for PN-junction Photodetectors. *Proc. SPIE* **2006,** *6122*, 61220H.

(31) Mandalapu, L. J.; Yang, Z.; Liu, J. L. Low-resistivity Au/Ni Ohmic Contacts to Sb-doped p-type ZnO. *App. Phys. Lett.* **2007,** *90*, 252103.

(32) Jeong, I.-S.; Kim, J. H.; Im, S. Ultraviolet-enhanced Photodiode Employing n-ZnO/p-Si Structure. *Appl. Phys. Lett.* **2003,** *83*, 2946.

(33) Zhang, T. C.; Guo, Y.; Mei, Z. X.; Gu, C. Z.; Du, X. L. Visible-Blind Ultraviolet Photodetector Based on Double Heterojunction of n-ZnO/Insulator-MgO/p-Si. *Appl. Phys. Lett.* **2009,** *94*, 113508.

(34) Hou, Y. N.; Mei, Z. X.; Liang, H. L.; Ye, D. Q.; Liang, S.; Gu, C. Z.; Du, X. L. Comparative Study of n-MgZnO/p-Si Ultraviolet-B Photodetector Performance with Different Device Structures. *Appl. Phys. Lett.* **2011,** *98*, 263501.

(35) Tasi, D. S.; Kang, C. F.; Wang, H. H.; Lin, C. A.; Ke, J. J.; Chu, Y. H.; He, J. H. n-ZnO/$LaAlO_3$/p-Si Heterojunction for Visible-Blind UV Detection. *Opt. Lett.* **2012,** *37*, 1112-1114.

(36) Wu, J. Z. Engineering Heterojunctions with Carbon Nanostructures: Towards High-Performance Optoelectronics. *Proc. SPIE* **2015,** *9553*, 95530Z.

(37) Bo, R.; Nasiri, N.; Chen, H.; Caputo, D.; Fu, L.; Tricoli, A. Low-Voltage High-Performance UV Photodetectors: An Interplay between Grain Boundaries and Debye Length. *ACS Appl. Mater. Interfaces* **2017,** *9*, 2606-2615.

(38) Nasiri, N.; Bo, R.; Fu, L.; Tricoli, A. Three-dimensional Nano-heterojunction Networks: a Highly Performing Structure for Fast Visible-blind UV Photodetectors. *Nanoscale* **2017,** *9*, 2059-2067.

(39) Bai, Z.; Yan, X.; Chen, X.; Cui, Y.; Lin, P.; Shen, Y.; Zhang, Y. Ultraviolet and Visible Photoresponse Properties of a ZnO/Si Heterojunction at Zero Bias. *RSC Adv.* **2013,** *3*, 17682-17688.

(40) Liu, X.; Gu, L.; Zhang, Q.; Wu, J.; Long, Y.; Fan, Z. All-Printable Band-Edge Modulated ZnO Nanowire Photodetectors with Ultra-High Detectivity. *Nat. Commun.* **2014,** *5*, 4007.

(41) Guo, F.; Yang, B.; Yuan, Y.; Xiao, Z.; Dong, Q.; Bi, Y.; Huang, J. A Nanocomposite Ultraviolet Photodetector Based on Interfacial Trap-Controlled Charge Injection. *Nat. Nanotech.* **2012,** *7*, 798-802.

(42) Ates, E. S.; Kucukyildiz, S.; Unalan, H. E. Zinc Oxide Nanowire Photodetectors with Single-Walled Carbon Nanotube Thin-Film Electrodes. *ACS Appl. Mater. Interfaces* **2012,** *4* (10), 5142-5146.

(43) Guo, D. Y.; Shan, C. X.; Qu, S. N.; Shen, D. Z. Highly Sensitive Ultraviolet Photodetectors Fabricated from ZnO Quantum Dots/Carbon Nanodots Hybrid Films. *Sci. Rep.* **2014,** *4*, 7469.

(44) Shao, D.; Sun, H.; Gao, J.; Xin, G.; Aguilar, M. A.; Yao, T.; Koratkar, N.; Lian, J.; Sawyer, S. Flexible, Thorn-like ZnO-multiwalled Carbon Nanotube Hybrid Paper for Efficient Ultraviolet Sensing and Photocatalyst Applications. *Nanoscale* **2014,** *6*, 13630.

(45) Liu, J. S.; Shan, C. X.; Li, B. H.; Zhang, Z. Z.; Yang, C. L.; Shen, D. Z.; Fan, X. W. High Responsivity Ultraviolet Photodetector Realized Via a Carrier-Trapping Process. *Appl. Phys. Lett.* **2010,** *97*, 251102.

(46) Jin, Z.; Q., Z.; Chen, Y.; Mao, P.; Li, H.; Liu, H.; Wang, J.; Li, Y. Graphdiyne: ZnO Nanocomposities for High-Performance UV Photodetectors. *Adv. Mater.* **2016,** *28*, 3697-3702.

(47) Gohier, A.; Dhar, A.; Gorintin, L.; Bondavalli, P.; Bonnassieux, Y.; Cojocaru, C. S. All-Printed Infrared Sensor Based on Multiwalled Carbon Nanotubes *Appl. Phys. Lett.* **2011,** *98* (6), 063103-1-3.

(48) Dresselhaus, M. S.; Dresselhaus, G.; Avouris, P., *Carbon Nanotubes: Synthesis, Structure, Properties and Applications*. Springer-Verlag: Berlin, 2001; Vol. 80.

(49) Wu, Z.; Chen, Z.; Du, X.; Logan, J. M.; Sippel, J.; Nikolou, M.; Kamaras, K.; Reynolds, J. R.; Tanner, D. B.; Hebard, A. F.; Rinzler, A. G. Transparent, Conductive Carbon Nanotube Films. *Science* **2004,** *305*, 1273-1276.

(50) Grüner, G. Carbon Nanotube Films for Transparent and Plastic Electronics. *J. Mater. Chem.* **2006,** *16*, 3533-3539.

(51) Hu, L.; Hecht, D. S.; Grüner, G. Carbon Nanotube Thin Films: Fabrication, Properties, and Applications. *Chem. Rev.* **2010,** *110* (10), 5790-5844.

(52) Arnold, M. S.; Green, A. A.; Hulvat, J. F.; Stupp, S. I.; Hersam, M. C. Sorting Carbon Nanotubes by Electronic Structure Using Density Differentiation. *Nature Nanotech.* **2006,** *1* (1), 60-65.

(53) Wadhwa, P.; Liu, B.; McCarthy, M. A.; Wu, Z.; Rinzler, A. G. Electronic Junction Control in a Nanotube-Semiconductor Schottky Junction Solar Cell. *Nano Lett.* **2010,** *10*, 5001-5005.

(54) Baetens, R.; Jelle, B. P.; Gustavsen, A. Properties, Requirements and Possibilities of Smart Windows for Dynamic Daylight and Solar Energy Control in Buildings: A State-of-the-Art Review. *Sol. Energy Mater. Sol. Cells* **2010,** *94* (2), 87-105.

(55) McCarthy, M. A.; Liu, B.; Donoghue, E. P.; Kravchenko, I.; Kim, D. Y.; So, F.; Rinzler, A. G. Low-Voltage, Low-Power, Organic Light-Emitting Transistors for Active Matrix Displays. *Science* **2011,** *332*, 570-573.

(56) Granqvist, C. G. Electrochromics for Smart Windows: Oxide-based Thin Films and Devices. *Thin Solid Films* **2014,** *564*, 1-38.

(57) Shulaker, M. M.; Hills, G.; Patil, N.; Wei, H.; Chen, H. Y.; Wong, H. S. P.; Mitra, S. Carbon Nanotube Computer. *Nature* **2013,** *501*, 526-530.

(58) Sangwan, V. K.; Ortiz, R. P.; Alaboson, J. M. P.; Emery, J. D.; Bedzyk, M. J.; Lauhon, L. L.; Marks, T. J.; Hersam, M. C. Fundamental Performance Limits of Carbon Nanotube Thin-Film Transistors Achieved Using Hybrid Molecular Dielectrics. *ACS Nano* **2013,** *6*, 7480-7488.

(59) Itkis, M. E.; Borondics, F.; Yu, A.; Haddon, R. C. Bolometric Infrared Photoresponse of Suspended Single-Walled Carbon Nanotube Films. *Science* **2006,** *312*, 413-416.

(60) Lu, R.; Li, Z.; Xu, G.; Wu, J. Z. Suspending Single-Wall Carbon Nanotube Thin Film Infrared Bolometers on Microchannels. *Appl. Phys. Lett.* **2009,** *94*, 163110.

(61) St-Antoine, B. C.; Mènard, D.; Martel, R. Single-Walled Carbon Nanotube Thermopile for Broadband Light Detection. *Nano Lett.* **2011,** *11*, 609-613.

(62) Yanagi, K.; Moriya, R.; Yomogida, Y.; Takenobu, T.; Naitoh, Y.; Ishida, T.; Kataura, H.; Matsuda, K.; Maniwa, Y. Electrochromic Carbon Electrodes: Controllable Visible Color Changes in Metallic Single-Wall Carbon Nanotubes. *Adv. Mater.* **2011,** *23*, 2811-2814.

(63) Wang, F.; Itkis, M. E.; Bekyarova, E.; Haddon, R. C. Charge-Compensated, Semiconducting Single-Walled Carbon Nanotube Thin Film as an Electrically Configurable Optical Medium. *Nat. Photonics* **2013,** *7*, 459-465.

(64) Moser, M. L.; Li, G.; Chen, M.; Bekyarova, E.; Itkis, M. E.; Haddon, R. C. Fast Electrochromic Device Based on Single-Walled Carbon Nanotube Thin Films. *Nano Lett.* **2016,** *19* (9), 5386–5393.

(65) Gu, Q. L.; Ling, C. C.; Chen, X. D.; Cheng, C. K.; Ng, A. M. C.; Beling, C. D.; Fung, S.; Djurišić, A. B.; Lu, L. W.; Brauer, G.; Ong, B. C. Hydrogen Peroxide Treatment Induced Rectifying Behavior of Au/n-ZnO Contact. *Appl. Phys. Lett.* **2007,** *90*, 122101.

(66) Gu, Q. L.; Cheung, C. K.; Ling, C. C.; Ng, A. M. C.; Djurišić, A. B.; Lu, L. W.; Chen, X. D.; Fung, S.; Beling, C. D.; Ong, H. C. Au/n-ZnO Rectifying Contact Fabricated with Hydrogen Peroxide Pretreatment. *J. Appl. Phys.* **2008,** *103*, 093706.

(67) Stekovic, D.; Arkook, B.; Li, G.; Li, W.; Bekyarova, E.; Itkis, M. E. High Modulation Speed, Depth, and Coloration Efficiency of Carbon Nanotube Thin Film Electrochromic Device Achieved by Counter Electrode Impedance Matching. *Adv. Mater. Interfaces* **2018**, 1800861.

(68) Bekyarova, E.; Itkis, M. E.; Cabrera, N.; Zhao, B.; Yu, A.; Gao, J.; Haddon, R. C. Electronic Properties of Single-Walled Carbon Nanotube Networks. *J. Am. Chem. Soc.* **2005,** *127*, 5990-5995.

(69) Mandalapu, L. J.; Xiu, F. X.; Yang, Z.; Liu, J. L. Ultraviolet Photoconductive Detectors Based on Ga-doped ZnO Films Grown by Molecular-beam Epitaxy. *Solid State Elec.* **2007,** *51*, 1014-1017.

(70) Kim, S. H.; Kim, H. K.; Seong, T. Y. Effect of Hydrogen Peroxide Treatment on The Characteristics of Pt Schottky Contact on n-type ZnO. *Appl. Phys. Lett.* **2005,** *86*, 112101.

(71) Young, S. J.; Ji, L. W.; Chang, S. J.; Su, Y. K. ZnO Metal–Semiconductor–Metal Ultraviolet Sensors with Various Contact Electrodes. *J. Cryst. Growth* **2006,** *293*, 43-47.

(72) Bonaccorso, F.; Sun, Z.; Hasan, T.; Ferrari, A. C. Graphene Photonics and Optoelectronics. *Nat. Photonics* **2010,** *4*, 611-622.

(73) Liu, H.; Sun, Q.; Xing, J.; Zheng, Z.; Zhang, Z.; Lu, Z.; Zhao, K. Fast and Enhanced Broadband Photoresponse of a ZnO Nanowire Array/Reduced Graphene Oxide Film

Hybrid Photodetector from the Visible to the Near-Infrared Range. *ACS Appl. Mater. Interfaces* **2015,** *7* (12), 6645-6651.

(74) Gong, X.; Tong, M.; Xia, Y.; Cai, W.; Moon, J. S.; Cao, Y.; Yu, G.; Shieh, C.-L.; Nilsson, B.; Heeger, A. J. High-Detectivity Polymer Photodetectors with Spectral Response from 300 nm to 1450 nm. *Science* **2009,** *325*, 1665-1667.

(75) Henini, M.; Razeghi, M. *Handbook of Infrared Detection Technologies*, Elsevier Advanced Technology: Kidlington, Oxford, UK, 2002.

(76) Nasiri, N.; Bo, R.; F., W.; Fu, L.; Tricoli, A. Ultraporous Electron-Depleted ZnO Nanoparticle Networks for Highly Sensitive Portable Visible-Blind UV Photodetector *Adv. Mater.* **2015,** *27*, 4336-4343.

(77) Shen, Y.; Yan, X.; Si, H.; Lin, P.; Liu, Y.; Sun, Y.; Zhang, Y. Improved Photoresponse Performance of Self-Powered ZnO/Spiro-MeOTAD Heterojunction Ultraviolet Photodetector by Piezo-Phototronic Effect. *ACS Appl. Mater. Interfaces* **2016,** *8*, 6137-6143.

(78) Anderson, R. L. Experiments on Ge-GaAs Heterojunctions. *Solid State Electronics* **1962,** *5*, 341-351.

(79) Lopez, A.; Anderson, R. L. Photocurrent Spectra of Ge-GaAs Heterojunctions. *Solid-State Electron.* **1964,** *7*, 695-700.

(80) Itkis, M. E.; Pekker, A.; Tian, X.; Bekyarova, E.; Haddon, R. C. Networks of Semiconducting SWNTs: Contribution of Midgap Electronic States to the Electrical Transport. *Acc. Chem. Res.* **2015,** *48*, 2270-2279.

(81) Behnam, A.; Johnson, J. L.; Choi, Y.; Ertosun, M. G.; Okyay, A. K.; Kapur, P.; Saraswat, K. C.; Ural, A. Experimental Characterization of Single-walled Carbon Nanotube Film-Si Schottky

Contacts Using Metal-Semiconductor-Metal Structures. *Appl. Phys. Lett.* **2008,** *92*, 243116.

(82) Wang, P. H.; Liu, B.; Shen, Y.; Zheng, Y.; McCarthy, M. A.; Holloway, P.; Rinzler, A. G. N-Channel Carbon Nanotube Enabled Vertical Field Effect Transistors with Solution Deposited ZnO Nanoparticle Based Channel Layers. *Appl. Phys. Lett.* **2012,** *100*, 173514.

(83) Coppa, B. J.; Fulton, C. C.; Kiesel, S. M.; Davis, R. F.; Pandarinath, C.; Burnette, J. E.; Nemanich, R. J.; Smith, D. J. Structural, Microstructural, and Electrical properties of Gold Films and

Schottky Contacts on Remote Plasma-cleaned, n-type ZnO {0001} Surfaces. *J. Appl. Phys.* **2005,** *97*, 103517.

(84) Sze, S. M. *Physics of Semiconductor Devices*, Wiley: New York, 1981.

(85) Brus, L. E. Electron-electron and Electron-hole Interaction in Small Semiconductor Crystallites: The Size Dependence of the Lowest Excited Electronic State. *J. Chem. Phys.* **1984**, 4403-4409.

(86) Marulanda, J. M.; Srivastava, A. Carrier Density and Effective Mass Calculations in Carbon Nanotubes. *Phys. Stat. Sol. (b)* **2007,** *245*, 2558-2562.

(87) Donnelly, J. P.; Milnes, A. G. Current/Voltage Characteristics of p-n Ge-GaAs Heterojunctions. *Proc. IEEE* **1966,** *113*, 1468-1476.

(88) Joshi, N. V. *Photoconductivity: Art, Science, and Technology*, Marcel Dekker, Inc.: New York: NY, NY, 1990; Vol. 25, p 309.

(89) Spataru, C. D.; Ismail-Beigi, S.; Benedict, L. X.; Louie, S. G. Excitonic Effects and Optical Spectra of Single-Walled Carbon Nanotubes. *Phys. Rev. Lett.* **2004,** *92* (7), 077402.

(90) Wang, F.; Dukovic, G.; Knoesel, E.; Brus, L.; Heinz, T. Observation of Rapid Auger Recombination in Optically Excited Semiconducting Carbon Nanotubes. *Phys. Rev. B: Condens. Matter Mater. Phys.* **2004,** *70*, 241403.

(91) Sheng, C.-X.; Vardeny, Z. V.; Dalton, A. B.; Baughman, R. H. Exciton Dynamics in Single-Walled Nanotubes: Transient Photoinduced Dichroism and Polarized Emission. *Phys. Rev. B: Condens. Matter Mater. Phys.* **2005,** *71*, 125427.

(92) Wang, F.; Dukovic, G.; Brus, L. E.; Heinz, T. The Optical Resonances in Carbon Nanotubes Arise from Excitons. *Science* **2005,** *308*, 838-841.

Chapter 4 Applications of MoS_2 Optoelectronic Properties for NO_2 Gas Sensor Detection at Sub-ppb Level

4.1 Introduction

In this Chapter we introduce a novel electro-optical gas sensor based on 2-dimensional transition metal dichalcogenide MoS_2 which can detect one of the most dangerous pollutants nitrogen dioxide at sub-ppb level. This work was done in collaboration with Professor Mulchandani research group, and Graduate student Tung Pham prepared MoS_2 devices. The part of this project presented in my Thesis is related to application of electro-optical properties of MoS_2 for gas sensing.

Nitrogen dioxide (NO_2) is a very dangerous gas which is produced by the burning of fuels, emissions from vehicles, power plants, and road-off equipment.[1] In the ambient air, NO_2 will react with water to form acid rain, resulting in the damage of buildings, ecosystem destruction, and nutrient pollution in coastal water. Moreover, NO_2 is highly toxic to humans and animals, especially to skin, eyes, and respiratory system.[2] The United States Environmental Protection Agency (US EPA) has regulated limit of exposure to NO_2 at 53 ppb averaged annually, and 100 ppb averaged over one hour.[3] Therefore, it is quite urgent and necessary to develop NO_2 gas sensors with high sensitivity achieving ppb level.

Up to now, much effort has been devoted to develop NO_2 sensor with high sensitivity, low detection limit, and low working temperature. Metal oxides like Cu_2O, WO_3, SnO_2, and NiO are good candidates for NO_2 detection, but limited by the high working temperature, high detection limit, and poor selectivity.[4-7] One-dimension SWNTs have

unique structure, large surface area, and outstanding electrical properties, so they are viewed as promising materials for chemical sensors. Hongjie Dai group prepared chemical sensors based on individual SWNT for NO_2 and NH_3 gas detection.[8] The SWNT based sensor shows fast response to NO_2 but slow recovery at room temperature. Two-dimensional single-layer graphene is composed of 1-layer of carbon atoms which has large surface area (2630 m^2 g^{-1}), and every carbon atom is in contact with gas molecules. Moreover, graphene can absorb molecules via van der Waals interaction and strong covalent bonding. Therefore, graphene has attracted a great deal of interest to explore it potential applications in chemical sensors.[9] Pearce, et al. epitaxially grew single-layer graphene on SiC substrate for NO_2 detection. At room temperature, the sensor is capable to detect 2.5 ppm of NO_2 but shows slow response and recovery.[10] Despite of significant efforts to develop chemical sensors based on SWNTs and graphene, there is a long way to go to overcome some drawbacks like slow recovery and poor selectivity.

Following the discovery of graphene,[11] other two dimensional (2D) materials such as transition metal dichalcogenides (TMDs) attracted significant attention because of the unique electronic properties originated from their low-dimensional electronic structure.[12-16] In contrast to graphene, TMDs possess finite bandgap in the range from 0.2 to 3 eV, depending on specific type of material and a number of layers, and became a valuable alternative to the conventional or narrow band semiconductors in a variety of electronic and optoelectronic applications (Figure 4.1).[12-17] [18]

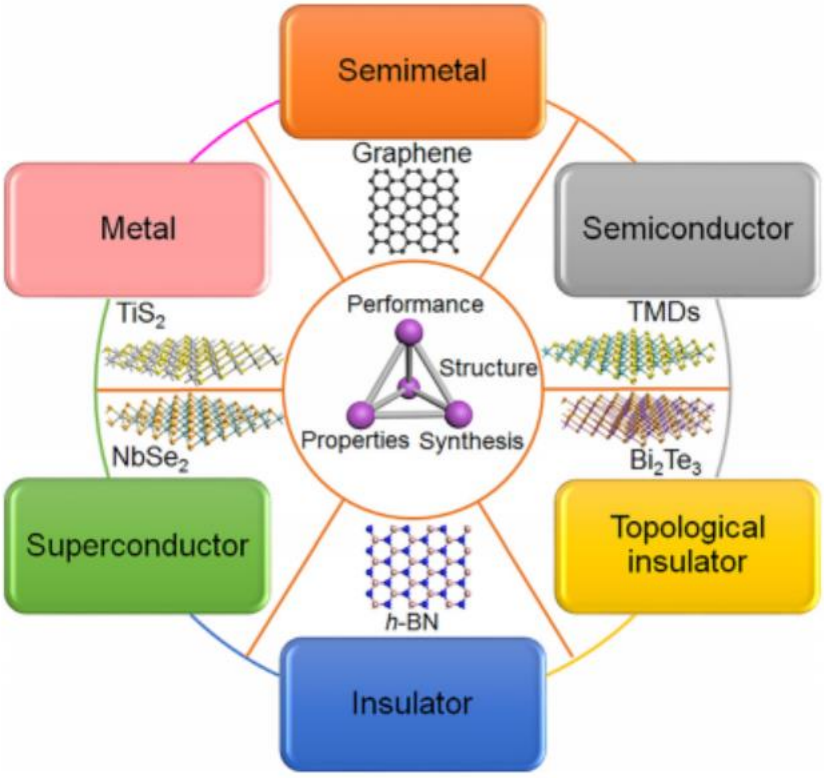

Figure 4.1 2D material and tetrahedron.[18]

MoS_2 is one of the most prominent materials from TMD family possessing a direct bandgap of 1.8 eV as a single layer[19-20] and showing promising performance in field-effect transistors (FETs), p-n junctions and heterojunctions, photovoltaic cells, and photodetectors demonstrations.[21-26] Monolayer MoS_2 consists of two layers of sulfur atoms in two-dimensional hexagonal planes connecting with Mo atoms through ionic-covalent bonding. Each Mo atom is surrounded by six sulfur atoms as shown in Figure 4.2[27]

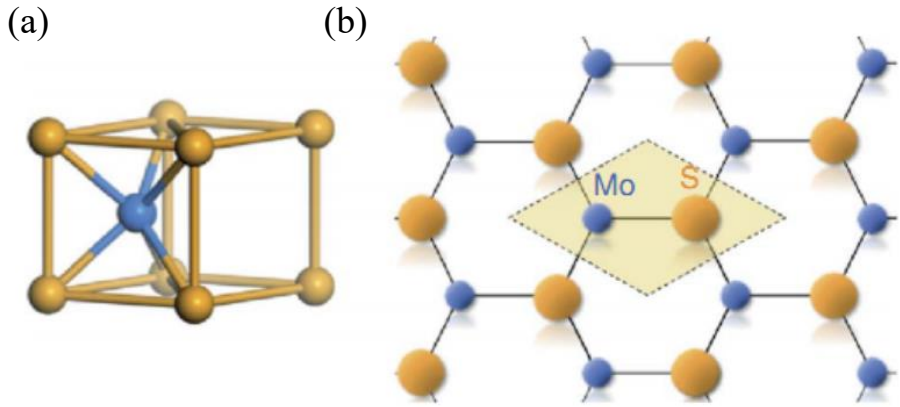

Figure 4.2 (a) Coordination environment of Mo atom in the structure; (b) a top view of the monolayer MoS_2 lattice.[27]

From the theoretical calculations, bulk MoS_2 is an indirect bandgap semiconductor and becomes a direct bandgap semiconductor when thinned to monolayer.[28] As shown in Figure 4.3, the direct excitonic transition energy at the Brillouin zone *K*-point has little change with the increase of the number of layers, while the indirect bandgap increases as the number of layers increases.[28] As a result, the monolayer MoS_2 is a direct bandgap semiconductor.

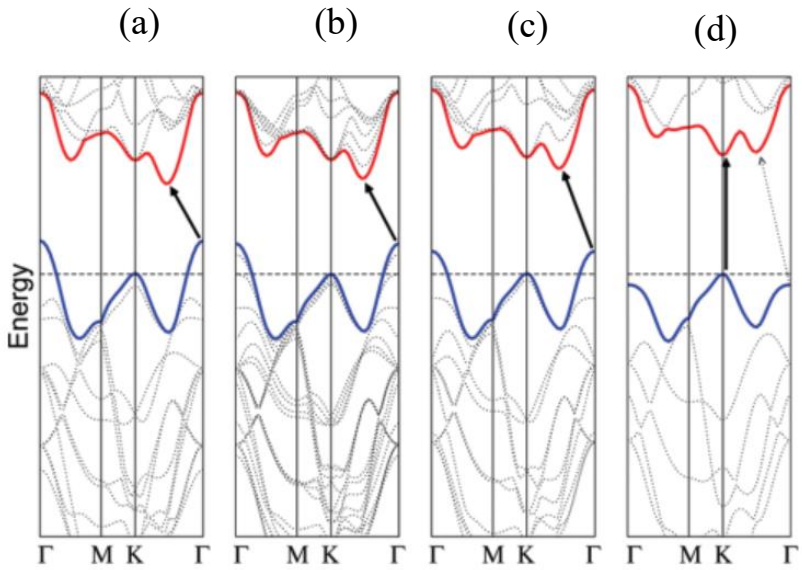

Figure 4.3 Calculated band structures of (a) bulk MoS_2, (b) quadrilayer MoS_2, (c) bilayer MoS_2, and (d) monolayer MoS_2.[28]

This change in the bandgap structure is due to the quantum confinement and the change in electron orbitals. Briefly, the conduction band states at *K*-point are primarily composed of localized *d* orbitals of Mo atom located at the middle of the S-Mo-S, which are barely affected by interlayer coupling. However, the states near the *Γ*- points are originated from the d orbitals of Mo atoms and the antibonding p_z-orbitals of S atoms which are very sensitive to the number of layers because of the strong interlayer coupling. Therefore, the band structures heavily depend on the number of layers of MoS_2.[12, 28]

As MoS_2 shows unique electronic properties and has great potential applications in multiple fields, various techniques have been explored to prepare reliable, large-scale, and atomically thin MoS_2 films. Like single-layer graphene, monolayer MoS_2 flake can

be exfoliated by micromechanical cleavage using adhesive tape. The obtained monolayer MoS_2 flake shows high cleanliness and quality with very few defects, and it is suitable for individual device fabrication and characterization in the lab. However, this method is limited to small-scale production and small size.[29-30] Solution intercalation is a promising method to produce large scale of high quality monolayer MoS_2. During the exfoliation process, it will produce MoS_2 with different phases, showing different electronic structures like semiconductors or metals. This issue can be resolved by annealing the sample at 300 ºC, resulting in change from metallic to semiconducting type of MoS_2.[31-32] Chemical vapor deposition (CVD) is an alternative method to achieve wafer-scale synthesis of MoS_2 thin film with high quality and few defects, which enables MoS_2 applications in wafer-scale fabrication of electronic devices.[33]

Because of their high surface to volume ratio, electronic transport in atomically thin TMD channels is extremely sensitive to the surrounding atmosphere thus allowing their exploration in gas and bio-sensing applications.[34-40] TMDs is now considered as a promising alternative to the conventional metal oxides sensing materials[2, 41-43] which typically require elevated temperature operations causing excessive energy consumption, reliability issues, and, especially, safety concerns. Chemiresistors based on single-and multi-layer MoS_2, either mechanically exfoliated or CVD grown, have been already explored for sensing of such hazardous analytes as NO, NH_3, Volatile Organic Compounds (VOCs) and nerve agents at ppm level. [34-40]

In recent years, several studies demonstrated efficient MoS_2 based NO_2 sensors performances at ppm level.[38-39, 44] It has been reported recently that CVD grown MoS_2

FET-based gas sensor is capable for NO_2 detection at sub-ppm (200 ppb) level, [38] however, a poor recovery at room temperature and slow response have been observed. Later reports show improved recovery by utilization of elevated temperatures ranging from 100 ºC to 150 ºC due to accelerated desorption of the gas molecules.[45-46] As an alternative strategy, UV light irradiation of the MoS_2 channel was employed to improve sensitivity and recovery rate of the response to NO_2 exposure[44] at ppm level following the strategy developed earlier for metal oxide based sensors.[47-48] In that report,[44] UV light is used as a tool to release oxygen ions from MoS_2 surface thus facilitating the interaction of NO_2 molecules with conducting electrons in MoS_2 channel and yielding faster removal rate of NO_2 molecules after the exposure.

CVD grown single layer MoS_2 is an ultimate 2D material with highest possible surface-to-volume ratio as compared to few layer alternatives, and is more suited for semiconducting processing platform as compared to mechanically exfoliated MoS_2 counter-part. However, due to several factors such as large bandgap of MoS_2, grain boundaries of MoS_2 triangular crystals forming its single-layer structure, and contribution of Schottky barriers at metal-MoS_2 contact interfaces, the typical sensor resistance can reach extremely high values of 10 GΩ to 1 TΩ. This complicates the sensor electrical integration with readout circuit and increases electrical noise thus degrading the sensor performance in terms of limit of detection of gaseous analytes.

Here, we utilize LED illumination with photon energy matching the bandgap of single-layer MoS_2 in order to decrease the MoS_2 channel resistance by 3 orders of magnitude by inducing a photocurrent, and employ the generated photocurrent instead of

dark current for NO_2 gas sensing. As a result, an efficient response to sub-ppm level of NO_2 concentrations (25 to 200 ppb) exposure was demonstrated with a sensitivity of 4.9%/ppb (4900%/ppm). Calculations of the optimized chemi-photoresistor limit of detection (*LOD*) following IUPAC procedure,[49] provided an evaluation of *LOD* for NO_2 detection at the level of ~0.2 ppb which exceeds the US Environment Protection Energy requirement of NO_2 detection at ppb level.

4.2 Experimental Section

1. MoS_2 growth and device preparation.

Single-layer MoS_2 films were grown by graduate student Tung Pham (Professor Mulchandani research group) via a CVD method, and Tung Pham also prepared the MoS2 device. After transferring MoS_2 to the desired SiO_2 substrate, 5 nm/ 50 nm thick Gr/Au electrodes are prepared using standard photolithography procedures and electron-beam metal deposition. The size of the active MoS_2 channel is $10\times10\mu$m

2. Electrical and photoconductivity measurements

The current-voltage (I-V) measurements in dark and under the light were conducted utilizing a Keithley 236 source-measure unit. The instruments control and data acquisition for all the measurements were conducted utilizing Labview hardware and software. For photoconductivity and gas sensing measurements the red LED (model L10762, Hamamatsu Photonics) with the central wavelength of 660 nm was integrated with the gas sensing mini-chamber. The LED power density was modulated utilizing a function generator DS360 (Stanford Research Systems), and the light intensity on the device was calibrated by Silicon based photodetector. The frequency dependencies of the

photoresponse were studied using a lock-in amplifier (SRS 830, Stanford Research Systems) with the dc bias of 5 V supplied by Keithley 236 source-measure unit, and the load resistance of 100 kΩ.

3. NO_2 sensing experiments

For gas sensing experiments, the concentrations of NO_2 gas is regulated by two Alicat Scientific mass flow controllers: one controlling the flow of 99.99% pure N_2 gas and the other controlling the flow of 10 ppm NO_2 in N_2. The target NO_2 concentration for detection of 25 ppb, 50 ppb, 100 pbb, 150 ppb, 200 ppb are achieved by mixing NO_2 flow with N_2 flow at ratios of 1:399, 2:398, 4:396, 6:394 and 8:392, respectively while the total flowrate to the sensing chamber remains constant at 400 sccm.

4.3 Results and Discussions

Figure 4.4a shows a schematic of MoS_2 channel with Cr/Au electrodes denoted in this paper as MoS_2(Au) device. I-V curve in dark (Figure 4.4b) shows very low current in pico-amperes range corresponding to the very high channel resistance of ~200 GΩ. Under red LED illumination of 60.9 nW (light intensity of 60.9 mW/cm^2) the channel current increases by ~500 times exceeding 10 nA at 5 V channel bias (Figure 4.4c). The temporal evolution of the photocurrent when LED irradiation is switching "on" and "off" is presented in Figure 4.4d showing relatively fast rise of photocurrent when LED irradiation is switching on with ~80% level reached in less than 1 s following by slow increase of photocurrent which continues for hundreds of seconds. Similar shape can be observed in the decay of photocurrent when LED is turned off with initial fast decay to below 10% level in less than 1 s followed by slow decay.

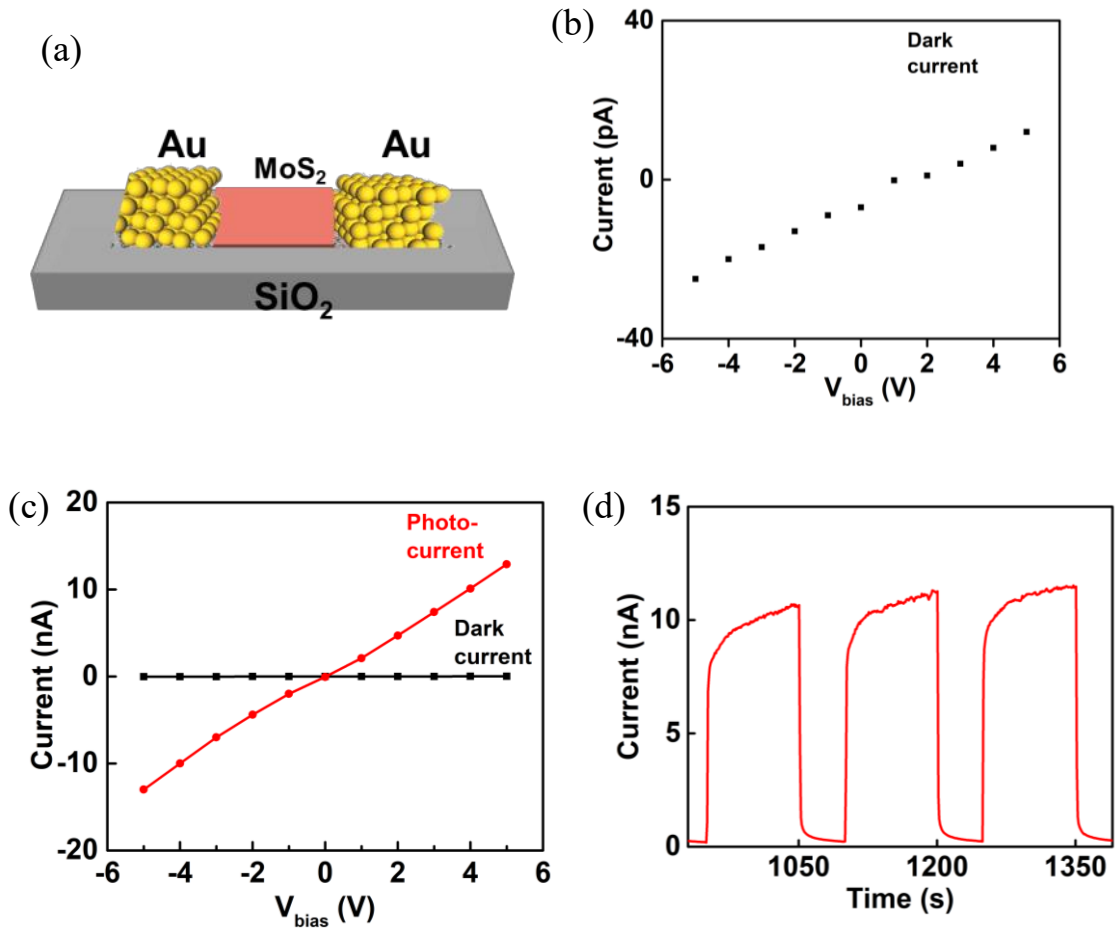

Figure 4.4 (a) Schematic of MoS_2 channel with Au electrodes; I-V dependence of MoS_2(Au) device (b) in dark (c) under red LED illumination of incident power of 60.9 nW; (d) photocurrent pulses as a response to switching of red LED irradiation "on" and "off".

The dependences of the amplitude of the photocurrent of the MoS_2 devices on the frequency f of square-wave red LED light modulation are presented in Figure 4.5a and show a decrease of photocurrent with increasing frequency described by power law $I_{ph} \propto f^{-\alpha}$ with best fitting obtained using exponents α of 0.17 for the devices with Au

electrodes. Such type of power law dependence of photocurrent with exponent α <1 are well known in the field of classical photoconductors, and is usually associated with wide distribution of photocarrier lifetimes (in our case from milliseconds to tens of seconds) due to the presence of trap states.[24, 50-53] Figure 4.5b shows that the dependence of photocurrent on the incident irradiation power P deviates from direct proportionality and is best described by the power law $I_{ph} \propto P^{\beta}$, with the exponents β values less than unity of 0.63 for the devices with Au electrodes. Such β <1 values are also typically associated with the presence of trap states distributed in energy within the bandgap of the conventional photoconductors.[50] In case of 2D materials with high surface to volume ratio the effect of trap states on the photoconductivity is often described in terms of photogating when under illumination one type of photocarriers is trapped by lattice defects or impurities.[52-53] Such trapping leads to the spatial charge accumulation and induced electric field which acts as a gate voltage in conventional FETs shifting the Fermi level of 2D channel to the energy position dependent on the time and intensity of incident radiation.[24, 50, 52-53] The contribution of photogating can explain the presented in Figure 4.5 power law dependences of photocurrent on frequency and incident power with exponents α and β less than unity. In case of single layer MoS_2 channel utilized in this study the trap states can be formed at the interface of MoS_2 and supporting dielectric (SiO_2) layer or on the top of MoS_2 layer. The fast photoresponse component visible at the moment of LED switching "on" and "off" and at high frequencies of modulation can be attributed to direct photoconductivity while slow component of photoresponse can be

associated with photogating, however, the boundary between these two contributions can be not well defined.

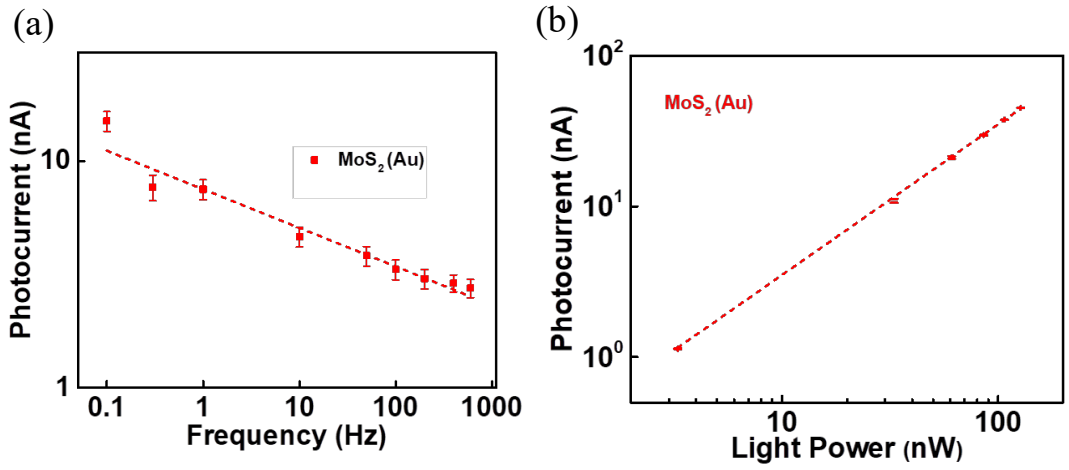

Figure 4.5 Dependence of photocurrent on (a) frequency of red LED modulation and (b) power of red LED irradiation for MoS_2 devices with 3 types of electrodes. Dashed lines show power law fits of experimental dependences as described in the text.

Figure 4.6 compares typical responses of MoS_2 single-layer based gas sensor with Cr/Au electrodes to NO_2 gas exposure in dark and under red LED illumination of incident power of 60.9 nW (light intensity of 60.9 mW/cm^2). For better comparison dark and photo- currents in Figure 4.6a and 4.6b, respectively, are both presented in logarithmic scale with the same maximum to minimum current ratios of 200. As presented in Figures 4.6a the current in the dark is very low in 20 to 30 pA range, but some visible decrease of the current upon NO_2 exposure can be observed at low NO_2 concentration of 50 ppb thus supporting previously demonstrated high potential of MoS_2 monolayer material for chemical sensor application.[34-35, 39, 54] Figure 4.6b shows that under LED illumination the current through the MoS_2 channel increases by 3 orders of magnitude and, more

strikingly, illuminated sensor shows much stronger response to the lowest reliably controlled concentration of NO_2 of 25 ppb which is a limit of our present setup.

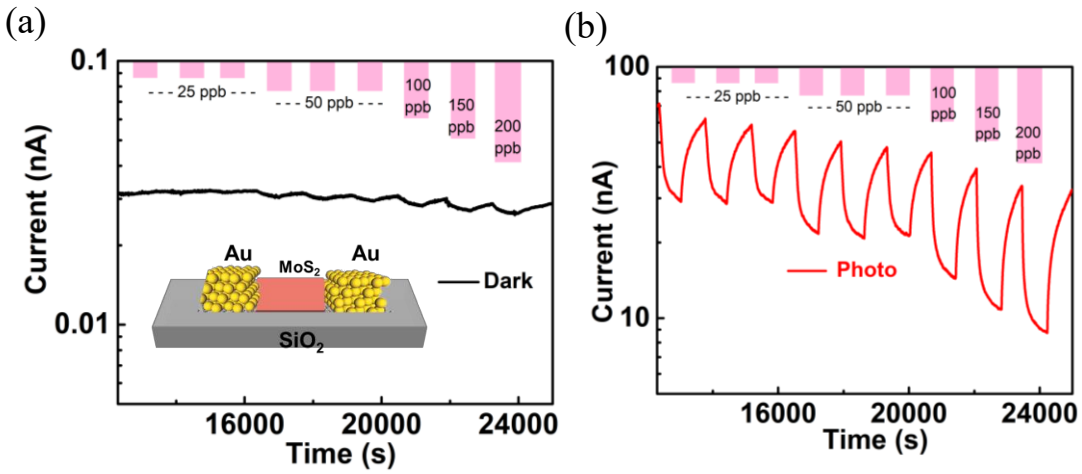

Figure 4.6 Effect of NO_2 gas exposure at concentrations from 25 to 200 ppb on: (a) Dark current in MoS_2(Au) device; (b) Photocurrent in MoS_2(Au) device under red LED illumination of incident power of 60.9 nW (light intensity of 60.9 mW/cm^2).

Figure 4.7a shows NO_2 detection results in terms of relative change of resistance $\Delta R/R_{N2}$, where R_{N2} is the resistance of the device established under N_2 flow before NO_2 exposure in dark or under illumination, and ΔR is a resistance change caused by NO_2 exposure. Noticeably, the response to NO_2 exposure under illumination is enhanced dramatically even if compared to dark current data expanded by a factor of 5. Figure 4.7b presents the amplitude of relative response $\Delta R/R_{N2}$ in dark and under illumination as a function of NO_2 concentration C (ppb) with a slope of such dependence defining the device sensitivity $S=\Delta R/R_{N2}(\%)/C(ppb)$. Under red LED illumination the NO_2 sensitivity is extremely high at the level of S=4.9%/ppb (4900%/ppm), much higher than the best

values at the level of 0.1%/ppb obtained in the dark. Some of the tested MoS_2(Au) sensors didn't show any response in the dark to sub-ppm concentrations of NO_2, while the sensitivity under red LED light illumination was consistently high. We should note that the sensitivity is usually normalized to the concentration expressed in ppm units but in our work we report a concentration in %/ppb units due to the strong response of our sensor to ppb level concentration of NO_2.

Another important figure of merit of chemical sensor is limit of detection (*LOD*) of the particular analyte which, following IUPAC procedure, is typically defined as a concentration of the analyte which causes a response 3 times higher than the noise level of the device (i.e. in the absence of the analyte).[49, 55] From the noise data presented in Figure 4.7b (inset) for the illuminated sensor root-mean-square (RMS) value of $\Delta R/R_{N2}$ noise of ~ 0.32% is obtained giving an evaluation of *LOD* of 3x0.32/4.9 ≈ 0.2 ppb. For comparison, the noise level for the sensor in dark is ~0.6% with much lower sensitivity of 0.1%/ppb resulting in detection limit of 3x0.6/0.1≈18 ppb in agreement with the visual observation of data presented in Figure 7. Thus bandgap matching illumination of MoS_2 sensor induces photocurrent in the sensor channel which can be used to significantly improve the sensitivity and detection limit of NO_2 sensing.

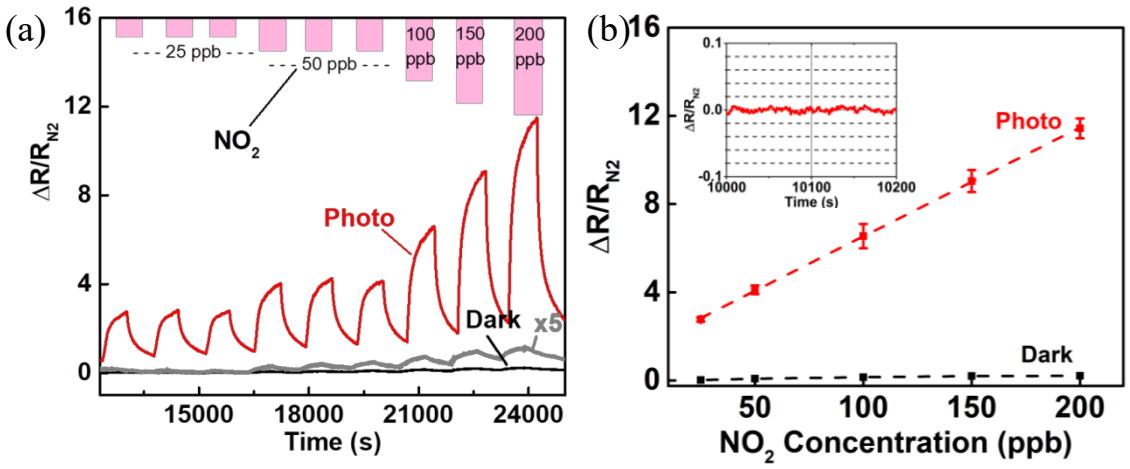

Figure 4.7 (a) Normalized resistance of MoS_2(Au) device in dark (black line, gray line shows x5 expanded data) and under red light (red curve). (b) Dependence of the normalized amplitude of resistance change $\Delta R/R_{N2}$ on the concentration of NO_2 gas. Inset shows a temporal trace of experimentally recorded noise of $\Delta R/R_{N2}$. All data were collected under dc bias of 5 V.

The band diagram of the MoS_2 channel in dark is presented in Figure 4.8a with Fermi level shifted towards conduction band for typically n-type doped MoS_2. Because of the relatively large band gap of MoS_2 and high Schottky barriers at the metal electrode/MoS_2 interfaces the concentration of free carriers is very low with thermally excited electrons and holes acting as majority and minority carriers, respectively. The relatively low sensitivity of the sensor in dark can be explained by the presence of oxygen which traps the thermally excited electrons in MoS_2 channel leading to further reduction of the device current. Thus, most of electrons are blocked by oxygen from interaction with NO_2 molecules resulting in suppressed response to the analyte. As schematically illustrated in Figure 4.8 b, under red light illumination the population of free electrons increases by

several orders of magnitude. Part of this increase can be due to photogating[52-53] when photoexcited holes are trapped at the MoS_2/SiO_2 interface generating a spatial positive charge which shifts the Fermi level closer to the edge of conduction band and increasing a population of the thermally excited electrons. These extra electrons are not blocked by oxygen and available for interaction with NO_2 molecules because of the single layer structure of MoS_2 when any charge carrier is at the surface. As discussed in literature, NO_2 gas molecules absorbed on MoS_2 channel surface act as electron acceptors and capture the photoexcited electrons thus leading to a decrease of current (photocurrent) in the channel.[35, 44]

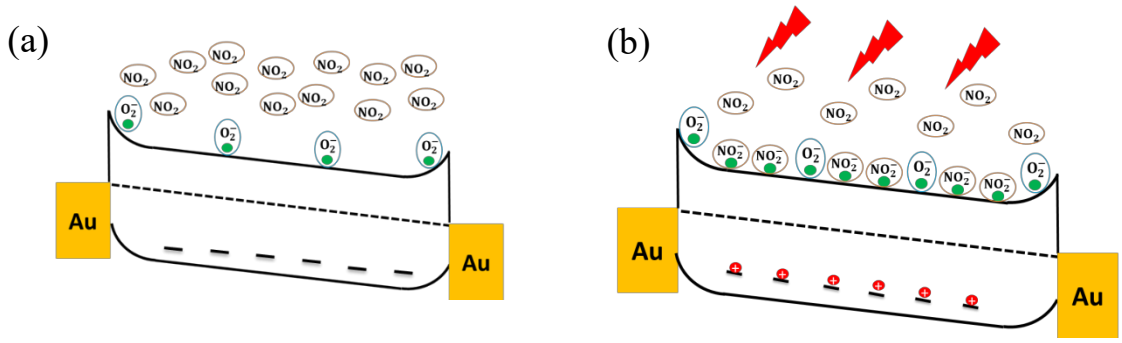

Figure 4.8 Band diagram of the device showing interaction of conduction band electrons in MoS_2 with NO_2 gas molecules (a) in dark and (b) under red light illumination.

Table 4.1 summarizes state of the art parameters reported in literature for MoS_2 based NO_2 gas sensors. Presented in this work MoS_2 operating under red LED light illumination shows the highest reported sensitivity to low dosage of NO_2 gas, because the photocurrent is used to enhance the sensor response. The calculations following IUPAC defined procedure gave extremely low detection limit in sub-ppb range (0.2 ppb) well suited to US EPA needs for NO_2 sensing at ppb level.

Table 4.1 Comparison between reports on MoS_2 based NO_2 gas sensors and present work

Material	Temperature	Minimum concentration tested	Detection limit (Calculation)	Sensitivity %/ppm	Ref.
MoS_2	RT	100 ppm	50-100 ppm	1.37/ppm	16
MoS_2	RT	20 ppb	10-20 ppb		17
MoS_2	RT	120 ppb	50-120 ppb	416/ppm	19
Gr/MoS_2	150 ^oC	1.2ppm	1.2 ppm	2.5/ppm	20
MoS_2/Gr	200 ^oC	50 ppb	14 ppb	18/ppm	30
3D MoS_2	200 ^oC	50 ppb	28ppb	20/ppm	31
MoS_2	RT (UV)	5 ppm	1-5 ppm	3.05/ppm	29
MoS_2	100	5 ppm	1-5 ppm	2.4/ppm	29
PtNPs/MoS_2	RT	0.5 ppm	2 ppb	8/ppm	35
MoS_2	RT	300ppb	200-300 ppb	0.08/ppm	36
MoS_2	100 ^oC	25	2 ppb		56
MoS_2	RT (red light)	25 ppb	0.2ppb	4.9/ppb (4900/ppm)	This work

4.4 Conclusions

Red light LED illumination with photon energy matching the direct bandgap of the single layer MoS_2 allowed to use induced photocurrent instead of dark current as a tool for NO_2 gas sensing. The resulted sensor showed extremely high sensitivity to ppb level NO_2 gas exposure up to 4.9 %/ppb (4900 %/ppm) and sub-ppb limit of NO_2 gas detection at the 0.2 ppb level. The presented concept of enhancing gas sensing performance by inducing a photocurrent can be expanded on different analytes, and employ other 2D TMD materials by matching the photon energies to the specific bandgaps.

References

(1) Atkinson, R. Atmospheric Chemistry of VOCs and NO_x. *Atmos. Environ.* 2000, *34*, 2063-2101.

(2) Wetchakun, K.; Samerjai, T.; Tamura, N.; Liewhiran, C.; Siriwong, C.; Kruefu, V.; Wisitsoraat, A.; Tuantranont, A.; Phanichphant, S. Semiconducting Metal Oxides as Sensors for Environmentally Hazardous Gases. *Sens. Actuators B: Chem.* 2011, *160*, 580-591.

(3) U. S. Environmental Protection Agency, "Air Trends Summary Report": http://www.epa.gov/oar/aqtrnd95/no2.html.

(4) Deng, S.; Tjoa, V.; Fan, H. M.; Tan, H. R.; Sayle, D. C.; Olivo, M.; Mhaisalkar, S.; Wei, J.; Sow, C. H. Reduced Graphene Oxide Conjugate Cu_2O Nanowire Mesocrystals for High-Performance NO_2 Gas Sensor. *J. Am. Chem. Soc.* 2012, *134*, 4905-4917.

(5) Cantalini, C.; Sun, H. T.; Faccio, M.; Pelino, M.; Santucci, S.; Lozzi, L.; Passacantando, M. NO_2 Sensitivity of WO_3 Thin Film Obatained by High Vacuum Thermal Evaopration *Sens. Actuat. B* 1996, *31*, 81-87.

(6) Law, M.; Kind, H.; Messer, B.; Kim, F.; Yang, P. Photochemical Sensing of NO_2 with SnO_2 Nanoribbon Nanosensors at Room Temperature. *Angew. Chem. Int. Ed.* 2002, *41*, 2405-2408.

(7) Hotovy, I.; Rehacek, V.; Siciliano, P.; Capone, S.; Spiess, L. Sensing Characteristics of NiO Thin Films as NO_2 Gas Sensor. *Thin Solid Films* 2002, *418*, 9-15.

(8) Kong, J.; Franklin, N. R.; Zhou, C.; Chapline, M. G.; Peng, S.; Cho, K.; Dai, H. Nanotube Molecular Wires as Chemical Sensors. *Science* 2000, *287*, 622-625.

(9) Yuan, W.; Shi, G. Graphene-Based Gas Sensor. *J. Mater. Chem. A* 2013, *1*, 10078-10091.

(10) Pearce, R.; Iakimov, T.; Andersson, M.; Hultman, L.; Spetz, A. L.; Yakimova, R. Epitaxially Grown Graphene Based on Gas Sensors for Ultra Sensitive NO_2 Detection. *Sens. Actuat. B* 2011, *155*, 451-455.

(11) Novoselov, K. S.; Geim, A. K.; Morozov, S. V.; Jiang, D.; Zhang, Y.; Dubonos, S. V.; Grigorieva, I. V.; Firsov, A. A. Electric Field Effect in Atomically Thin Carbon Films. *Science* 2004, *306*, 666-669.

(12) Wang, H.; Kalantar-Zadeh, K.; Kis, A.; Coleman, Y. N.; Strano, M. S. Electronics and Optoelectronics of Two-dimensional Transition Metal Dichalcogenides. *Nat. Nanotech.* 2012, *7*, 699-712.

(13) Geim, A. K.; Grigorieva, I. V. Van der Waals Heterostructures. *Nature* 2013, *499*, 419-425.

(14) Xu, M.; Liang, T.; Shi, M.; Chen, H. Graphene-Like Two-Dimensional Materials. *Chem. Rev.* 2013, *113*, 3766-3798.

(15) Jariwala, D.; Sangwan, V. K.; Lauhon, L. J.; Marks, T. J.; Hersam, M. C. Emerging Device Applications for Semiconducting Two-Dimensional Transition Metal Dichalcogenides. *ACS Nano* 2014, *8*, 1102-1120.

(16) Tan, C.; Cao, X.; Wu, X. J.; He, Q.; Yang, J.; Zhang, X.; Chen, J.; Zhao, W.; Han, S.; Nam, G. H.; Sindoro, M.; Zhang, H. Recent Advances in Ultrathin Two-Dimensional Nanomaterials. *Chem. Rev.* 2017, *117*, 6225-6331.

(17) Sun, Z.; Martinez, A.; Wang, F. Optical Modulators with 2D Layered Materials. *Nat. Photon.* 2016, *10*, 227-238.

(18) Li, X.; Tao, L.; Chen, Z.; Fang, H.; Li, X.; Wang, X.; Xu, J. B.; Zhu, H. Graphene and Related Two-Dimensional Material: Structure-Property Relationships for Electronics and Optoelectronics. *Appl. Phys. Rev.* 2017, *4*, 021306-.

(19) Mak, K. F.; Lee, C.; Hone, J.; Shan, J.; Heinz, T. F. Atomicall Thin MoS_2: A New Direct-Gap Semiconductor. *Phys. Rev. Lett.* 2010, *105*, 136805.

(20) Lee, C.; Yan, H.; Brus, L. E.; Heinz, T. F.; Hone, J.; Ryu, S. Anomalous Lattice Vibrations of Single- and Few-Layer MoS_2. *ACS Nano* 2010, *4*, 2695-2700.

(21) Radisavljeic, B.; Radenovic, A.; Brivio, J.; Giacometti, V.; Kis, A. Single-Layer MoS_2 Transistors. *Nat. Nanotech.* 2011, *6*, 147-150.

(22) Choi, M. S.; Qu, D.; Lee, D.; Liu, X.; Watanabe, K.; Taniguchi, T.; Yoo, W. J. Lateral MoS_2 p-n Junction Formed by Chemical Doping for Use in High-Performance Optoelectronics. *ACS Nano* 2014, *8*, 9331-9340.

(23) Wi, S.; Kim, H.; Chen, M.; Nam, H.; Guo, L. J.; Meyhofer, E.; Liang, X. Enhancement of Photovoltaic Response in Multilayer MoS_2 Induced by Plasma Doping. *ACS Nano* 2014, *6*, 5270-5281.

(24) Lopez-Sanchez, O.; Lembke, D.; Kayci, M.; Radenovic, A.; Kis, A. Ultrasensitive Photodetectors Based on Monolayer MoS_2. *Nat. Nanotech.* 2013, *8*, 497-501.

(25) Zhang, W.; Huang, J. K.; Chen, C. H.; Chang, H. Y.; Cheng, Y. J.; Li, L. J. High-Gain Phototransistors Based on a CVD MoS_2 Monolayer. *Adv. Mater.* 2013, *25*, 3456-3461.

(26) Yin, Z.; Li, H.; Li, H.; Jiang, L.; Shi, Y.; Sun, Y.; Lu, G.; Zhang, Q.; Chen, X.; Zhang, H. Single-Layer MoS_2 Phototransistors. *ACS Nano* 2012, *6*, 74-80.

(27) Cao, T.; Wang, G.; Han, W.; Ye, H.; Zhu, C.; Shi, J.; Niu, Q.; Tan, P.; Wang, E.; Liu, B.; Feng, J. Valley-Selective Circular Dichroism of Monolayer Molybdenum Disulphide. *Nature Commun.* 2012, *3*, 887.

(28) Splendiani, A.; Sun, L.; Zhang, Y.; Li, T.; Kim, J.; Chim, C. Y.; Galli, G.; Wang, F. Emerging Photoluminescence in Monolayer MoS_2. *Nano Lett.* 2010, *10*, 1271-1275.

(29) Lee, C.; Yan, H.; Brus, L. E.; Heinz, T. F.; Hone, J.; Ryu, S. Anomalous Lattice Vibrations of Single- and Few-Layer MoS_2. *ACS Nano* 2010, *4*, 2695-2700.

(30) Mak, K. F.; Lee, C.; Hone, J.; Heinz, T. F. Atomically Thin MoS_2: a New Direct-Gap Semiconductor. *Phys. Rev. Lett.* 2010, *105*, 136805.

(31) Eda, G.; Yamaguchi, H.; Voiry, D.; Fujita, T.; Chen, M.; Chhowalla, M. Photoluminescence From Chemically Exfoliated MoS_2. *Nano Lett.* 2011, *11*, 5111-5116.

(32) Coleman, J. N.; Lotya, M.; O'Neill, A.; Bergin, S. D.; King, P. J.; Khan, U.; Young, K.; Gaucher, A.; De, S.; Smith, R. J.; Shevets, I. V.; Arora, S. K.; Stanton, G.; Kim, H.-Y.; Lee, K.; Kin, G. T.; Duesberg, G. S.; Hallam, T.; Boland, J. J.; Wang, J. J.; Donegan, J. F.; Grunlan, J. C.; Moriarty, G. M.; Shmeliov, A.; Nicholls, R. J.; Perkins, J. M.; Grieveson, E. M.; Theuwissen, K.; McComb, D. W.; Nellist, P. D.; Nicolosi, V. Two-Dimensional Nanosheets Produced by Liquid Exfoliation of Layered Materials. *Science* 2011, *331*, 568.

(33) Lee, Y. H.; Zhang, X. Q.; Zhang, W.; Chang, M. T.; Lin, C. T.; Chang, K. D.; Yu, Y. C.; Wang, J. T. W.; Chang, C. S.; Li, L. J.; Lin, T. W. Synthesis of Large-Area MoS_2 Atomic Layers with Chemical Vapor Deposition. *Adv. Mater.* 2012, *24*, 2320-2325.

(34) Late, D. J.; Huang, Y. K.; Liu, B.; Acharya, J.; Shirodkar, S. N.; Luo, J.; Yan, A.; Charles, D.; Waghmare, U. V.; Dravid, V.; Rao, C. N. R. Sensing Behavior of Atomically Thin-Layered MoS_2 Transistors. *ACS Nano* 2013, *7*, 4879-4891.

(35) Liu, B.; Chen, L.; Liu, G.; Abbas, A. N.; Fathi, M.; Zhou, C. High-Performance Chemical Sensing Using Schottky-Contacted Chemical Vapor Deposition Grown Monolayer MoS_2 Transistors. *ACS Nano* 2014, *8*, 5304-5314.

(36) Li, H.; Yin, Z.; He, Q.; Li, H.; Huang, X.; Lu, G.; Fam, D. W. H.; Tok, A. L. Y.; Zhang, Q.; Zhang, H. Fabrication of Single- and Multilayer MoS_2 Film-Based Field-Effect Transistors for Sensing NO at Room Temperature. *Small* 2011, *8* (1), 63-67.

(37) Cho, B.; Kim, A. R.; Yoon, D.; Lee, Y. J.; Lee, S.; Yoo, T. J.; Kang, C. G.; Lee, B. H.; Ko, H. C.; Kim, D. H.; Hahm, M. G. Bifunctional Sensing Characteristics of Chemical Vapor Deposition Synthesized Atomic-Layered MoS_2. *ACS Appl. Mater. Interfaces* 2015, *7*, 2952-2959.

(38) Cho, B.; Yoon, J.; Lim, S. K.; Kim, D. H.; Park, S. G.; Kwon, J. D.; Lee, Y. J.; Lee, K. H.; Lee, B. H.; Ko, H. C.; Hahm, M. G. Chemical Sensing of 2D Graphene/MoS_2 Heterostructure Device. *ACS Appl. Mater. Interfaces* 2015, *7*, 16775-16780.

(39) Perkins, F. K.; Friedman, A. L.; Cobas, E.; Campbell, P. M.; Jernigan, G. G.; Jonker, B. T. Chemical Vapor Sensing with Monolayer MoS_2. *Nano Lett.* 2013, *13*, 668-673.

(40) Kim, J. S.; Yoo, H. W.; Choi, H. O.; Jung, H. T. Tunable Volatile Organic Compounds Sensor by Using Thiolated Ligand Conjugation on MoS_2. *Nano Lett.* 2014, *14*, 5941-5947.

(41) Mubeen, S.; Lai, M.; Zhang, T.; Lim, J. H.; Muchandani, A.; Deshusses, M. A.; Myung, N. V. Hybrid Tin Oxide-SWNT Nanostructures based Gas Sensor. *Electrochim. Acta* 2013, *92*, 484-490.

(42) Dey, A. Semiconductor Metal Oxide Gas Sensors: A Review. *Mater. Sci. Eng. B* 2018, *229*, 206-217.

(43) Fine, G. F.; Cavanagh, L. M.; Afonja, A.; Binions, R. Metal Oxide Semi-Conductor Gas Sensors in Environmental Monitoring. *Sensors* 2010, *10*, 5469-5502.

(44) Kumar, P.; Goel, N.; Kumar, M. UV-Activated MoS_2 Based Fast and Reversible NO_2 Sensor at Room Temperature. *ACS Sens.* 2017, *2*, 1744-1752.

(45) Long, H.; Harley-Trochimczyk, A.; Pham, T.; Tang, Z.; Shi, T.; Zettl, A.; Carraro, C.; Worsley, M. A.; Maboudian, R. High Surface Area MoS_2/Graphene Hybrid Aerogel for Ultrasensitive NO_2 Detaction. *Adv. Funct. Mater.* 2016, *26*, 5158-5165.

(46) Long, H.; Chan, L.; Harley-Trochimczyk, A.; Luna, L. E.; Tang, Z.; Shi, T.; Zettl, A.; Carraro, C.; Worsley, M. A.; Maboudian, R. 3D MoS_2 Aerogel for Ultrasensitive NO_2 Detection and Its Tunable Sensing Behavior. *Adv. Mater. Interfaces* 2017, *4*, 1700217.

(47) Fan, S. W.; Srivastava, A. K.; Dravid, V. P. UV-Activated Room-Temperature Gas Sensing Mechanism of Polycrystalline ZnO. *Appl. Phys. Lett.* 2009, *95*, 142106.

(48) Park, S.; An, S.; Mum, Y.; Lee, C. UV-Enhanced NO_2 Gas Sensing Properties of SnO_2-Core/ZnO-Shell Nanowires at Room Temperature. *ACS Appl. Mater. Interfaces* 2013, *5*, 4285-4292.

(49) Analytical Methods Committee. Recommendations for the Definition, Estimation and Use of the Detection Limit. *Analyst* 1987, *112*, 199-204.

(50) Joshi, N. V. *Photoconductivity: Art, Science, and Technology*, Marcel Dekker, Inc.: New York: NY, NY, 1990; Vol. 25, p 309.

(51) Li, G.; Suja, M.; Chen, M.; Bekyarova, E.; Haddon, R. C.; Liu, J. L.; Itkis, M. E. Visible-Blind UV Photodetector Based on Single-Walled Carbon Nanotube Thin Film/ZnO Vertical Heterostructures. *ACS Appl. Mater. Interfaces* 2017, *9*, 37094-37104.

(52) Furchi, M. M.; Polyushkin, D. K.; Pospischil, A.; Mueller, T. Mechanisms of Photoconductivity in Atomically Thin MoS_2. *Nano Lett.* 2014, *14*, 6165-6170.

(53) Fang, H.; Hu, W. Photogating in Low Dimensional Photodetectors. *Adv. Sci.* 2017, *4*, 1700323.

(54) He, Q.; Zeng, Z.; Yin, Z.; Li, H.; Wu, S.; Huang, X.; Zhang, H. Fabrication of Flexible MoS_2 Thin-film Transistor Arrays for Practical Gas-sensing Applications. *Small* 2012, *8*, 2994-2999.

(55) Lee, K.; Gatensby, K.; McEvoy, N.; Hallam, T.; Duesberg, G. S. High-Performance Sensors Based on Molybdenum Disulfide Thin Films. *Adv. Mater.* 2013, *25*, 6699-6702.

(56) Deokar, G.; Vancsó , P.; Arenal, R.; Ravaux, F.; Casanov-Cháfer; Llobet, E.; Makarova, A.; Vyalikh, D.; Struzzi, C.; Lambin, P.; Jouiad, M.; Colomer, J. F. MoS_2-

Carbon Nanotube Hybrid Material Growth and Gas Sensing. *Adv. Mater. Interfaces* 2017, *4*, 1700801.